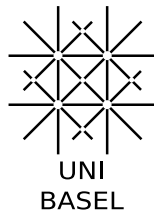


Exploring T_2^* decay
New methods for short echo time imaging
and fat-water quantification

Inauguraldissertation

zur Erlangung der Würde eines Doktors der Philosophie
vorgelegt der
Philosophisch-Naturwissenschaftlichen Fakultät
der Universität Basel

von
Xeni Deligianni
aus Thessaloniki, Griechenland



Basel, 2013

Genehmigt von der Philosophisch-Naturwissenschaftlichen Fakultät

auf Antrag von:

Prof. Dr. Klaus Scheffler

Referent

Prof. Dr. Sebastian Kozerke

Korreferent

Basel, den 17.09.2013

Prof. Dr. Jörg Schibler

Dekan

Abstract

The major advantage of magnetic resonance imaging (MRI) over other imaging modalities like computed tomography (CT) is that it does not utilize ionizing radiation. A drawback of MRI in comparison to CT is that in general it requires longer scan times and for this reason fast scanning techniques have been proposed. Fast MR imaging can refer to fast scan times or fast signal acquisition. The first is important in various cases such as in abdominal scans to decrease motion sensitivity, while short echo times and short acquisition times allow visualization of tissues with fast signal relaxation. One category of MR sequences that allows fast scanning is gradient echo sequences. These sequences do not use radiofrequency pulses to yield a signal echo and this allows fast imaging, shorter echo times and scan times, while the signal decays according to the apparent transverse relaxation T_2^* . Gradient echo sequences can be used both for qualitative and quantitative imaging and during this thesis an application in each direction was explored.

The first part of this thesis is related to fast gradient echo imaging for qualitative imaging of fast decaying signals. It is focused on the development of a short echo time sequence that can be easily translated to clinical settings. In the first chapter of this part a novel short echo time sequence is being introduced. Subsequently, two different applications are being discussed. Firstly, the application of the sequence to musculoskeletal imaging at high and ultra-high field is being described. In the second chapter, the effect of fat suppression on short T_2 tissues imaging is being considered. At the last chapter of this part the sequence is adapted to be used for molecular imaging of iron oxide labeled cells.

The second part of this thesis refers to quantitative gradient echo imaging. The aim is tissue characterization based on the analysis of the signal decay. A multi-echo sequence is adapted in order to be used with a novel powerful fitting tool for three-dimensional (3D) liver fat-water imaging. Preliminary results are presented from a comparison with a standard two-point Dixon technique.

Publications arising from this thesis

Journal papers

- **Deligianni X**, Bär P, Scheffler K, Trattnig S and Bieri O (2012), High-resolution Fourier-encoded sub-millisecond echo time musculoskeletal imaging at 3 Tesla and 7 Tesla. *Magn Reson Med.* doi: 10.1002/mrm.24578
- **Deligianni X**, Bär P, Scheffler K, Trattnig S and Bieri O, Water-selective excitation of short T_2 species with binomial pulses, *Magn Reson Med*, *submitted*
- **Deligianni X**, Jiráček D, Scheffler K, Berková Z, Hájek M and Bieri O, In vivo visualization of cells labeled with superparamagnetic iron oxides by a sub-millisecond gradient echo sequence, *Magnetic Resonance Materials in Physics, Biology and Medicine*, *submitted*
- Juras MV, Apprich, S, Zbýň Š, Zak L, **Deligianni X**, Szomolanyi P, Bieri O and Trattnig S (2013), Quantitative MRI analysis of menisci using biexponential T_2^* fitting with a variable echo time sequence. *Magn Reson Med.* doi: 10.1002/mrm.24760
- Juras MV, Apprich S, Szomolanyi P, Bieri O, **Deligianni X**, Trattnig S, Biexponential T_2^* analysis of healthy and diseased Achilles tendons: an in vivo preliminary magnetic resonance study and correlation with clinical score, doi: 10.1007/s00330-013-2897-8.

Conference proceedings

- **Deligianni X**, Scheffler K and Bieri O, A high resolution variable echo time 3D spoiled gradient echo sequence for imaging of short T2 components, Proceedings of the 28th annual scientific meeting of ESMRMB, Leipzig, Germany, 2011.
- **Deligianni X**, Bär P, Scheffler K, Trattnig S, and Bieri O, Water selective high resolution imaging of short T_2 components of the knee at high and ultra high field strengths, *Proc. Intl. Soc. Mag. Reson. Med.* 20 (2012), 3315.

-
- **Deligianni X**, Scheffler K and Bieri O, Fast 3D Quantification of Fat Liver Tissue Using Sequentially Shifted Echo Times and a singular value decomposition matrix pencil method, Proc. Intl. Soc. Mag. Reson. Med. 20 (2012), 4032.
 - **Deligianni X**, Jirák D, Scheffler K, Berková Z, Hájek M and Bieri O, In vivo visualization of cells labeled with superparamagnetic iron oxide by a variable echo time double contrast spoiled gradient echo sequence in diabetic patients, Proceedings of the 29th annual scientific meeting of ESMRMB, Lisbon, Portugal, 2012.

Conference proceedings (contributions)

- Juras V, Apprich S, Szomolanyi P, Bieri O, **Deligianni X**, and Trattnig S, Advanced Bi-Exponential Analysis of T_2^* in the Achilles Tendon of Pre- And Post-Operative Patients Using a Variable Echo Time Sequence at 3T, Proc. Intl. Soc. Mag. Reson. Med. 21 (2013), 0688.
- Juras V, Apprich S, Szomolanyi P, Zak L, Bieri O, **Deligianni X**, and Trattnig S, Analysis of Menisci Using Bi-Exponential T_2^* Fitting with VTE Sequence at 3T, Proc. Intl. Soc. Mag. Reson. Med. 21 (2013), 3465.
- Juras V, Apprich S, Szomolanyi P, Kronnerwetter C, Bieri O, **Deligianni X**, and Trattnig S, A Comparison of T_2^* Measured by a Variable Echo Time Sequence at 3 and 7T in Connective Tissues in the ex vivo Knees, Proc. Intl. Soc. Mag. Reson. Med. 21 (2013), 3466.
- Zbyn S, Apprich S, Juras V, Szomolanyi P, Walzer SM, **Deligianni X**, Traxler H, Bieri O, and Trattnig S, Ex Vivo Mapping of Sodium T 1 and T2* Relaxation Times in Human Lumbar Intervertebral Discs at 7 Tesla, Proc. Intl. Soc. Mag. Reson. Med. 21 (2013), 2473.
- Zbyn S, Juras V, Michaely HJ, **Deligianni X**, Bieri O, Schoenberg SO, Trattnig S, and Haneder S, In Vivo Functional Sodium MR Imaging of the Human Kidneys at 7 Tesla, Proceedings of the Annual Meeting ISMRM 2013, 4140.
- Schönbauer E, Riegler G, Apprich S, Juras V, **Deligianni X**, Bieri O, Zbyn S, and Trattnig S, Quantitative MR Imaging - T2*-Mapping of the Knee Joint Using a Multi-Echo VTE-Sequence at 3 Tesla: Preliminary Results, Proc. Intl. Soc. Mag. Reson. Med. 21 (2013), 1605.
- Zbyn S, Juras V, Michaely HJ, **Deligianni X**, Oliver Bieri, Schoenberg SO, Trattnig S, and Haneder S, Sodium T_2^* Mapping of the Human Kidneys in Vivo at 7 Tesla, Proc. Intl. Soc. Mag. Reson. Med. 21 (2013), 4142.
- Juras V, Menedez MI, Hofstaetter J, Brix M, Walzer S, Szomolanyi P, Bieri O, **Deligianni X**, and Trattnig S, T_2^* of the Osteochondral Junction Measured by

VTE at 7T and Correlated with Histology, Proc. Intl. Soc. Mag. Reson. Med. 21 (2013), 3532.

- Menendez, MI, Juras, V, Hofstaetter, J, Brix, M, Walzer, S, Szomolanyi, P, Bieri, O, **Deligianni, X** and Trattnig, S, T_2^* of calcified cartilage and osteochondral junction at 3 Tesla and 7 Tesla field strength and histological correlation, osteoarthritis and cartilage, (21), S190-S191.

Contents

1	Introduction	13
1.1	3D Short-TR SPGR MRI	14
1.2	Short Echo Time Imaging	15
1.2.1	Short T_2 species	16
1.2.1.1	MRI of SPIO labeled cells	17
1.2.2	Ultrashort echo time (UTE) imaging	19
1.2.2.1	More recent UTE methods	20
1.2.3	Cartesian representation vs radial representation	21
1.2.4	Variable echo time (vTE) imaging	22
1.2.4.1	Partial Fourier reconstruction	22
1.2.5	Complementary techniques used with short echo time imaging	23
1.2.5.1	Long T_2 suppression	24
1.2.5.2	Fat suppression	25
1.2.6	From high to ultra-high field	26
1.3	Fat-water quantification	27
1.3.1	^1H MRS of liver fat	27
1.3.2	Dixon methods	28
1.3.2.1	Two-point Dixon	29
1.3.2.2	Three-point Dixon / Multi-point Dixon	29
1.3.3	Fat-water imaging and simultaneous T_2^* quantification	30
1.4	Aim of the thesis	31
1.5	Outline of the thesis	32
	References	34
I	Variable Echo Time SPGR	45
2	High-resolution Fourier-encoded sub-millisecond echo time musculoskeletal imaging at 3 Tesla and 7 Tesla	47
2.1	Introduction	48
2.2	Methods	49
2.2.1	Experiments	49
2.3	Results	51

2.3.1	Imaging of connective tissue at 3T	51
2.3.2	Imaging of the knee joint and the Achilles tendon at 7T	53
2.4	Discussion	54
References		56
References	56
3	Water selective excitation of short T2 species with binomial pulses	59
3.1	Introduction	60
3.2	Methods	60
3.2.1	Simulations	61
3.2.2	Imaging experiments	62
3.3	Results	62
3.4	Discussion	68
References		70
References	70
4	In vivo visualization of cells labeled with superparamagnetic iron oxides by a sub-millisecond gradient echo sequence	73
4.1	Introduction	74
4.2	Methods	75
4.3	Results	78
4.3.1	Phantom scan	78
4.3.2	Animal scan	79
4.3.3	Patient scan	80
4.4	Discussion	83
References		85
References	85
II	Fat-Water quantification	87
5	Fast Quantitative Fat-Water Liver Imaging Based on a Multi-Echo Gradient Echo Singular Value Decomposition Matrix Pencil Method	89
5.1	Introduction	90
5.2	Methods	91
5.2.1	Singular Value Decomposition Matrix Pencil Method	91
5.2.2	Sequence Adaptation and Setup	91
5.2.3	Data Analysis	93
5.3	Results	94
5.3.1	Liver Fat Quantification in Dairy Cream Phantoms	94
5.3.2	Liver Fat Quantification In Vivo	95
5.4	Discussion	98

References	99
References	99
III Conclusion	103
6 Summary and conclusion	105
6.1 Variable Echo Time Imaging	106
6.2 Water-Fat Imaging	107
6.3 Outlook	107
References	109

Chapter 1

Introduction

In 1980's the first MRI clinical scanners were introduced [1]. MRI was introduced as an imaging modality outperforming other existing imaging modalities in imaging of soft tissue. Since its introduction, its range of applications has been broadened a lot and innovations in qualitative and quantitative MR imaging have been achieved. Today, MRI has been introduced in the clinical routine for musculoskeletal imaging [2–6]. In addition, it is also used for tissue characterization, since it has been shown that tissue changes such as fat infiltration are reflected in tissue properties visible with MRI and MR spectroscopy (MRS) [7, 8].

MRI is based on the creation of a signal echo either with radiofrequency (RF) pulses or with switching gradient pulses. The second category, which allows for shorter repetition times was already introduced in 1986 by Jens Frahm and Axel Haase as rapid NMR imaging [9]. This evolved in one broad category of MR sequences, that allows fast imaging, shorter echo times and scan times. In this case, since no 180 degrees RF pulse is employed, field inhomogeneities are not compensated for and the signal decays according to the apparent transverse relaxation T_2^* [10–12]. Fast imaging can be beneficial in many cases such as in abdominal scans to decrease motion sensitivity, while short echo times allow visualization of tissues with fast signal relaxation.

1.1 3D Short-TR SPGR MRI

In gradient echo sequences (GRE), gradient reversal on the frequency encoding axis is used to form a signal echo (see Fig. 1.1). Since in GRE sequences the flip angle α is typically less than 90° , no long period is needed for T_1 recovery and shorter repetition times can be used [12, 13].

In GRE sequences steady states of both the longitudinal and the transverse magnetization can be considered [12]. If the transverse magnetization is considered to be zero before the next excitation than the sequence is defined as spoiled. Spoiled GRE sequences (SPGR) are a class of gradient echo sequences where the transverse magnetization is disrupted (spoiled) before the next excitation pulse, and are most commonly used to generate T_1 -weighted contrast. Spoiling can be achieved by choosing a very long repetition time (TR) in comparison to T_2 so that the transverse magnetization completely decays before the next excitation [11, 12].

An alternative method that allows for much faster repetition times is to apply gradient spoilers at the end of the sequence, but they are not so effective at disrupting the magnetization and spoiling can be spatially non-uniform [12]. A more efficient way is to use RF spoiling in addition (i.e., to phase cycle the RF excitation in a nonlinear way). The phase of the RF pulses can be random, but a more popular way is to select the phase Φ_j of the B_1 field of the j^{th} RF pulse according to a predetermined equation:

$$\Phi_j = \Phi_{j-1} + j\Phi_0 \quad (1.1)$$

The value of Φ_0 is predetermined and a value of 117° is recommended by Zur et al. [14]. Due to the fact that the phase increment $\Phi_j - \Phi_{j-1}$ is linearly proportional

to j , the phase Φ_j varies quadratically with j . With RF spoiling, image contrast can become independent of T_2 and approximate T_1 weighting can be achieved.

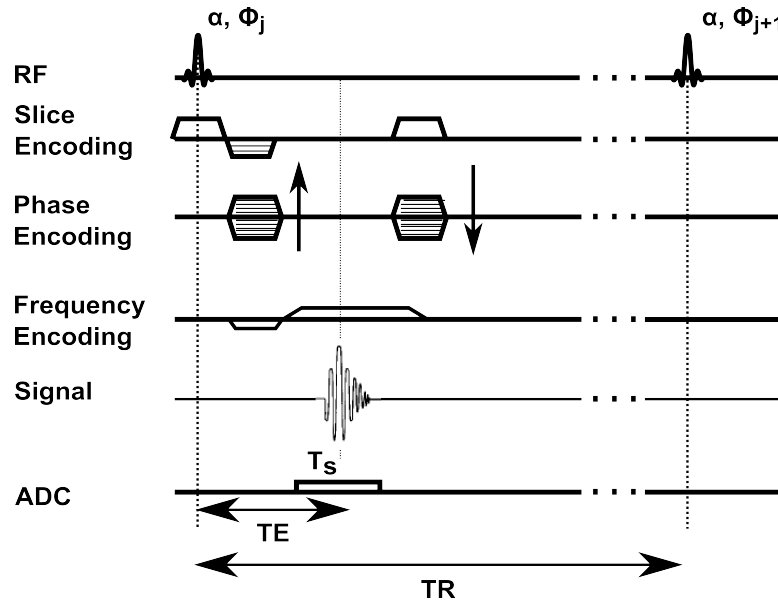


Figure 1.1: Pulse sequence diagram for a standard spoiled gradient echo sequence (source: [12]).

The acquisition of SPGR sequences can be carried either with single- or multi-slice two-dimensional (2D) encoding or with a volumetric encoding. In 2D acquisition, each slice is excited by a spatially-selective radiofrequency pulse, and multiple slices can also be interleaved in the same TR. In contrast, in three-dimensional (3D) volume MR acquisition a set of contiguous slices is simultaneously excited. In rectilinear sampling [15] resolution of the different slices is achieved by using an additional phase encoding direction perpendicular to the one used for image encoding [12]. 3D sequences might require increased scan time over 2D sequences for the same number of slices, but their advantage is that they offer thin contiguous slices and higher SNR [11].

1.2 Short Echo Time Imaging

MRI is outperforming other modalities in soft tissue imaging, because among other factors, it highly depends on the proton density of tissues. That is successful in tissues which have a high percentage of water or low susceptibility issues. Since the early times of MR there has been interest in imaging of tissues that have local field inhomogeneities (i.e., high susceptibility) or little water content, for example in musculoskeletal (MSK) imaging (i.e., tendons, menisci, bone, dentine) or lung imaging. A common characteristic of all these tissue species is that the spin-spin relaxation happens very fast even during excitation, so it is important to have short radiofrequency pulses and to start the

signal acquisition as soon as possible after excitation. One of the first focuses of these techniques was the lung parenchyma, in order to partly substitute computer tomography, which uses ionizing radiation and highlight regional differences [16]. The aim of lung MRI is to produce diagnostic information about the lung parenchyma such as perfusion assessment and measurement of ventilation and respiratory mechanics without the use of ionizing radiation [17, 18]. MRI can also be used to detect cancer nodules or airway diseases [19].

Lung has air-tissue interfaces that create large variations in magnetic susceptibility. Conventional gradient echo sequences use an echo time in the order of 2-3 ms, which is too long to acquire a detectable signal. Although this is already a considerable improvement in respect to spin echo methods it is not sufficient when the focus of interest is in highly ordered tissues.

Already in the early 90' s it was proven that to get MR signal out of the lungs, the acquisition has to be performed as close as possible to the excitation so tissues with very short T_2 decay could be measured. In 1991, Bergin et al. [20, 21] introduced a method, which is nowadays broadly known as Ultra Short Echo (UTE), that allowed a first introduction of lung imaging by achieving ultra short echo times.

After lung the focus of short echo techniques moved to MSK because of the possibility of measuring highly ordered tissues (menisci, tendons) that have short T_2 values and are usually black in conventional imaging [22, 23].

1.2.1 Short T_2 species

Short T_2 tissue components are present in various tissues in the human body and are of high clinical significance. The increase or decrease in the relative amount of short T_2 species can indicate various pathologies [2, 24, 25]. Some clinical applications of the quantification of short T_2 components are chronic fibrosis, iron deposition, hemorrhage, calcification and deposition diseases (amyloidosis, etc). In certain cases the signal of the short T_2 components is increased (e.g. chronic fibrosis, hemorrhage calcification), while loss of tissue or change of the order of tissue, demyelination or edema can cause signal decrease [24].

Conventionally, short T_2 species are considered the species with time constant T_2 (transverse relaxation) less than 10 ms. T_2 is caused by the dephasing of different spins due to variations in local precession frequencies, while T_2^* is the apparent transverse relaxation time constant, which is also affected by external field inhomogeneities. At a molecular level, protons in water associated with macromolecules have T_2 values of less than 1 ms, while protons that are very closely associated with macromolecules have T_2 in the order of tens of microseconds [28]. In other words, a more mobile environment reduces dipolar coupling between the spins and increases T_2 , while in a more ordered environment such as in the case of tendons, menisci or bone, the coupling is stronger and the T_2 values are reduced [29].

Short T_2 species require special sequences for their visualization. Since their signal decays very fast, short echo times need to be employed. In addition, their relaxation time is comparable to the duration of the RF pulse so the relaxation and excitation

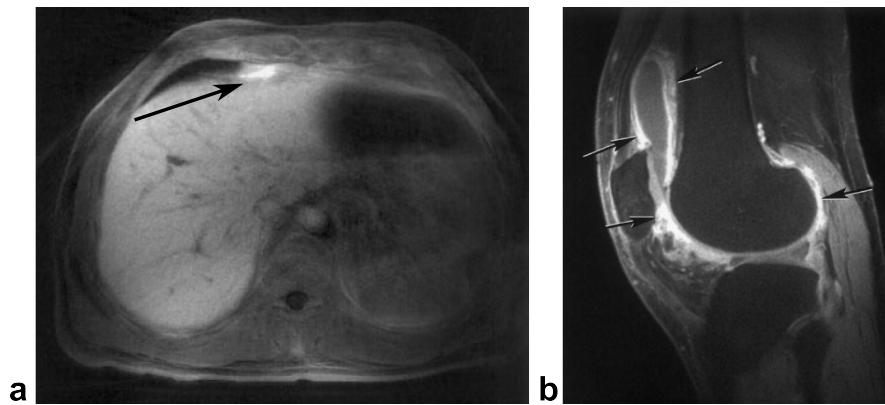


Figure 1.2: Short T_2 clinical applications: a) Difference fat-suppressed UTE (d FUTE) liver image of a patient with hemochromatosis [26], b) d FUTE images of a patient with chronic arthritis (source: [24], [27]).

processes occur simultaneously [30]. Finally, short T_2 species have broad line-width (see Fig. 1.3) and can be saturated by off-resonance pulses [29].

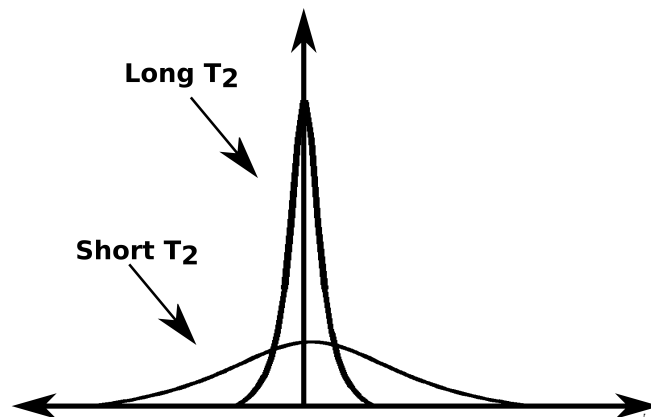


Figure 1.3: Spectral line-width proportional to T_2 (source: [29])

1.2.1.1 MRI of SPIO labeled cells

Short T_2 species have an inherent characteristic of short transverse relaxation times, however $T_2 - T_2^*$ effects can be artificially induced in order to make cells visible with MRI. This concept is used in molecular MRI where cells are labeled with contrast agents in order to induce susceptibility effects and visualize them in a noninvasive way with MRI [31]. Labeling allows longitudinal studies to follow-up the fate and functionality of various cells over time.

Superparamagnetic iron oxide nanoparticles (SPIO) are the most common contrast

agent used for cell tracking [32]. They have a size of some tens of nm (50-100 nm) and they are generally constituted by a core of ferric and ferrous oxides coated by a layer of dextran or other polysaccharide for biocompatibility [33]. Labeling induces a pronounced shortening of T_2 and T_2^* and in this way single cells become visible to MRI. Despite the diameter of 50-100 nm, the labeling effect extends in space much more than the volume of the particle (see Fig. 1.4) and for this reason they have been successfully used as labeling agent for cells.

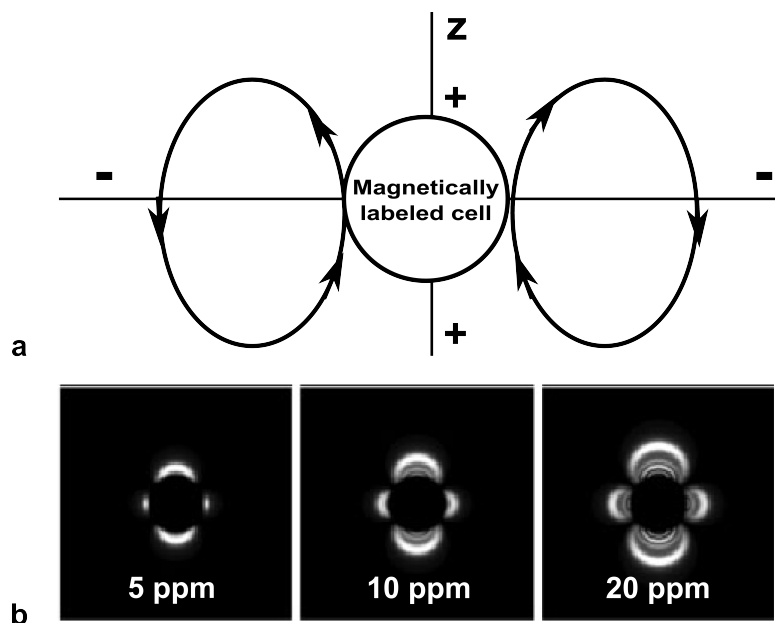


Figure 1.4: SPIO magnetic field: a. Representation of the magnetic lines induced outside a magnetically labeled cell (source: [34]), b. Sample positive contrast images produced with the PARTS method (source: [35]). The region of positive contrast extends further for increased susceptibility difference.

SPIO nanoparticles have been used for cell labeling of stem cells [36] and pancreatic islets [37–40] (a more extensive treatise of pancreatic islets imaging can be found in chapter 4). Labeling of pancreatic islets enables follow up of the success of their transplantation into the liver of diabetic patients (see Fig. 1.5) and it has been proved that the labeling gives information about the functionality of the islets after their transplantation into the liver [41].

Sequences sensitive to T_2^* effects such as GRE are typically used for the follow-up of targeted islets, where the labeled cell forms a relatively large hypointense region due to signal dephasing, but there are many sources (i.e., other sources of susceptibility such as air and air-tissue interfaces) that can cause hypointensities so these sequences are sensitive to false positives. Since the resulting transverse relaxation times are very short, short echo time imaging techniques are especially useful for their visualization because they can allow positive contrast visualization where the labeled cells appear

hyperintense. Finally, the development of new more efficient contrast agents for MR is a very active research direction [42, 43].

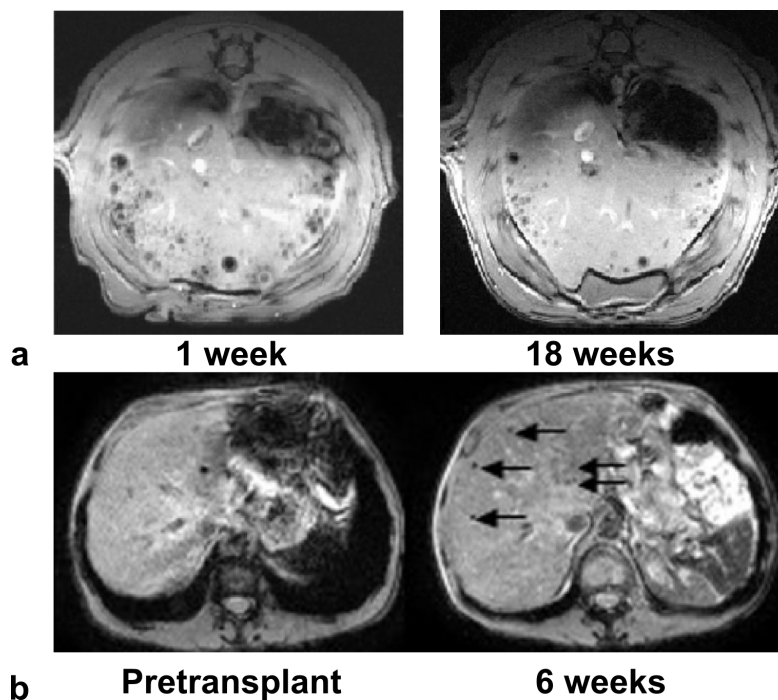


Figure 1.5: Labeled cells appear on T_2 sensitive images as hypointensities: a) Rat with labeled pancreatic islets 1 and 18 weeks after their transplantation to the liver (source: [37]), b) liver images from a patient before and 6 weeks after pancreatic islets transplantation to the liver (source: [44]).

1.2.2 Ultrashort echo time (UTE) imaging

The technical possibilities for the visualization of short T_2 species have been explored for more than two decades. The first UTE sequences were two-dimensional (2D) with half excitation and radial sampling (see Fig. 1.6). The first basic sequence scheme, as it was introduced in 1991 [20], consisted of two half-sinc radiofrequency (RF) excitation pulses and projection reconstruction acquisition gradients (see Fig. 1.6). In this sequence, a conventional slice-selective pulse is truncated in the time domain at the point of peak output power. This way, acquisition can start immediately after the pulse without the need of a slice refocusing gradient. In order to avoid introducing phase encoding gradients, a center-out radial acquisition is performed, so the center of k-space is sampled at the shortest possible time after excitation. In order to maintain the same slice selectivity characteristics, the acquisition needs to be repeated twice with reverse polarity of the slice selection gradient and the acquired signals are summed in the complex domain [45–48]. In order to further reduce the echo time, the acquisition is started during the ramping up of the readout gradient.

The 2D UTE sequence relies on the complex sum of the signals acquired at different times: this makes it very susceptible to eddy currents, which cause a broadened slice profile since the transverse magnetization is not properly refocused after summing of the signals [49]. An important aspect in imaging of short T_2 species with UTE is that the transverse decay that happens during excitation is considerable. The excitation and decay procedures happen simultaneously and for this reason it is important to have fast excitation pulses [30].

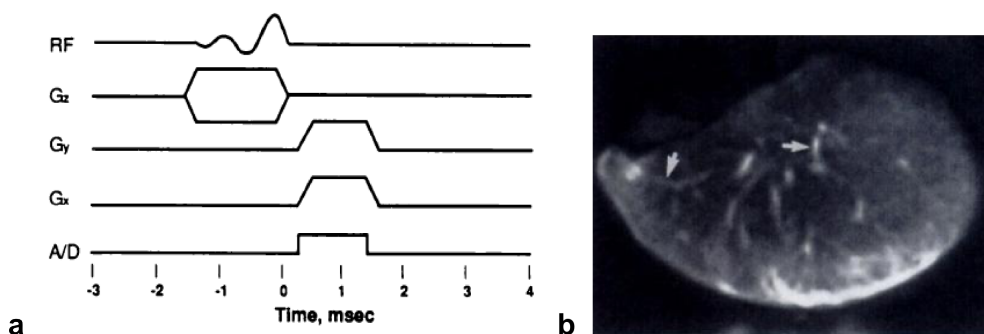


Figure 1.6: a. Pulse sequence diagram of a first implementation of a 2D UTE, b. projection reconstruction (UTE) image from excised human lung. The arrows indicate vessels (source: [20]).

Shortly after this 2D version, a 3D sequence variant was introduced [25, 50–53]. Instead of using two half excitations, this method uses a single hard, non-selective pulse and a 3D radial center-out (“kooshball”) acquisition of free-induction decay, producing an image with isotropic resolution. This method needs a longer acquisition time but the RF excitation is shorter and more robust than in the 2D variant, which is sensitive to timing errors, eddy currents and large excitation tails that complicate multi-slice scanning [49, 52]. Typically, data acquisition already starts during ramp up of the readout gradient in order to minimize the effective echo time.

Since the signal is acquired shortly after excitation, the inherent contrast of the image is very low. Therefore, preparation pulses are typically used or additional echoes are acquired in order to suppress the long T_2 species (more in 1.2.5.1) [29, 48]. Finally, another key characteristic of these sequences is the radial sampling as opposed to traditional Fourier sampling. For this reason, the image reconstruction also requires regridding (i.e. of the radially sampled data to a rectangular k-space) [29].

1.2.2.1 More recent UTE methods

In the recent years, UTE has been extended in order to overcome some of its limitations. The directions of development have been mainly two: optimizing the excitation and optimizing k-space encoding.

1) More complex ways of excitation

An important technical aspect for imaging short T_2 tissues is that the excitation has to be as short as possible. Following this principle, in the early 90's [54] another method (called BLAST and later evolved to the zero TE) was proposed where the data acquisition “starts” before excitation. UTE scheme allows the collection of samples just after we excite the tissue, while in zero TE (zTE) technique (see Fig. 1.6) data sampling starts even before excitation. The drawback is that like more recent advanced excitation methods such as SWIFT [55], which aim to minimize the time between excitation and signal acquisition, this usually requires external technical equipment in order to achieve instantaneous switching between excitation and reception of the signal and therefore it cannot be used in a standard clinical facility.

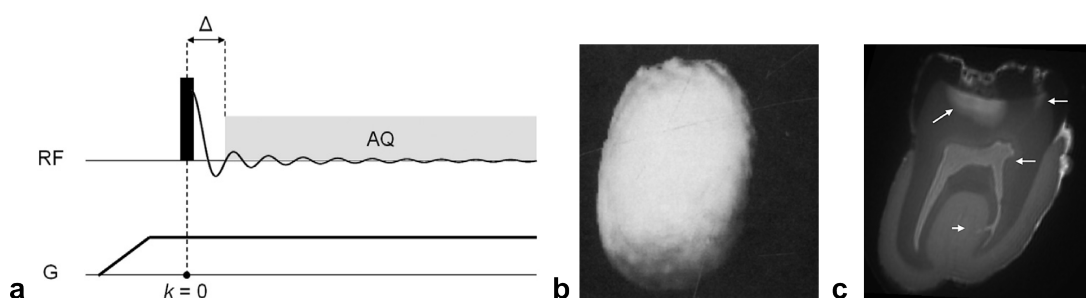


Figure 1.7: a. Pulse sequence diagram for a zTE sequence (source: [56]), b. surface image of a grape acquired with the BLAST sequence (source: [54]), c. recent zTE images from a molar with caries lesions (source: [57])

2) more efficient k-space trajectories

Non-cartesian trajectories is one main characteristic of UTE methods. Spiral [58–60], cone [61, 62] and other complex trajectories have been employed to traverse k-space or even hybrid methods such as PETRA [63] where k-space is sampled in a hybrid way in order to minimize artifacts due to incorrect sampling of k-space center.

1.2.3 Cartesian representation vs radial representation

Radial sampling is usually employed with UTE sequences in order to achieve shorter echo times. Radial sampling though is not as efficient as Cartesian and it takes as a general estimate six times longer [64, 65]. Higher number of acquisitions are required for the same field-of-view (FOV) to satisfy the Nyquist criterion, because the periphery of k-space is sparsely sampled; on the other hand, the center is oversampled yielding higher SNR and lower flow and motion sensitivity [64]. For this reason non-cartesian trajectories are usually undersampled, but special weighting strategies are needed to compensate for this fact [66].

Finally, a drawback of UTE techniques is the presence of artifacts introduced by system delays and eddy currents that have not decayed at the moment of acquisition

and cause the actual trajectory to vary from the expected [67]. Since radial acquisition requires regridding, these effects cause artifacts during image reconstruction. More specifically, gradient timing delays and eddy currents result in variations of the effective echo times with the projection angle, since the center of k-space is “missed” in an angularly dependent manner [68]. While Cartesian acquisitions are inherently robust to system delays and eddy currents, these effects can degrade the image quality of UTE-like sequences that employ high slew rates and in some cases time-varying gradient waveforms [67].

1.2.4 Variable echo time (vTE) imaging

The most important concept behind UTE is to acquire the center of k-space as fast as possible after excitation, since it contains the contrast information of the image [11]. In this way susceptibility dephasing effects can be reduced and the signal of fast decaying species can be captured. For this reason, a UTE-like method was proposed in the early 90’s where prephasing time is not constant across k-space [69]. Instead, in the center of k-space, where there are no phase encoding gradients, the encoding is performed as fast as the system allows, and the echo time is gradually increased towards the periphery of k-space while keeping the gradient performance at maximum possible. The initial sequence was using asymmetric RF pulses for excitation in order to optimize its performance, and asymmetric echo sampling was also used to minimize echo time even further. One of the first applications was high resolution imaging of the inner ear [70], while in later years it was also used for bone imaging [71]. The initial concept was to use fixed receiver bandwidth [70, 72], while later [73] variable bandwidth was also introduced.

The advantage of vTE methods with respect to UTE is higher robustness because they can exploit Cartesian sampling (see section 1.2.3) while maintaining a low effective echo time, making them additionally more efficient in sampling and reconstruction time.

1.2.4.1 Partial Fourier reconstruction

One way to speed up the acquisition procedure in order to achieve shorter echo and scan times is to collect only part of k-space. In partial Fourier acquisition, data are not collected symmetrically around k-space [12]. Partial Fourier k-space has many benefits since it can allow reduced echo time and scan time. In case that the direction of asymmetric sampling is the frequency encoding direction the partial Fourier acquisition is called partial or asymmetric echo.

Partial Fourier transform is possible because in principle only one half of k-space is needed in order to reconstruct a real object, since its Fourier Transform is Hermitian (i.e., the real part is symmetric and the imaginary antisymmetric). In principle, various phase shift effects such as motion and eddy currents violate the assumption that the reconstructed object is real introducing phase errors, which would not be an issue in the case of a fully sampled k-space.

In order to counteract this effect many techniques for reconstruction of asymmetrically sampled k-space have been developed [74]. In the simplest case zero-filling is used to replace the unmeasured data. Other methods of reconstructing an incomplete data set are homodyne, Margosian, Cuppen, Projection onto Convex Sets formalism (POCS), FIR and MoFir [74,75]. These algorithms exploit the redundancy of k-space to calculate the missing data, through reflection of the conjugate data across the k-space origin (see Fig. 1.8) and they differ mainly on the methods they use for phase correction.

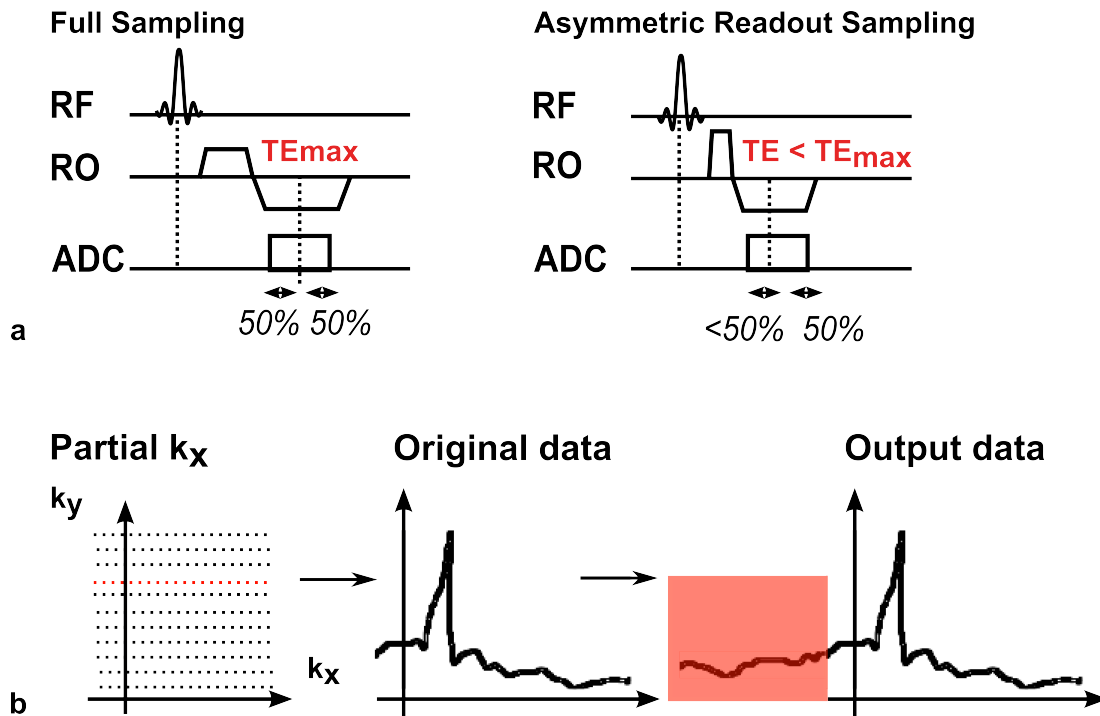


Figure 1.8: Description of asymmetric data reconstruction algorithm: a. Pulse diagram of an asymmetrically sampled echo, b. k-space description of asymmetric sampling and reconstruction with correction algorithms (source: [12, 74]).

1.2.5 Complementary techniques used with short echo time imaging

In the very short echo time regime there is no contrast between the short T_2 species and the background, as the contrast is mostly spin-density weighted. Therefore, preparation pulses are typically introduced in order to suppress the background of short T_2 species or alternatively a second echo is also acquired and short T_2 contrast is achieved through post-processing. Principally long T_2 tissues need to be suppressed (i.e., water) and in addition fat suppression has been proven especially beneficial.

1.2.5.1 Long T_2 suppression

Suppression of species with long T_2 can be achieved with preparation pulses or with image subtraction. Long T_2 species suppression yields images where short T_2 species appear bright and are typically referred to as positive contrast images.

Preparation pulses for the suppression of long T_2 species are usually saturation pulses: radiofrequency pulses are used that have a duration greater than the T_2 of the short species and flip angle 90° or larger. In this way only the long T_2 species are excited, since the decay rate of the short T_2 is faster than the excitation rate. At the end of the pulse, a spoiling gradient is applied to dephase the magnetization of the long T_2 species [45, 51, 52, 76]. Instead of saturation pulses, inversion pulses can also be used [48, 77, 78].

Image subtraction works on the principle that there is no significant decay in signal intensity for the long T_2 species in the ultrashort echo and in a later echo time. For this reason, a second echo needs to be acquired and its intensity is subtracted from the first (see Fig. 1.9).

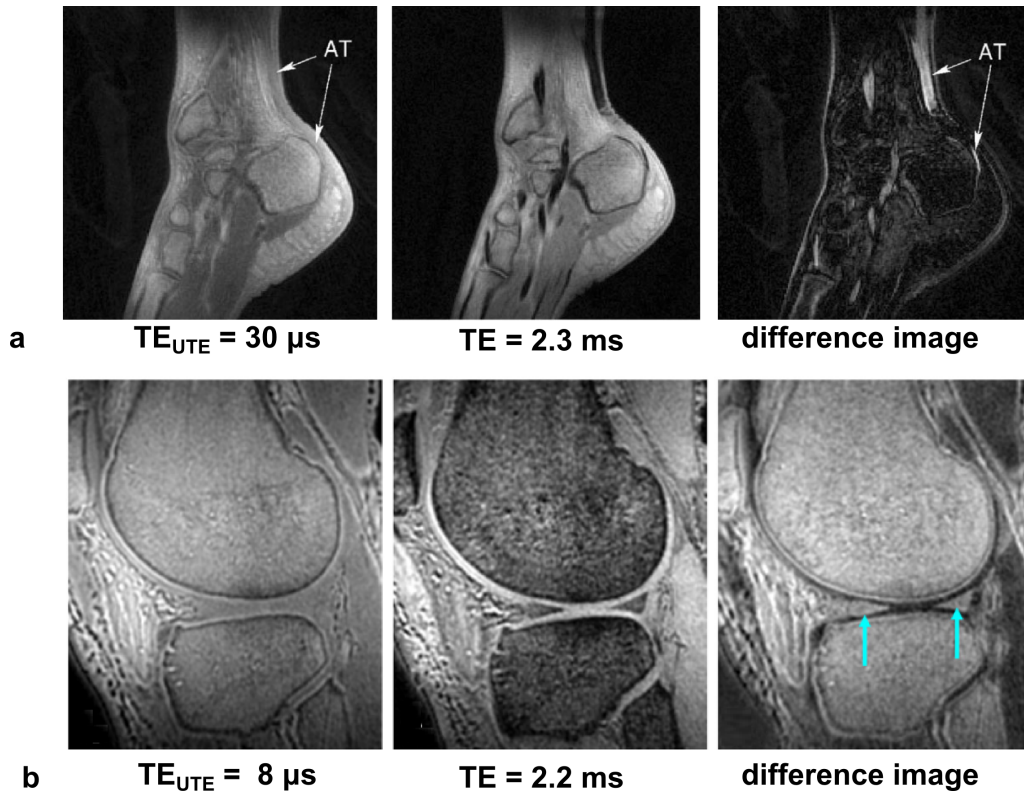


Figure 1.9: MSK exemplary images of 3D UTE: a. Achilles tendon image (source: [51]), b. knee image (source: [79]). The UTE image exhibits high signal for all tissues, while the difference image shows high signal from short T_2 tissues.

1.2.5.2 Fat suppression

Fat suppression techniques are applied to suppress signal from adipose tissue that can hide underlying abnormalities such as inflammation or edema. In case of MSK imaging, fat suppression can considerably highlight structures such as the menisci and the ligaments. In SPGR sequences fat appears bright due to its short T_1 relaxation time ($T_1 = 296$ ms at 1.5 T, $T_1 = 366$ ms at 3T [80]). Successful elimination of the fat signal allows the use of lower bandwidths since chemical shift artifacts are no longer present. For this reason, fat suppression not only increases the conspicuity of highly ordered tissues, but in addition it allows high signal-to-noise ratios since lower receiver bandwidths can be used.

Frequency based fat suppression techniques are more effective at high field, since the distance of water and fat peaks is larger, while phase based (e.g. Dixon based [81, 82]) methods are more effective at low field [83–85].

The most commonly used techniques include chemically-selective fat-suppression pulses, inversion recovery methods, water excitation and phase-based reconstructions.

1) Chemically selective fat suppression (FATSAT)

Off-resonant pulses have been broadly used in the clinics in order to suppress fat signal for MSK imaging [86, 87]. The so called FATSAT pulses are preparation pulses, centered at the main peak of the fat spectrum, that excite the fat signal and subsequently destroy it with spoiler gradients [88, 89].

However, short T_2 species have broad line-width (see Fig. 1.3) and therefore off-resonant pulses (as mentioned above) may partly saturate them. Fat suppression can therefore also reduce the conspicuity of short T_2 components [29]. Finally, another disadvantage of this method is that it is sensitive to both B_0 and B_1 inhomogeneities.

2) Short TI inversion recovery (STIR) and spectrally-selective adiabatic inversion recovery (SPAIR)

The STIR method uses an inversion pulse in order to suppress the signal from short T_1 tissues such as fat [90]. This method provides uniform fat suppression and is robust to B_0 inhomogeneities. The disadvantage is that these images are heavily T_1 -weighted [85], because also the water signal experiences an inversion. To avoid this effect, a frequency-selective inversion pulse can be used, usually following an adiabatic shape in order to reduce B_1 sensitivity. However, this method introduces again a dependence on B_0 because of the spectral selectivity of the pulse.

3) Water-excitation

Another method to suppress fat is to selectively excite the water or fat components. Composite binomial pulses have been used for this purpose (more about binomial pulses at chapter 3). In general, water-excitation pulses describe a train of RF pulses that are separated by a time delay. During this delay, the fat component precesses in such

a way that after the final excitation the water component is excited, while the off-resonant component is flipped back to the longitudinal axis (see Fig. 1.10). Some implementations of binomial pulses also include spatial-spectral pulses [14,91,92], which can be selective both in spatial location and frequency.

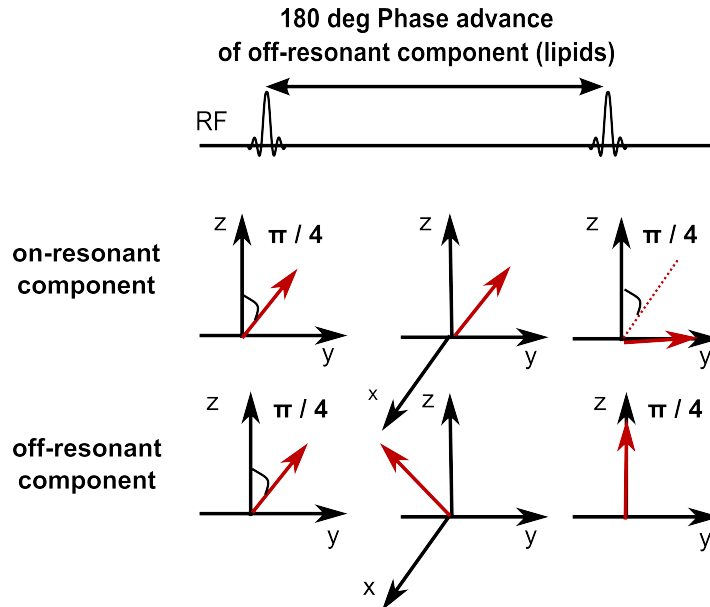


Figure 1.10: Representation of the magnetization vector for an on-resonant and off-resonant spin precession for a simple 1-1 90 degrees binomial excitation. The on-resonant spin is initially aligned with the z axis. The first sub-pulse flips it by 45° and the second sub-pulse flips it to the y axis. The off-resonant spin precesses 180 degrees in the interpulse interval so the second pulse flips it back to the z axis (source: [12]).

4) Chemical shift based

Another technique for fat suppression is based on Dixon methods (see paragraph 1.3.2). In this spectroscopic imaging technique [81] the chemical shift between water and fat is encoded in the signal phase. In the initial simple approach two images are acquired with the water and fat signals in- and out-of-phase and water-only and fat-only images are acquired in post-processing.

1.2.6 From high to ultra-high field

Short T_2 species are usually found in low concentration in the body, therefore this kind of imaging can highly benefit from the increased polarization (and consequently higher SNR) at higher field strength. Moreover, ultra-high field strength (7T and above) in conjunction with short TE methods can be used for the imaging of non-proton species (for example sodium MRI) whose abundance is too low to be detectable at lower fields

and whose transversal decay rate is too short for conventional imaging [5, 6, 50, 61, 62, 93–95]. Besides, with the advance of ultra-high field, UTE methods were proven to be especially useful for imaging of tissues with ultra-short T_2 such as bone [96].

Due to RF power absorption (i.e., specific absorption rate (SAR)) limitations, GRE-based sequences can be preferable at ultra-high field strengths. Scanning at high and ultra-high field also allows for increasing resolutions, which is very important in MSK imaging [6, 97]. Finally, in higher field the chemical shift between fat and water is bigger (~ 1040 Hz at 7T compared to 440 Hz at 3T), which creates a larger water-fat shift but it is advantageous for some fat suppression methods (such as fat saturation).

1.3 Fat-water quantification

Fat-water quantification is the assessment of the percentage of fat and water in a certain tissue, these two being the two main measurable components of human soft tissue. Increased presence of fat is often a marker of disease, and the amount of fat infiltration marks the stage of the disease. Two tissues mostly affected by pathologic fat infiltrations are the skeletal muscle and the liver. The skeletal muscle can exhibit a pathologic infiltration of fat in case of metabolic abnormalities [98], myopathies (e.g. muscular dystrophy [99, 100]) and muscle degeneration after injury [101, 102].

In the liver, accumulation of fat can happen in alcoholic diseases, non-alcoholic diseases and various hepatitis. Non-alcoholic liver diseases have a high prevalence in the western world, and they can range from simple steatosis to chronic liver disease [103, 104], therefore accurate fat quantification is of great importance for early diagnosis and better treatment.

The clinical standard for quantification of liver fat is non-targeted biopsy: an invasive procedure that is moreover subjected to sampling variability, and is thus not performed unless there is a clear pathological evidence. Alternatively, ^1H -NMR spectroscopy is the current gold standard for non-invasive fat quantification [105, 106], but it requires a complicated setup and does not offer whole organ coverage. Consequently, both biopsy and spectroscopy are prone to sampling errors – a drawback that can be overcome by whole organ fat quantification. As a result, over the years several MRI techniques have been developed for water-fat quantification.

1.3.1 ^1H MRS of liver fat

MR spectroscopy shows the frequency spectrum of the chemical species inside a specified voxel [107, 108]. Fat protons resonate at a different frequency with respect to water due to the methylene bonds and therefore they will appear as a different peak on the spectrum (see Fig. 1.11). The main resonant peak of the fat is 3.35 ppm (220 Hz at 1.5T) lower in frequency than the water peak. Integration of the relative area under the fat peak with respect to the area under the water peak gives an assessment of the fat content within the voxel [105]. Usually the quantification is performed taking into account the main fat peak.

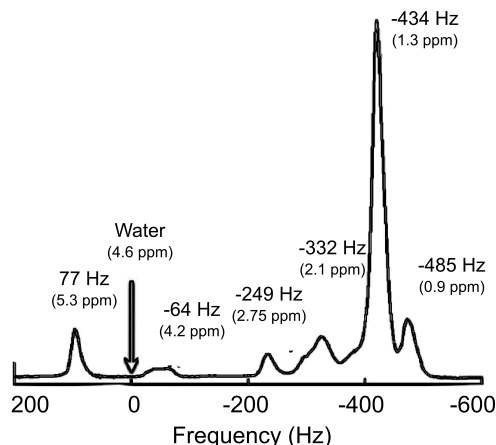


Figure 1.11: Fat spectrum from vegetable oil at 3T (source: [109]).

Nowadays liver ^1H -spectroscopy is an established non-invasive method for quantification of fat liver [8, 105, 110–112]. In the liver single-voxel spectroscopy is usually performed in different points of the organ because the fat concentration may vary depending on the location. A good shimming of the main magnetic field is important in order to avoid broadening of the line-width of the spectrum, and usually the acquisition spans multiple breath-holds in order to increase the signal-to-noise ratio. Specialized software is typically used for the analysis of the spectrum [106]. For accurate results, T_2 correction is usually needed to correct for susceptibility effects, especially in presence of iron [113, 114].

Although MR spectroscopy is considered the gold standard for liver fat quantification, its disadvantage is that it can be biased by sampling errors. Therefore, various MRI methods have been developed that aim to produce fat fraction maps instead of local fat percentage estimation.

1.3.2 Dixon methods

This concept was introduced in 1984 by Dixon [81], using a modified spin echo sequence. Dixon methods are a family of MR imaging techniques that typically rely on the acquisition of multiple images with different echo times, which are selected based on the phase difference between water and fat. With post-processing algorithms, these images can be used to separate water and fat components. Since water and fat signals resonate at different frequencies, they are periodically in-phase and out-of-phase with respect to each other, leading to a constructive or destructive interference in the acquired signal. This phenomenon can be used to separate fat and water components or quantify the relative percentage of the two species.

1.3.2.1 Two-point Dixon

Two-point Dixon refers to the acquisition of only two images, one of which has the fat and water components in each voxel in-phase, and the other out-of-phase (see Fig. 1.12). This is achieved by using echo times of 2.3 ms (out-of-phase) and 4.6 ms (in-phase) at 1.5T. These two images, called “in-phase” (I) and “out-of-phase” (O) can be described by the following equations [82]:

$$I = (W + F) \cdot \exp(i\phi_0) \quad (1.2)$$

$$O = (W - F) \cdot \exp(i\phi_0) \cdot \exp(i\phi) \quad (1.3)$$

where ϕ is the error phase due to the magnetic field inhomogeneity and ϕ_0 the error phase due to system imperfections, W is the signal contribution of the water component, and F is the signal contribution of fat. W and F can be extracted using the following equations:

$$W = 0.5 \cdot |I + O| \quad (1.4)$$

$$F = 0.5 \cdot |I - O| \quad (1.5)$$

To acquire quantitative results, the images should be corrected for T_1 (saturation) effects and T_2^* (decay) effects [115]. Recently, novel two-point Dixon techniques have been introduced where the echo times can be chosen in a flexible way with a trade-off between a signal-to-noise ratio (SNR) gain from the acquisition (thanks to the possibility of using shorter echo times) and an SNR loss from the separation because the signal difference between the “in-phase” and “out-of-phase” components is not as large as in the original method [116].

One major drawback of the two-point Dixon method is its sensitivity to B_0 inhomogeneities, because phase differences due to B_0 effects can interfere with chemical-based phase differences [117]. For this reason, acquiring more echoes is sometimes advisable, but it has the disadvantage of requiring longer acquisition times.

1.3.2.2 Three-point Dixon / Multi-point Dixon

These methods rely on the same principles as the two-point methods, but additional images at different echo times are acquired. The additional information can be used to estimate the true phase ϕ (see Eq. 1.3). This is important in order to account for B_0 inhomogeneities [117–119], noise bias, T_2^* decay or the multiple peaks of the fat spectrum [82].

Correcting for T_2^* decay is important since most of the chemical-shift based methods include acquisition of at least two echoes. During the two acquisitions there is signal decay, which should be corrected for and this effect becomes especially important in the presence of iron (i.e, iron and fat can co-exist in diffuse liver disease [120–123]).

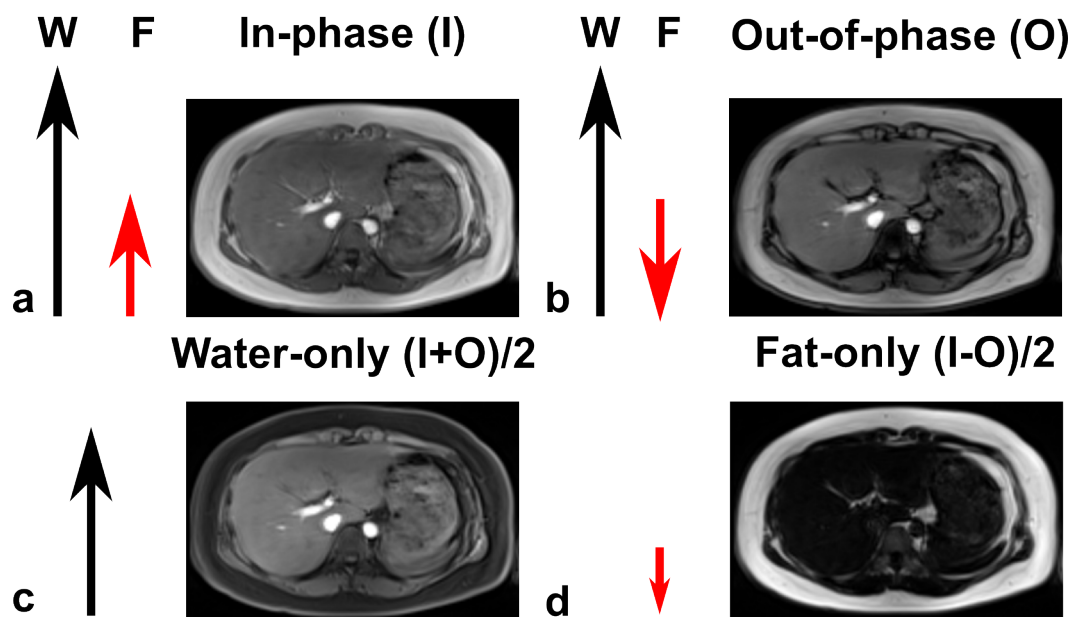


Figure 1.12: Two-point Dixon technique: post-processing of the in- phase (a) and out-of-phase (b) images allows under ideal conditions calculation of a water-only and a fat-only image.

Another issue that needs to be accounted for is that the Dixon methods usually assume that the fat is characterized by one main peak. However, it is well known today that actually the fat spectrum has multiple peaks (see Fig. 1.11). It has at least six distinct peaks [114] and their relative amplitudes and frequencies at 3T are approximately: 4.7 % (77 Hz), 3.9 % (-64 Hz), 0.6 % (-249 Hz), 12.0 % (-332 Hz), 70.0 % (-434 Hz), 8.8 % (-485 Hz). Due to the fact that at least two of them (i.e. the olefinic fat peak is 0.5 ppm away from the water peak [124]) are close to the water peak, they can be incorrectly mapped as water and thus introduce an error in the quantification.

Nowadays, Dixon techniques are broadly used at a clinical level, since their relation with spectroscopy has been well established [7, 125, 126]. The research interest though is moving to more robust and different multi-point water-fat quantification methods.

1.3.3 Fat-water imaging and simultaneous T_2^* quantification

Multiple-point techniques can be an extension of the Dixon techniques where the echo times are chosen in- and out-of-phase and then least squares fitting is used to extract the amplitudes of the water and fat components (more in chapter 5) [127].

Another approach, the so called IDEAL (Iterative Decomposition of water and fat with Echo Asymmetry and Least-squares estimation) introduced by Reeder et al. [121] is to acquire multiple echo times (i.e., at least six echo times for simultaneous T_2^* estimation) at optimal echo times for the separation [128, 129] and then use iterative fitting of a predefined model to separate the spectral components and estimate the transverse

relaxation times. Different models and fitting algorithms have been introduced in the recent years [128,130]. In general, the signal in a voxel at different echo times is modeled as follows [131]:

$$s(t) = \left(W \cdot \exp(-R_{2,W}^* t) + F \cdot \sum_{p=1}^P r_p \exp(i \cdot 2\pi \Delta f_p t) \exp(-R_{2,f_p}^* t) \right) \exp(i \cdot 2\pi \psi t)$$

where W and F are the amplitudes of the water and fat signals, $R_{2,W}^* = \frac{1}{T_{2,W}^*}$ and $T_{2,W}^*$ is the decay rate of water, $R_{2,f_p}^* = \frac{1}{T_{2,f_p}^*}$ the decay rate of the respective fat component, Δf_p the frequencies and r_p the relative amplitudes of the fat peaks, ψ the shift caused by the static field inhomogeneities.

Usually a common relaxation time is assumed for water and fat and one spectral component for the fat. The initial method was used for water-fat separation [121], but more recent IDEAL variations account for T_2^* and B_0 variations [128], while the inclusion of the multi-peak fat spectrum and direct spectrum estimation offers improved water-fat separation [130].

1.4 Aim of the thesis

MRI as diagnostic tool was introduced for soft tissue imaging and today even imaging of highly ordered molecular structures with fast signal decay (i.e., short T_2 values) is feasible. However, even if they achieve to yield high MR signal out of highly ordered structures most novel imaging techniques for short T_2 imaging require a rather complicated setup, challenging to be translated into clinical routine. Another area where MRI can be a useful diagnostic tool is tissue characterization, since it can offer information about the spectral components of tissue. However, in most of the applications, the quantitative measurements with MR are still not recognized as the gold standard that remains histology examination.

In this thesis, the focus of interest is on the transverse decay of the signal. The base for new sequence developments were standard spoiled gradient echo sequences exploiting the robustness of Fourier encoding. High field and ultra-high field was used in order to achieve fast high resolution imaging. The first part of the thesis is related to imaging of tissues with very short transverse signal decay. The aim was to develop a sequence that can capture the signal from short T_2 tissues, being at the same time adequate for use and integration at a clinical environment. The main focus of interest was musculoskeletal tissues such as menisci and ligaments, which have a high percentage of short T_2 components and therefore they are characterized by short T_2 values. Furthermore, the extension of the method for fat suppressed short TE imaging was also studied since fat suppression can increase the conspicuity in imaging of this kind of components. Fat suppression is extensively used in the clinics, but the effects on the visualization of short T_2 components remain unclear. Therefore, the effect of fat suppression on imaging and on the conspicuity of short T_2 species was investigated.

Finally, short echo time imaging was extended to a different and highly challenging imaging area; molecular imaging. The goal was to investigate the feasibility of using the same approach for imaging labeled cells in vivo.

The second part of the thesis is related to the analysis of the signal decay for quantification of fat percentage in the liver. Fat is an important biomarker for abnormalities that are increasing in western population such as non alcoholic liver disease. The motivation behind measuring fat percentage with MRI is that it offers diagnostic information in a non-invasive way. However, quantification with MRI still does not provide standard diagnostic values. The principal MR modality that has established a gold standard relation with histology is spectroscopy. The aim was to develop a fast sequence that offers volume coverage of the liver for fast and efficient clinical scanning and at the same time offers results close the gold standard spectroscopy values. A spoiled gradient echo was adapted for quantitative imaging of fat. A multi-echo gradient echo sequence was extended in order to be used with a powerful computational algorithm for the calculation of fat maps as well as relaxation maps. The clinical focus of interest in this case is liver imaging due to the high importance of detecting early stages of steatosis.

1.5 Outline of the thesis

This thesis is divided into two different parts, the first of which is focused on a qualitative and the second one on a quantitative development based on a spoiled gradient echo sequence.

The first part of the thesis has as main focus short echo time imaging. This part is extending over three different chapters. The first chapter, chapter 2 named “High-resolution Fourier-encoded sub-millisecond echo time musculoskeletal imaging at 3 Tesla and 7 Tesla”, is focused on the introduction of a short echo time sequence. A novel implementation of a variable echo time sequence is being presented. The optimization of the sequence for musculoskeletal imaging of short T_2 tissues of the knee such as menisci and ligaments is also described and experiments performed at high and ultra-high field are presented. The results show positive contrast imaging of short T_2 structures, achieved through long T_2 components suppression by the use of subtraction of a later echo. Long T_2 suppression is shown to improve conspicuity of short T_2 tissues such as the menisci and the ligaments. In addition, preliminary results from an application of the proposed sequence for imaging of the Achilles tendon at 7T is being described. In chapter 3, the addition of fat suppression in the form of water excitation is investigated. The short echo time sequence is modified with the addition of binomial sub-pulses. The effect of the fat suppression block on the signal of short T_2 species is analyzed and a comparison of the binomial pulses preparation with the commonly used FATSAT pre-pulses on the conspicuity of short T_2 tissues is performed. Finally, in chapter 4 the clinical focus is moved to a different application of the short echo time sequence: molecular imaging. The sequence is used for detection of pancreatic islets labeled with superparamagnetic iron oxide and transplanted into the liver. A double contrast protocol is used in order to yield positive contrast images and advanced ways of producing positive contrast are

being explored.

The second part of the thesis is focused on water-fat liver imaging. In chapter 5, the development of a novel method for simultaneous water-fat imaging and T_2^* quantification is being described. The adaptation of a multi-echo gradient echo sequence for using a powerful post-processing algorithm originating from the spectroscopy domain is being described. Preliminary results from healthy volunteers at 3T are being presented from the comparison of the proposed method with the two-point Dixon method.

References

- [1] R. Damadian, “Tumor detection by nuclear magnetic resonance,” *Science (New York, N. Y.)*, vol. 171, pp. 1151–1153, Mar. 1971. PMID: 5544870.
- [2] G. E. Gold, J. M. Pauly, A. Macovski, and R. J. Herfkens, “MR spectroscopic imaging of collagen: tendons and knee menisci,” *Magn Reson Med*, vol. 34, pp. 647–654, Nov. 1995. PMID: 8544684.
- [3] G. E. Gold, E. Han, J. Stainsby, G. Wright, J. Brittain, and C. Beaulieu, “Musculoskeletal MRI at 3.0 t: relaxation times and image contrast,” *AJR Am J Roentgenol*, vol. 183, pp. 343–351, Aug. 2004. PMID: 15269023.
- [4] F. Eckstein, F. Cicuttini, J.-P. Raynaud, J. C. Waterton, and C. Peterfy, “Magnetic resonance imaging (MRI) of articular cartilage in knee osteoarthritis (OA): morphological assessment,” *Osteoarthritis Cartilage*, vol. 14 Suppl A, pp. A46–75, 2006. PMID: 16713720.
- [5] G. H. Welsch, V. Juras, P. Szomolanyi, T. C. Mamisch, P. Baer, C. Kronnerwetter, M. Blanke, H. Fujita, and S. Trattnig, “Magnetic resonance imaging of the knee at 3 and 7 tesla: a comparison using dedicated multi-channel coils and optimised 2D and 3D protocols,” *Eur Radiol*, Apr. 2012. PMID: 22538628.
- [6] S. Trattnig, S. Zbýň, B. Schmitt, K. Friedrich, V. Juras, P. Szomolanyi, and W. Bogner, “Advanced MR methods at ultra-high field (7 tesla) for clinical musculoskeletal applications,” *Eur Radiol*, June 2012. PMID: 22688127.
- [7] B. Guiu, R. Loffroy, J.-M. Petit, S. Aho, D. Ben Salem, D. Masson, P. Hillon, J.-P. Cercueil, and D. Krause, “Mapping of liver fat with triple-echo gradient echo imaging: validation against 3.0-t proton MR spectroscopy,” *Eur Radiol*, vol. 19, pp. 1786–1793, July 2009. PMID: 19247667.
- [8] M. Hajek, M. Dezortova, D. Wagnerova, A. Skoch, L. Voska, I. Hejlova, and P. Trunecka, “MR spectroscopy as a tool for in vivo determination of steatosis in liver transplant recipients,” *Magn Reson Mater Phy*, vol. 24, pp. 297–304, Oct. 2011. PMID: 21744232.
- [9] A. Haase, J. Frahm, D. Matthaei, W. Hancic, and K.-D. Merboldt, “FLASH imaging. rapid NMR imaging using low flip-angle pulses,” *Journal of Magnetic Resonance (1969)*, vol. 67, pp. 258–266, Apr. 1986.
- [10] D. Weishaupt, V. D. Köchli, and B. Marincek, *How Does MRI Work?: An Introduction to the Physics and Function of Magnetic Resonance Imaging*. Springer, Jan. 2006.
- [11] E. M. Haacke, R. W. Brown, M. R. Thompson, and R. Venkatesan, *Magnetic Resonance Imaging: Physical Principles and Sequence Design*. 1999. John Wiley & Sons, New York.
- [12] M. A. Bernstein, K. F. King, and X. J. Zhou, *Handbook of MRI Pulse Sequences*. Elsevier, Sept. 2004.
- [13] D. W. McRobbie, *MRI from picture to proton*. Cambridge, UK; New York: Cambridge University Press, 2007.
- [14] Y. Zur, “Design of improved spectral-spatial pulses for routine clinical use,” *Magn Reson Med*, vol. 43, pp. 410–420, Mar. 2000. PMID: 10725884.

- [15] J. H. d. Boef, C. M. J. v. Uijen, and C. D. Holzschere, "Multiple-slice NMR imaging by three-dimensional fourier zeugmatography," *Physics in Medicine and Biology*, vol. 29, p. 857, July 1984.
- [16] M. M. Barreto, P. P. Rafful, R. S. Rodrigues, G. Zanetti, B. Hochegger, A. S. Souza Jr., M. D. Guimarães, and E. Marchiori, "Correlation between computed tomographic and magnetic resonance imaging findings of parenchymal lung diseases," *European Journal of Radiology*.
- [17] D. O. Kuethe, A. Caprihan, E. Fukushima, and R. A. Waggoner, "Imaging lungs using inert fluorinated gases," *Magn Reson Med*, vol. 39, pp. 85–88, Jan. 1998. PMID: 9438441.
- [18] H. U. Kauczor and K. F. Kreitner, "Contrast-enhanced MRI of the lung," *European journal of radiology*, vol. 34, pp. 196–207, June 2000. PMID: 10927161.
- [19] M. Wielpütz and H.-U. Kauczor, "MRI of the lung: state of the art," *Diagn Interv Radiol*, vol. 18, pp. 344–353, Aug. 2012. PMID: 22434450.
- [20] C. J. Bergin, J. M. Pauly, and A. Macovski, "Lung parenchyma: projection reconstruction MR imaging," *Radiology*, vol. 179, pp. 777–781, June 1991. PMID: 2027991.
- [21] C. J. Bergin, D. C. Noll, J. M. Pauly, G. H. Glover, and A. Macovski, "MR imaging of lung parenchyma: a solution to susceptibility," *Radiology*, vol. 183, pp. 673–676, June 1992. PMID: 1584917.
- [22] P. D. Gatehouse, R. W. Thomas, M. D. Robson, G. Hamilton, A. H. Herlihy, and G. M. Bydder, "Magnetic resonance imaging of the knee with ultrashort TE pulse sequences," *Magn Reson Imaging*, vol. 22, pp. 1061–1067, Oct. 2004. PMID: 15527992.
- [23] M. Robson, M. Benjamin, P. Gishen, and G. Bydder, "Magnetic resonance imaging of the achilles tendon using ultrashort TE (UTE) pulse sequences," *Clin Radiology*, vol. 59, pp. 727–735, Aug. 2004.
- [24] P. D. Gatehouse and G. M. Bydder, "Magnetic resonance imaging of short t2 components in tissue," *Clin Radiology*, vol. 58, pp. 1–19, Jan. 2003. PMID: 12565203.
- [25] Y. Wu, J. L. Ackerman, D. A. Chesler, L. Graham, Y. Wang, and M. J. Glimcher, "Density of organic matrix of native mineralized bone measured by water- and fat-suppressed proton projection MRI," *Magn Reson Med*, vol. 50, pp. 59–68, July 2003. PMID: 12815679.
- [26] K. E. Chappell, N. Patel, P. D. Gatehouse, J. Main, B. K. Puri, S. D. Taylor-Robinson, and G. M. Bydder, "Magnetic resonance imaging of the liver with ultrashort TE (UTE) pulse sequences," *J Magn Reson Imaging*, vol. 18, pp. 709–713, Dec. 2003. PMID: 14635156.
- [27] T. Movin, M. Kristoffersen-Wiberg, A. Shalabi, A. Gad, P. Aspelin, and C. Rolf, "Intra-tendinous alterations as imaged by ultrasound and contrast medium-enhanced magnetic resonance in chronic achillodynia," *Foot Ankle Int.*, vol. 19, pp. 311–317, May 1998. PMID: 9622422.
- [28] R. M. Henkelman, G. J. Stanisz, and S. J. Graham, "Magnetization transfer in MRI: a review," *NMR in biomedicine*, vol. 14, pp. 57–64, Apr. 2001. PMID: 11320533.
- [29] M. D. Robson, P. D. Gatehouse, M. Bydder, and G. M. Bydder, "Magnetic resonance: an introduction to ultrashort TE (UTE) imaging," *J Comput Assist Tomogr*, vol. 27, pp. 825–846, Dec. 2003. PMID: 14600447.

-
- [30] F. Springer, G. Steidle, P. Martirosian, C. D. Claussen, and F. Schick, “Effects of in-pulse transverse relaxation in 3D ultrashort echo time sequences: analytical derivation, comparison to numerical simulation and experimental application at 3T,” *J Magn Reson*, vol. 206, pp. 88–96, Sept. 2010. PMID: 20637661.
- [31] E. M. Shapiro, S. Skrtic, K. Sharer, J. M. Hill, C. E. Dunbar, and A. P. Koretsky, “MRI detection of single particles for cellular imaging,” *Proceedings of the National Academy of Sciences of the United States of America*, vol. 101, pp. 10901–10906, July 2004. PMID: 15256592.
- [32] J. W. M. Bulte and D. L. Kraitchman, “Iron oxide MR contrast agents for molecular and cellular imaging,” *NMR Biomed*, vol. 17, pp. 484–499, Nov. 2004. PMID: 15526347.
- [33] *Molecular Imaging and Contrast Agent Database (MICAD)*. Bethesda (MD): National Center for Biotechnology Information (US), 2004. PMID: 20641179.
- [34] C. H. Cunningham, T. Arai, P. C. Yang, M. V. McConnell, J. M. Pauly, and S. M. Conolly, “Positive contrast magnetic resonance imaging of cells labeled with magnetic nanoparticles,” *Magn Reson Med*, vol. 53, pp. 999–1005, May 2005. PMID: 15844142.
- [35] T. Cukur, M. Yamada, W. R. Overall, P. Yang, and D. G. Nishimura, “Positive contrast with alternating repetition time SSFP (PARTS): a fast imaging technique for SPIO-Labeled cells,” *Magn Reson Med*, vol. 63, pp. 427–437, Feb. 2010. PMID: 20099331
PMCID: PMC3158609.
- [36] S. A. Anderson, J. Glod, A. S. Arbab, M. Noel, P. Ashari, H. A. Fine, and J. A. Frank, “Noninvasive MR imaging of magnetically labeled stem cells to directly identify neovasculature in a glioma model,” *Blood*, vol. 105, pp. 420–425, Jan. 2005. PMID: 15331444.
- [37] D. Jiráček, J. Kríz, V. Herynek, B. Andersson, P. Girman, M. Burian, F. Saudek, and M. Hájek, “MRI of transplanted pancreatic islets,” *Magn Reson Med*, vol. 52, pp. 1228–1233, Dec. 2004. PMID: 15562474.
- [38] Z. Berková, D. Jirák, K. Zacharovová, J. Kriz, A. Lodererová, P. Girman, T. Koblas, E. Dovolilová, M. Vancová, M. Hajek, and F. Saudek, “Labeling of pancreatic islets with iron oxide nanoparticles for in vivo detection with magnetic resonance,” *Transplantation*, vol. 85, pp. 155–159, Jan. 2008. PMID: 18192927.
- [39] H. S. Kim, Y. Choi, I. C. Song, and W. K. Moon, “Magnetic resonance imaging and biological properties of pancreatic islets labeled with iron oxide nanoparticles,” *NMR in biomedicine*, vol. 22, pp. 852–856, Oct. 2009. PMID: 19489018.
- [40] F. Ris, M. Lepetit-Coiffe, P. Meda, L. A. Crowe, C. Toso, M. Armanet, N. Niclauss, G. Parnaud, L. Giovannoni, D. Bosco, P. Morel, J.-P. Vallee, and T. Berney, “Assessment of human islet labeling with clinical grade iron nanoparticles prior to transplantation for graft monitoring by MRI,” *Cell transplantation*, vol. 19, no. 12, pp. 1573–1585, 2010. PMID: 20719068.
- [41] K. Zacharovová, Z. Berková, D. Jiráček, V. Herynek, M. Vancová, E. Dovolilová, and F. Saudek, “Processing of superparamagnetic iron contrast agent ferucarbotran in transplanted pancreatic islets,” *Contrast Media Mol Imaging*, vol. 7, pp. 485–493, Dec. 2012. PMID: 22991314.

- [42] B. P. Barnett, J. Ruiz-Cabello, P. Hota, R. Ouwerkerk, M. J. Shablott, C. Lauzon, P. Walczak, W. D. Gilson, V. P. Chacko, D. L. Kraitchman, A. Arepally, and J. W. M. Bulte, "Use of perfluorocarbon nanoparticles for non-invasive multimodal cell tracking of human pancreatic islets," *Contrast Media Mol Imaging*, vol. 6, no. 4, pp. 251–259, 2011. PMID: 21861285 PMCID: PMC3160722.
- [43] B. Zhang, B. Jiang, Y. Chen, H. Huang, Q. Xie, M. Kang, H. Zhang, C. Zhai, and Y. Wu, "Detection of viability of transplanted beta cells labeled with a novel contrast agent – polyvinylpyrrolidone-coated superparamagnetic iron oxide nanoparticles by magnetic resonance imaging," *Contrast Media Mol Imaging*, vol. 7, no. 1, p. 35–44, 2012.
- [44] C. Toso, J.-P. Vallee, P. Morel, F. Ris, S. Demuylder-Mischler, M. Lepetit-Coiffe, N. Marangon, F. Saudek, A. M. James Shapiro, D. Bosco, and T. Berney, "Clinical magnetic resonance imaging of pancreatic islet grafts after iron nanoparticle labeling," *Am. J. Transplant.*, vol. 8, pp. 701–706, Mar. 2008. PMID: 18294167.
- [45] J. Pauly, S. Conolly, D. Nishimura, and A. Macovski, "Slice-selective excitation for very short t_2 species," in *Proceedings of SMRM 8th Annual meeting*, vol. 28, (Amsterdam, The Netherlands, 1989), 1989.
- [46] D. Mentrup and H. Eggers, "Signal decay correction in 2D ultra-short echo time imaging," *Magma (New York, N.Y.)*, vol. 19, pp. 62–70, May 2006. PMID: 16779561.
- [47] J.-F. Nielsen and K. S. Nayak, "Pulse sequences for phase-contrast SSFP imaging from a single steady-state," *Proc Int Soc Magn Reson Med*, vol. 14, p. 879, May 2006. PMID: 17387380 PMCID: PMC1832109.
- [48] J. Du, A. M. Takahashi, W. C. Bae, C. B. Chung, and G. M. Bydder, "Dual inversion recovery, ultrashort echo time (DIR UTE) imaging: creating high contrast for short- t_2 species," *Magn Reson Med*, vol. 63, pp. 447–455, Feb. 2010. PMID: 20099332.
- [49] J. P. Wansapura, B. L. Daniel, J. Pauly, and K. Butts, "Temperature mapping of frozen tissue using eddy current compensated half excitation RF pulses," *Magn Reson Med*, vol. 46, no. 5, p. 985–992, 2001.
- [50] G. H. Glover, J. M. Pauly, and K. M. Bradshaw, "Boron-11 imaging with a three-dimensional reconstruction method," *J Magn Reson Imaging*, vol. 2, pp. 47–52, Feb. 1992. PMID: 1623280.
- [51] J. Rahmer, P. Börnert, J. Groen, and C. Bos, "Three-dimensional radial ultrashort echo-time imaging with t_2 adapted sampling," *Magn Reson Med*, vol. 55, pp. 1075–1082, May 2006. PMID: 16538604.
- [52] P. E. Z. Larson, P. T. Gurney, K. Nayak, G. E. Gold, J. M. Pauly, and D. G. Nishimura, "Designing long- t_2 suppression pulses for ultrashort echo time imaging," *Magn Reson Med*, vol. 56, pp. 94–103, July 2006. PMID: 16724304.
- [53] J. Rahmer, U. Blume, and P. Börnert, "Selective 3D ultrashort TE imaging: comparison of "dual-echo" acquisition and magnetization preparation for improving short- t_2 contrast," *Magn Reson Mater Phy*, vol. 20, pp. 83–92, Apr. 2007. PMID: 17354002.
- [54] S. Hafner, "Fast imaging in liquids and solids with the back-projection low angle ShoT (BLAST) technique," *Magn Reson Imaging*, vol. 12, no. 7, pp. 1047–1051, 1994. PMID: 7997092.

- [55] D. Idiyatullin, C. Corum, J.-Y. Park, and M. Garwood, “Fast and quiet MRI using a swept radiofrequency,” *Journal of magnetic resonance (San Diego, Calif.: 1997)*, vol. 181, pp. 342–349, Aug. 2006. PMID: 16782371.
- [56] M. Weiger, M. Stampanoni, and K. P. Pruessmann, “Direct depiction of bone microstructure using MRI with zero echo time,” *Bone*, vol. 54, pp. 44–47, May 2013. PMID: 23356986.
- [57] M. Weiger, K. P. Pruessmann, A.-K. Bracher, S. Köhler, V. Lehmann, U. Wolfram, F. Hennel, and V. Rasche, “High-resolution ZTE imaging of human teeth,” *NMR Biomed*, vol. 25, pp. 1144–1151, Oct. 2012. PMID: 22290744.
- [58] Y. Qian and F. E. Boada, “Acquisition-weighted stack of spirals for fast high-resolution three-dimensional ultra-short echo time MR imaging,” *Magn Reson Med*, vol. 60, pp. 135–145, July 2008. PMID: 18581326.
- [59] Y. Qian, A. A. Williams, C. R. Chu, and F. E. Boada, “Multicomponent t_2^* mapping of knee cartilage: technical feasibility ex vivo,” *Magn Reson Med*, vol. 64, pp. 1426–1431, Nov. 2010. PMID: 20865752.
- [60] Y. Qian, A. A. Williams, C. R. Chu, and F. E. Boada, “High-resolution ultrashort echo time (UTE) imaging on human knee with AWSOS sequence at 3.0 t,” *Journal of magnetic resonance imaging: JMRI*, vol. 35, pp. 204–210, Jan. 2012. PMID: 22002811.
- [61] F. E. Boada, J. S. Gillen, G. X. Shen, S. Y. Chang, and K. R. Thulborn, “Fast three dimensional sodium imaging,” *Magn Reson Med*, vol. 37, pp. 706–715, May 1997. PMID: 9126944.
- [62] A. Lu, I. C. Atkinson, T. C. Claiborne, F. C. Damen, and K. R. Thulborn, “Quantitative sodium imaging with a flexible twisted projection pulse sequence,” *Magn Reson Med*, vol. 63, pp. 1583–1593, June 2010. PMID: 20512862.
- [63] D. M. Grodzki, P. M. Jakob, and B. Heismann, “Ultrashort echo time imaging using pointwise encoding time reduction with radial acquisition (PETRA),” *Magn Reson Med*, vol. 67, pp. 510–518, Feb. 2012. PMID: 21721039.
- [64] M. L. Lauzon and B. K. Rutt, “Effects of polar sampling in k-space,” *Magn Reson Med*, vol. 36, no. 6, p. 940–949, 1996.
- [65] C. A. Mistretta, O. Wieben, J. Velikina, W. Block, J. Perry, Y. Wu, K. Johnson, and Y. Wu, “Highly constrained backprojection for time-resolved MRI,” *Magn Reson Med*, vol. 55, pp. 30–40, Jan. 2006. PMID: 16342275 PMCID: PMC2366054.
- [66] J. G. Pipe, “Reconstructing MR images from undersampled data: data-weighting considerations,” *Magn Reson Med*, vol. 43, pp. 867–875, June 2000. PMID: 10861882.
- [67] I. C. Atkinson, A. Lu, and K. R. Thulborn, “Characterization and correction of system delays and eddy currents for MR imaging with ultrashort echo-time and time-varying gradients,” *Magnetic Resonance in Medicine*, vol. 62, no. 2, p. 532–537, 2009.
- [68] D. C. Peters, J. A. Derbyshire, and E. R. McVeigh, “Centering the projection reconstruction trajectory: reducing gradient delay errors,” *Magn Reson Med*, vol. 50, pp. 1–6, July 2003. PMID: 12815671.
- [69] P. Schmalbrock, “A method to achieve very short echo times for submillimeter resolution imaging,” in *Proceedings 11th Scientific Meeting, International Society for Magnetic Resonance in Medicine*, (New York, USA), p. 3934, 1992.

- [70] K. Ying, P. Schmalbrock, and B. Clymer, "Echo-time reduction for submillimeter resolution imaging with a 3D phase encode time reduced acquisition method," *Magn Reson Med*, vol. 33, pp. 82–87, Jan. 1995. PMID: 7891540.
- [71] A. Techawiboonwong, H. K. Song, and F. W. Wehrli, "In vivo MRI of submillisecond t_2 species with two-dimensional and three-dimensional radial sequences and applications to the measurement of cortical bone water," *NMR Biomed*, vol. 21, pp. 59–70, Jan. 2008. PMID: 17506113.
- [72] H. K. Song and F. W. Wehrli, "Variable TE gradient and spin echo sequences for in vivo MR microscopy of short t_2 species," *Magn Reson Med*, vol. 39, pp. 251–258, Feb. 1998. PMID: 9469708.
- [73] A. F. Stalder, D. V. Elverfeldt, D. Paul, J. Hennig, and M. Markl, "Variable echo time imaging: signal characteristics of 1-m gadobutrol contrast agent at 1.5 and 3T," *Magn Reson Med*, vol. 59, pp. 113–123, Jan. 2008. PMID: 18058940.
- [74] G. McGibney, M. R. Smith, S. T. Nichols, and A. Crawley, "Quantitative evaluation of several partial fourier reconstruction algorithms used in MRI," *Magn Reson Med*, vol. 30, pp. 51–59, July 1993. PMID: 8371675.
- [75] L. Gubin, B. Polyak, and E. Raik, "The method of projections for finding the common point of convex sets," *USSR Computational Mathematics and Mathematical Physics*, vol. 7, no. 6, pp. 1–24, 1967.
- [76] M. S. Sussman, J. M. Pauly, and G. A. Wright, "Design of practical t_2 -selective RF excitation (TELEX) pulses," *Magn Reson Med*, vol. 40, pp. 890–899, Dec. 1998. PMID: 9840834.
- [77] P. E. Z. Larson, S. M. Conolly, J. M. Pauly, and D. G. Nishimura, "Using adiabatic inversion pulses for long- t_2 suppression in ultrashort echo time (UTE) imaging," *Magn Reson Med*, vol. 58, pp. 952–961, Nov. 2007. PMID: 17969119.
- [78] G. Korosoglou, L. Tang, D. Kedziorek, K. Cosby, W. D. Gilson, E.-J. Vonken, M. Schär, D. Sosnovik, D. L. Kraitchman, R. G. Weiss, R. Weissleder, and M. Stuber, "Positive contrast MR-lymphography using inversion recovery with ON-resonant water suppression (IRON)," *J Magn Reson Imaging*, vol. 27, pp. 1175–1180, May 2008. PMID: 18425827.
- [79] J. Du, M. Bydder, A. M. Takahashi, M. Carl, C. B. Chung, and G. M. Bydder, "Short t_2 contrast with three-dimensional ultrashort echo time imaging," *Magn Reson Imaging*, vol. 29, pp. 470–482, May 2011. PMID: 21440400.
- [80] R. Rakow-Penner, B. Daniel, H. Yu, A. Sawyer-Glover, and G. H. Glover, "Relaxation times of breast tissue at 1.5T and 3T measured using IDEAL," *J Magn Reson Imaging*, vol. 23, pp. 87–91, Jan. 2006. PMID: 16315211.
- [81] W. T. Dixon, "Simple proton spectroscopic imaging," *Radiology*, vol. 153, pp. 189–194, Oct. 1984.
- [82] J. Ma, "Dixon techniques for water and fat imaging," *J Magn Reson Imaging*, vol. 28, pp. 543–558, Sept. 2008. PMID: 18777528.
- [83] E. M. Delfaut, J. Beltran, G. Johnson, J. Rousseau, X. Marchandise, and A. Cotten, "Fat suppression in MR imaging: techniques and pitfalls," *Radiographics*, vol. 19, pp. 373–382, Apr. 1999. PMID: 10194785.

- [84] P. D. Gatehouse and G. M. Bydder, “Magnetic resonance imaging of short t2 components in tissue,” *Clinical Radiology*, vol. 58, pp. 1–19, Jan. 2003. PMID: 12565203.
- [85] T. A. Bley, O. Wieben, C. J. François, J. H. Brittain, and S. B. Reeder, “Fat and water magnetic resonance imaging,” *J Magn Reson Imaging*, vol. 31, pp. 4–18, Jan. 2010. PMID: 20027567.
- [86] C. Glaser, S. Faber, F. Eckstein, H. Fischer, V. Springer, L. Heudorfer, T. Stammberger, K. H. Englmeier, and M. Reiser, “Optimization and validation of a rapid high-resolution t1-w 3D FLASH water excitation MRI sequence for the quantitative assessment of articular cartilage volume and thickness,” *Magn Reson Imaging*, vol. 19, pp. 177–185, Feb. 2001. PMID: 11358655.
- [87] V. Vasilevska, U. Szeimies, and A. Stäbler, “Magnetic resonance imaging signs of iliotibial band friction in patients with isolated medial compartment osteoarthritis of the knee,” *Skeletal Radiol.*, vol. 38, pp. 871–875, Sept. 2009. PMID: 19484234.
- [88] J. Frahm, A. Haase, W. Hänicke, D. Matthaei, H. Bomsdorf, and T. Helzel, “Chemical shift selective MR imaging using a whole-body magnet,” *Radiology*, vol. 156, pp. 441–444, Aug. 1985. PMID: 4011907.
- [89] A. Haase, J. Frahm, W. Hänicke, and D. Matthaei, “1H NMR chemical shift selective (CHESS) imaging,” *Phys Med Biol*, vol. 30, pp. 341–344, Apr. 1985. PMID: 4001160.
- [90] G. M. Bydder, J. M. Pennock, R. E. Steiner, S. Khenia, J. A. Payne, and I. R. Young, “The short TI inversion recovery sequence—an approach to MR imaging of the abdomen,” *Magn Reson Imaging*, vol. 3, no. 3, pp. 251–254, 1985. PMID: 4079672.
- [91] C. H. Meyer, J. M. Pauly, A. Macovski, and D. G. Nishimura, “Simultaneous spatial and spectral selective excitation,” *Magn Reson Med*, vol. 15, pp. 287–304, Aug. 1990. PMID: 2392053.
- [92] F. Schick, “Simultaneous highly selective MR water and fat imaging using a simple new type of spectral-spatial excitation,” *Magn Reson Med*, vol. 40, pp. 194–202, Aug. 1998. PMID: 9702701.
- [93] S. Nilles-Vallespin, M.-A. Weber, M. Bock, A. Bongers, P. Speier, S. E. Combs, J. Wöhrle, F. Lehmann-Horn, M. Essig, and L. R. Schad, “3D radial projection technique with ultrashort echo times for sodium MRI: clinical applications in human brain and skeletal muscle,” *Magn Reson Med*, vol. 57, pp. 74–81, Jan. 2007. PMID: 17191248.
- [94] R. R. Regatte and M. E. Schweitzer, “Ultra-high-field MRI of the musculoskeletal system at 7.0T,” *J Magn Reson Imaging*, vol. 25, pp. 262–269, Feb. 2007. PMID: 17260399.
- [95] R. Krug, C. Stehling, D. A. C. Kelley, S. Majumdar, and T. M. Link, “Imaging of the musculoskeletal system in vivo using ultra-high field magnetic resonance at 7 t,” *Investigative Radiology*, vol. 44, pp. 613–618, Sept. 2009.
- [96] R. Krug, P. E. Z. Larson, C. Wang, A. J. Burghardt, D. A. C. Kelley, T. M. Link, X. Zhang, D. B. Vigneron, and S. Majumdar, “Ultrashort echo time MRI of cortical bone at 7 tesla field strength: A feasibility study,” *J Magn Reson Imaging*, vol. 34, pp. 691–695, Sept. 2011. PMID: 21769960.
- [97] E. Moser, F. Stahlberg, M. E. Ladd, and S. Trattnig, “7-t MR—from research to clinical applications?,” *NMR Biomed*, vol. 25, pp. 695–716, May 2012. PMID: 22102481.

- [98] M. Boettcher, J. Machann, N. Stefan, C. Thamer, H.-U. Häring, C. D. Claussen, A. Fritsche, and F. Schick, “Intermuscular adipose tissue (IMAT): association with other adipose tissue compartments and insulin sensitivity,” *J Magn Reson Imaging*, vol. 29, pp. 1340–1345, June 2009. PMID: 19422021.
- [99] T. A. L. Wren, S. Bluml, L. Tseng-Ong, and V. Gilsanz, “Three-point technique of fat quantification of muscle tissue as a marker of disease progression in duchenne muscular dystrophy: preliminary study,” *AJR. Am J Roentgenol.*, vol. 190, pp. W8–12, Jan. 2008. PMID: 18094282.
- [100] M. Gloor, S. Fasler, A. Fischmann, T. Haas, O. Bieri, K. Heinimann, S. G. Wetzel, K. Scheffler, and D. Fischer, “Quantification of fat infiltration in oculopharyngeal muscular dystrophy: comparison of three MR imaging methods,” *J Magn Reson Imaging*, vol. 33, pp. 203–210, Jan. 2011. PMID: 21182140.
- [101] C. W. A. Pfirrmann, M. R. Schmid, M. Zanetti, B. Jost, C. Gerber, and J. Hodler, “Assessment of fat content in supraspinatus muscle with proton MR spectroscopy in asymptomatic volunteers and patients with supraspinatus tendon lesions,” *Radiology*, vol. 232, pp. 709–715, Sept. 2004. PMID: 15333791.
- [102] D. C. Karampinos, H. Yu, A. Shimakawa, T. M. Link, and S. Majumdar, “Chemical shift-based water/fat separation in the presence of susceptibility-induced fat resonance shift,” *Magn Reson Med*, vol. 68, pp. 1495–1505, Nov. 2012. PMID: 22247024.
- [103] J. D. Browning, L. S. Szczepaniak, R. Dobbins, P. Nuremberg, J. D. Horton, J. C. Cohen, S. M. Grundy, and H. H. Hobbs, “Prevalence of hepatic steatosis in an urban population in the united states: impact of ethnicity,” *Hepatology*, vol. 40, pp. 1387–1395, Dec. 2004. PMID: 15565570.
- [104] S. M. Mazhar, M. Shiehorteza, and C. B. Sirlin, “Noninvasive assessment of hepatic steatosis,” *Clin. Gastroenterol. Hepatol.*, vol. 7, pp. 135–140, Feb. 2009. PMID: 19118644.
- [105] C. Thomsen, U. Becker, K. Winkler, P. Christoffersen, M. Jensen, and O. Henriksen, “Quantification of liver fat using magnetic resonance spectroscopy,” *Magn Reson Imaging*, vol. 12, no. 3, pp. 487–495, 1994.
- [106] L. S. Szczepaniak, P. Nuremberg, D. Leonard, J. D. Browning, J. S. Reingold, S. Grundy, H. H. Hobbs, and R. L. Dobbins, “Magnetic resonance spectroscopy to measure hepatic triglyceride content: prevalence of hepatic steatosis in the general population,” *Am. J. Physiol. Endocrinol. Metab.*, vol. 288, pp. E462–E468, Feb. 2005.
- [107] P. A. Bottomley, “Spatial localization in NMR spectroscopy in vivo,” *Ann N Y Acad Sci*, vol. 508, pp. 333–348, 1987. PMID: 3326459.
- [108] J. Frahm, H. Bruhn, M. L. Gyngell, K. D. Merboldt, W. Hänicke, and R. Sauter, “Localized high-resolution proton NMR spectroscopy using stimulated echoes: initial applications to human brain in vivo,” *Magn Reson Med*, vol. 9, pp. 79–93, Jan. 1989. PMID: 2540396.
- [109] S. B. Reeder and C. B. Sirlin, “Quantification of liver fat with magnetic resonance imaging,” *Magn Reson Imaging Clin N Am*, vol. 18, pp. 337–357, ix, Aug. 2010. PMID: 21094444.

- [110] R. Longo, C. Ricci, F. Masutti, R. Vidimari, L. S. Crocè, L. Bercich, C. Tiribelli, and L. Dalla Palma, “Fatty infiltration of the liver. quantification by 1H localized magnetic resonance spectroscopy and comparison with computed tomography,” *Invest Radiol*, vol. 28, pp. 297–302, Apr. 1993. PMID: 8478169.
- [111] R. Longo, P. Pollesello, C. Ricci, F. Masutti, B. J. Kvam, L. Bercich, L. S. Crocè, P. Grigoletto, S. Paoletti, and B. de Bernard, “Proton MR spectroscopy in quantitative in vivo determination of fat content in human liver steatosis,” *J Magn Reson Imaging*, vol. 5, pp. 281–285, June 1995. PMID: 7633104.
- [112] F. Springer, J. Machann, C. D. Claussen, F. Schick, and N. F. Schwenzer, “Liver fat content determined by magnetic resonance imaging and spectroscopy,” *World J Gastroenterol*, vol. 16, pp. 1560–1566, Apr. 2010. PMID: 20355234.
- [113] N. Pineda, P. Sharma, Q. Xu, X. Hu, M. Vos, and D. R. Martin, “Measurement of hepatic lipid: high-speed t2-corrected multiecho acquisition at 1H MR spectroscopy—a rapid and accurate technique,” *Radiology*, vol. 252, pp. 568–576, Aug. 2009. PMID: 19546430.
- [114] G. Hamilton, T. Yokoo, M. Bydder, I. Cruite, M. E. Schroeder, C. B. Sirlin, and M. S. Middleton, “In vivo characterization of the liver fat ¹H MR spectrum,” *NMR Biomed*, vol. 24, pp. 784–790, Aug. 2011. PMID: 21834002.
- [115] M. Bydder, T. Yokoo, G. Hamilton, M. S. Middleton, A. D. Chavez, J. B. Schwimmer, J. E. Lavine, and C. B. Sirlin, “Relaxation effects in the quantification of fat using gradient echo imaging,” *Magn Reson Imaging*, vol. 26, pp. 347–359, Apr. 2008. PMID: 18093781.
- [116] H. Eggers, B. Brendel, A. Duijndam, and G. Herigault, “Dual-echo dixon imaging with flexible choice of echo times,” *Magn Reson Med*, vol. 65, pp. 96–107, Jan. 2011. PMID: 20860006.
- [117] G. H. Glover and E. Schneider, “Three-point dixon technique for true water/fat decomposition with b0 inhomogeneity correction,” *Magn Reson Med*, vol. 18, pp. 371–383, Apr. 1991. PMID: 2046518.
- [118] H. N. Yeung and D. W. Kormos, “Separation of true fat and water images by correcting magnetic field inhomogeneity in situ,” *Radiology*, vol. 159, pp. 783–786, June 1986. PMID: 3704157.
- [119] G. H. Glover, “Multipoint dixon technique for water and fat proton and susceptibility imaging,” *J Magn Reson Imaging*, vol. 1, pp. 521–530, Oct. 1991. PMID: 1790376.
- [120] Y. Gandon, D. Guyader, J. F. Heautot, M. I. Reda, J. Yaouanq, T. Buhé, P. Brissot, M. Carsin, and Y. Deugnier, “Hemochromatosis: diagnosis and quantification of liver iron with gradient-echo MR imaging,” *Radiology*, vol. 193, pp. 533–538, Nov. 1994. PMID: 7972774.
- [121] S. B. Reeder, A. R. Pineda, Z. Wen, A. Shimakawa, H. Yu, J. H. Brittain, G. E. Gold, C. H. Beaulieu, and N. J. Pelc, “Iterative decomposition of water and fat with echo asymmetry and least-squares estimation (IDEAL): application with fast spin-echo imaging,” *Magn Reson Med*, vol. 54, pp. 636–644, Sept. 2005. PMID: 16092103.
- [122] A. C. A. Westphalen, A. Qayyum, B. M. Yeh, R. B. Merriman, J. A. Lee, A. Lamba, Y. Lu, and F. V. Coakley, “Liver fat: effect of hepatic iron deposition on evaluation with opposed-phase MR imaging,” *Radiology*, vol. 242, pp. 450–455, Feb. 2007. PMID: 17255416.

- [123] M. R. Bashir, E. M. Merkle, A. D. Smith, and D. T. Boll, "Hepatic MR imaging for in vivo differentiation of steatosis, iron deposition and combined storage disorder: single-ratio in/opposed phase analysis vs. dual-ratio dixon discrimination," *Eur J Radiol*, vol. 81, pp. e101–109, Feb. 2012. PMID: 21330083.
- [124] J. Mao, H. Yan, W. W. Brey, J. Bidgood, W D, J. J. Steinbach, and A. Mancuso, "Fat tissue and fat suppression," *Magn Reson Imaging*, vol. 11, no. 3, pp. 385–393, 1993. PMID: 8505872.
- [125] S. McPherson, J. R. Jonsson, G. J. Cowin, P. O'Rourke, A. D. Clouston, A. Volp, L. Horsfall, D. Jothimani, J. Fawcett, G. J. Galloway, M. Benson, and E. E. Powell, "Magnetic resonance imaging and spectroscopy accurately estimate the severity of steatosis provided the stage of fibrosis is considered," *Journal of Hepatology*, vol. 51, pp. 389–397, Aug. 2009.
- [126] R. J. H. Borra, S. Salo, K. Dean, R. Lautamäki, P. Nuutila, M. Komu, and R. Parkkola, "Nonalcoholic fatty liver disease: Rapid evaluation of liver fat content with in-phase and out-of-phase MR imaging1," *Radiology*, vol. 250, pp. 130–136, Jan. 2009. PMID: 19017926.
- [127] D. P. O'Regan, M. F. Callaghan, M. Wylezinska-Arridge, J. Fitzpatrick, R. P. Naoumova, J. V. Hajnal, and S. A. Schmitz, "Liver fat content and t2*: simultaneous measurement by using breath-hold multiecho MR imaging at 3.0 t-feasibility," *Radiology*, vol. 247, pp. 550–557, May 2008. PMID: 18349314.
- [128] H. Yu, C. A. McKenzie, A. Shimakawa, A. T. Vu, A. C. S. Brau, P. J. Beatty, A. R. Pineda, J. H. Brittain, and S. B. Reeder, "Multiecho reconstruction for simultaneous water-fat decomposition and t2* estimation," *J Magn Reson Imaging*, vol. 26, pp. 1153–1161, Oct. 2007. PMID: 17896369.
- [129] S. B. Reeder, C. A. McKenzie, A. R. Pineda, H. Yu, A. Shimakawa, A. C. Brau, B. A. Hargreaves, G. E. Gold, and J. H. Brittain, "Water-fat separation with IDEAL gradient-echo imaging," *J. Magn. Reson. Imaging*, vol. 25, no. 3, p. 644–652, 2007.
- [130] H. Yu, A. Shimakawa, C. A. McKenzie, E. Brodsky, J. H. Brittain, and S. B. Reeder, "Multiecho water-fat separation and simultaneous r2* estimation with multifrequency fat spectrum modeling," *Magn Reson Med*, vol. 60, pp. 1122–1134, Nov. 2008. PMID: 18956464.
- [131] V. V. Chebrolu, C. D. G. Hines, H. Yu, A. R. Pineda, A. Shimakawa, C. A. McKenzie, A. Samsonov, J. H. Brittain, and S. B. Reeder, "Independent estimation of t*2 for water and fat for improved accuracy of fat quantification," *Magn Reson Med*, vol. 63, pp. 849–857, Apr. 2010. PMID: 20373385.

Part I

Variable Echo Time SPGR

Chapter 2

High-resolution Fourier-encoded sub-millisecond echo time musculoskeletal imaging at 3 Tesla and 7 Tesla

An adapted version of this chapter is published as: **Deligianni X**, Bär P, Scheffler K, Trattnig S and Bieri O (2012), High-resolution Fourier-encoded sub-millisecond echo time musculoskeletal imaging at 3 Tesla and 7 Tesla. *Magn Reson Med.* doi: 10.1002/mrm.24578

2.1 Introduction

Highly oriented tissue components, such as the menisci, tendons or ligaments, exhibit very short transverse relaxation times (T_2) and typically appear black in contemporary musculoskeletal (MSK) imaging, which might lead to misinterpretations [1–3]. As a result, ultra short echo time (UTE) imaging techniques typically offering a time to echo (TE) close to zero [4, 5] were proposed and a broad number of qualitative and quantitative UTE MSK applications (including X-nuclei imaging [6]) can be traced in literature [3]. One drawback of UTE sequences, however, is the radial acquisition scheme which not only requires an extended sampling time [7–9] but is also more prone to artifacts due to the gradient system imperfections [10], as compared to Fourier-encoded, i.e. Cartesian sampling techniques. Moreover, the subject frequently needs to be positioned in the isocenter to circumvent issues from B_0 field shimming [11]. Thus, even 20 years after their introduction [4], UTE methods are still hardly used in clinical routine.

Clearly, from a simple research perspective, the development of any zero TE technique is a challenge of its own. For the visualization of most short-lived T_2 tissues, however, this seems not of foremost importance, since the typical T_2 values reported in the literature for fibrous tissues range from several hundreds of microseconds (tendons: $T_2 = 0.4 - 7.0$ ms) to several milliseconds (menisci: $T_2 = 5 - 8$ ms) [5, 12, 13]. Moreover, for a reliable early diagnosis of lesions in the ultrastructural morphological composition of fibrous tissues, it is absolutely essential to provide high-resolution images. Consequently, at least from a clinical perspective, there is a high demand for a robust and easily applicable method to image connective MSK structures with high-resolution and signal-to-noise.

A straightforward approach is thus to adapt a 3D Cartesian spoiled gradient echo (SPGR) for sub-millisecond (sub-ms) TE, since these sequences generally are broadly used for MSK imaging in the clinical routine [14, 15]. Several methods can be used to shorten the TE with Cartesian sampling techniques, such as asymmetric RF pulses, asymmetric readout (also referred to as partial echoes), optimal gradient switching patterns (maximum gradient amplitudes and slew rates), ramp sampling, or to dynamically adapt and reduce the TE towards the center of k-space [16, 17], commonly referred to as variable echo time (vTE). This concept can already be found in the early times of MRI for Fourier zeugmatography [18], where phase encoding was performed by varying the duration of the phase encoding gradient [19], rather than its amplitude as with contemporary MRI sequences. Exactly this principle, in combination with the fact that the lower spatial frequencies of k-space define the signal contrast [20], is exploited by vTE techniques: the TE is minimized for every line in k-space. As a result, in complete analogy to UTE imaging, the TE in the center of k-space (requiring small or even zero gradient moments for phase and slice encoding), can be considerably shortened as compared to the outer parts. Variable echo times have been used for time of flight angiography [19], signal-to-noise ratio (SNR) enhancement in combination with contrast agents [21], or for imaging of bone [22]. In contrast to UTE imaging, however, Cartesian vTE methods are fast and flexible, and provide a simple setup for integra-

tion of additional preparation schemes, such as long T_2 suppression or fat suppression schemes [1, 23, 24]. Generally, vTE techniques allow a further TE reduction by using an asymmetric readout; typically achieving a minimal TE around 2.8 ms for 0.5 mm in-plane resolution for a 3D Cartesian scan [16, 17, 19, 20]. No dedicated reconstruction methods, however, have been used so far to optimize image reconstruction from vTE methods using partial sampling of the echo.

In this chapter, we will demonstrate that standard Fourier-encoded SPGR sequences can be adapted to yield sub-ms TE using an asymmetric readout in combination with a vTE technique along the phase and slice encoding directions (sub-ms SPGR). In addition, a projection onto convex sets (POCS) technique was used to yield improved image reconstruction from partial echo data [25]. Overall, this setup allows the acquisition of high-resolution images of short-lived T_2 species, such as tendons, ligaments or menisci, with high SNR and within clinically acceptable scan times. The proposed sub-ms SPGR imaging technique was explored for the visualization of connective tissue in the knee at 3T and at 7T, and for the Achilles tendon at 7T. Although research seems to move towards more and more complex trajectories to achieve zero TE, our results demonstrate that especially MSK imaging of fibrous tissues can profit significantly from the robustness of a standard Cartesian method.

2.2 Methods

2.2.1 Experiments

All measurements were performed either at 3T (Magnetom Verio, Siemens Medical Solutions, Erlangen, Germany) or 7T (Magnetom 7T, Siemens Medical Solutions, Erlangen, Germany). The experiments were approved by the local ethics committee and written consent was obtained from the volunteers prior to scanning in case they were not belonging to the project. A custom 3D multi-echo Cartesian SPGR technique was adapted to use a variable echo time in combination with an asymmetric readout only for the first echo (TE_1). Moreover, non-selective excitation pulses were used and gradient slew rate and switching patterns were optimized in order to maximize speed within the peripheral nerve stimulation limits. As a result, TE_1 has its maximum near the edges of k-space but becomes shorter towards the center of k-space (see Fig. 2.1). The minimum value of TE_1 depends (for constant readout bandwidths) mainly on the properties of the readout gradient and thus on the performance of the gradient system (i.e. slew rate and maximum amplitude) and raises with increasing resolution. For instance, for a reduction in echo time of about 37 % the TE was equal to TE_{\min} for 44 % of the phase encoding steps at 3T. Nevertheless, even for in-plane resolutions down to about 0.4 x 0.4 mm² a sub-millisecond TE_1 could be achieved. Optionally to the sub-millisecond (TE_1) image, a fully sampled second echo (TE_2) image could be acquired, for which the time to echo (TE_2) was kept constant across the k-space. This allows calculation of a difference image, as commonly used with UTE sequences to suppress signal from long T_2 species.

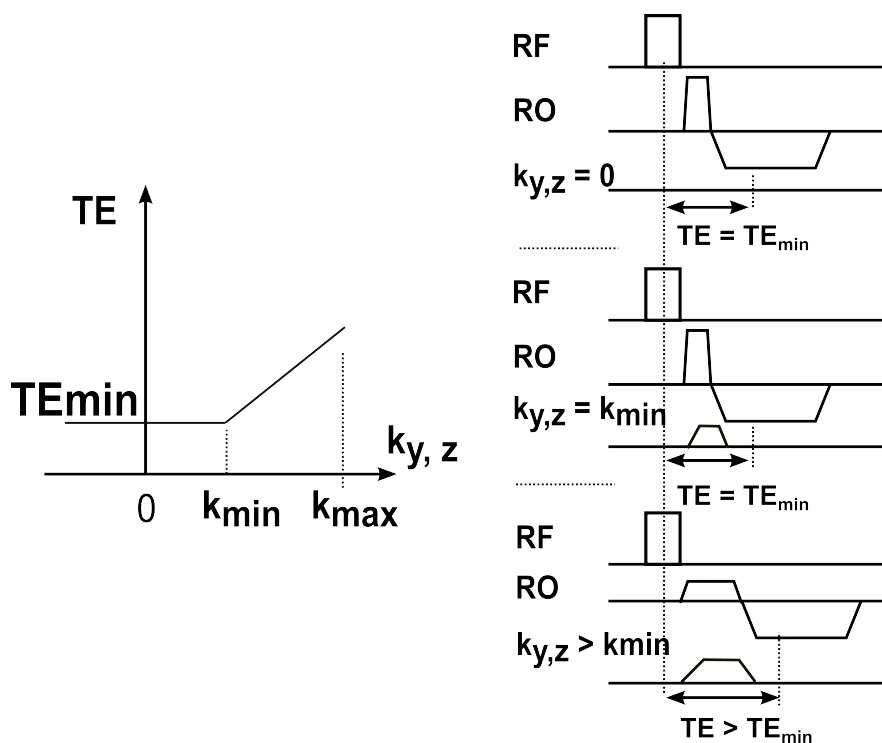


Figure 2.1: For pulse sequences using vTE, the TE is a function of the variable prephasing gradient moments along the direction of the phase (k_y) and slice (k_z) encoding. The minimum TE (TE_{min}) is reached at the center of k-space and is limited by constant factors: the time required for excitation, such as the radiofrequency pulse duration, and the properties of frequency encoding along the direction of the RO, such as the echo asymmetry. As long as the variable $k_{y,z}$ prephasing gradient moments require less time than the constant events, TE_{min} can be maintained (as indicated in the plot by k_{min}) but starts to increase continuously with increasing $k_{y,z}$ moments ($k_{y,z} > k_{min}$).

Asymmetric readout data was reconstructed using a POCS algorithm [25]. The minimum asymmetry allowed by the algorithm was 8 % (a value of 100 % indicates full sampling before the k-space center). Online calculation of the image difference was performed (i.e. subtraction of the TE_2 image from the TE_1 image) in case of dual contrast acquisitions using a scripting framework [26].

At 3T, whole knee scans of 8 healthy subjects were performed using a dedicated transmit/ receive 15-channel knee coil with 15 integrated preamplifiers and elements arranged in 3 rings by 5 elements. At 7T, imaging of the knee of one healthy volunteer and of the Achilles tendon of two healthy volunteers was performed with a dedicated 28-channel knee coil (QED, USA). For all protocol details, see Table 2.1. Flip angles were derived from the Ernst equation based on a T_1 estimate for cartilage and fibrous tissue in the range of about 1000 ms [27].

	Knee	joint	Achilles	tendon
	3T	7T		
In-plane resolution (mm)	0.55	0.36	0.52	0.42
FOV (mm)	140	140	199	159
Slices / Slice thickness (mm)	52 / 2.5	120 / 1.0	72 / 1.0	128 / 0.5
BW (Hz / Pixel)	528	345	590	352
TE₁ (ms) / RO asymmetry (%)^a	0.8 / 14.8	0.92 / 13.3	0.8 / 15.6	1.02 / 15.6
Reduction in TE_{1-max}(ms)^b	37.5	43.6	22.3	32.9
TE₂ (ms) / RO asymmetry (%)^a	8.22 / 100	8.08 / 100	- / -	- / -
TR (ms) / Flip angle	12 / 9 ^o	13 / 8 ^o	7 / 8 ^o	7 / 8 ^o
Hard pulse duration (ms)	0.15	0.15	0.15	0.15
Acquisition time (min)	2.40	7.51	5.47	6.22
Number of averages	1	1	2	1

^a RO (Readout asymmetry: a percentage of 100% indicates full sampling before the k-space center. Readout was always performed along the longest (i.e. head-foot) axis.

^bReduction in TE_{1-max}: reduction in the first echo time achieved using the vTE scheme

Table 2.1: MR Scan Parameters

2.3 Results

2.3.1 Imaging of connective tissue at 3T

Imaging of the lateral knee menisci is demonstrated in Fig. 2.2. The first echo image (see Fig. 2.2a), acquired with TE₁ = 0.8 ms, shows no or low contrast between the frontal and the posterior part of the lateral meniscus and its surrounding tissue as expected from a purely proton density weighted image. This is in contrast to the second echo image, acquired with a TE₂ = 8.22 ms (see Fig. 2.2a), where the signal from the lateral meniscus is considerably reduced due to the short T₂ of connective tissues. As a result, parts of the connective tissue appear with a pronounced positive contrast in the difference image (see Fig. 2.2a) and the lateral meniscus can be clearly delineated from its surrounding tissue with high signal- and contrast-to-noise. This signal behavior was consistent among all 8 volunteers. The visibility of the lateral meniscus on both tibial and femoral cartilage images corroborates that the apparent positive contrast in the difference image is not simply due to a water-fat shift. Interestingly, positive contrast variation is also observed within cartilage layers, indicating zonal regions of short T₂ near the cortical bone, as can be expected.

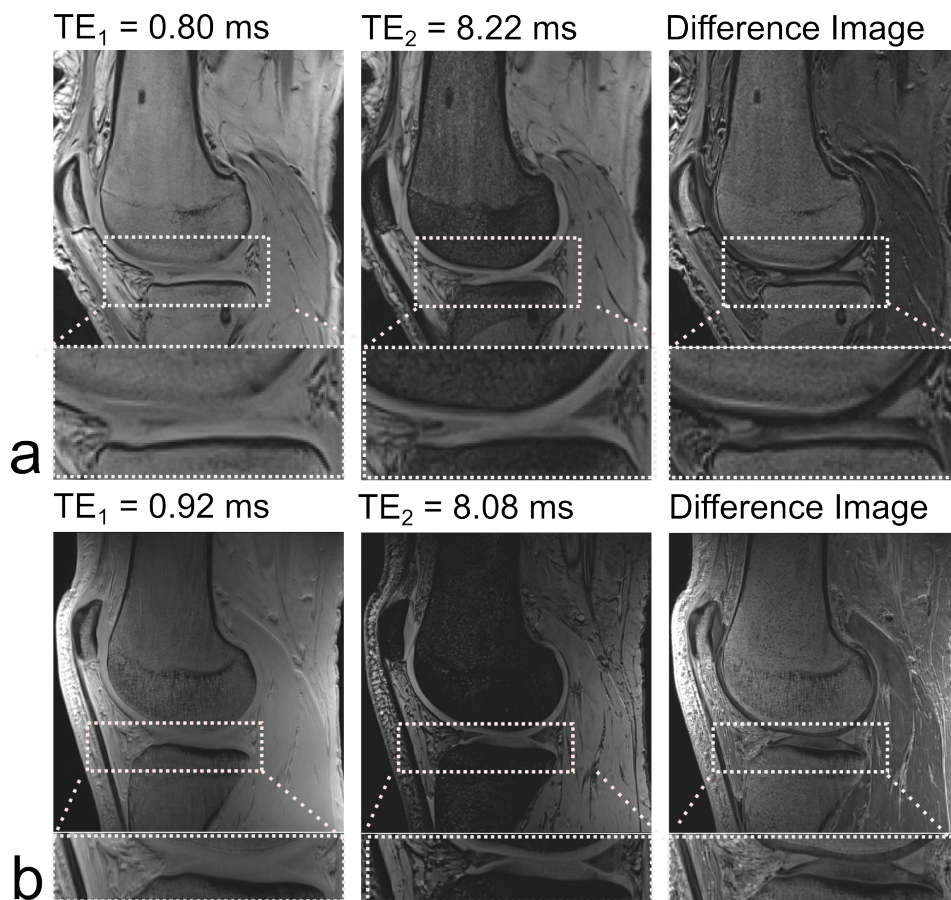


Figure 2.2: Sagittal sample images of the lateral menisci in the knee joint. (a) Optimized 3D SPGR scan at 3T with $0.50 \times 0.50 \text{ mm}^2$ in-plane resolution and 2.5 mm slice thickness, (b) Optimized 3D SPGR scan at 7T with $0.36 \times 0.36 \text{ mm}^2$ in-plane resolution and 1 mm slice thickness.

Similar results are observed for patellar and cruciate ligaments. The patellar ligament and its bundle structure is clearly visible on the short echo image (see Fig. 2.2a) but has completely disappeared on the second echo image (see Fig. 2.2a). It thus reveals with positive contrast on the difference image (see Fig. 2.2a). The posterior cruciate ligament was also clearly visible on both, 3T (see Figs. 2.3a-b) and 7T (see Fig. 2.3c) images. Even thin structures of the ligament reveal without any blurring artifact on the sub-millisecond echo images and on the difference image (see Figs. 2.3a-c).

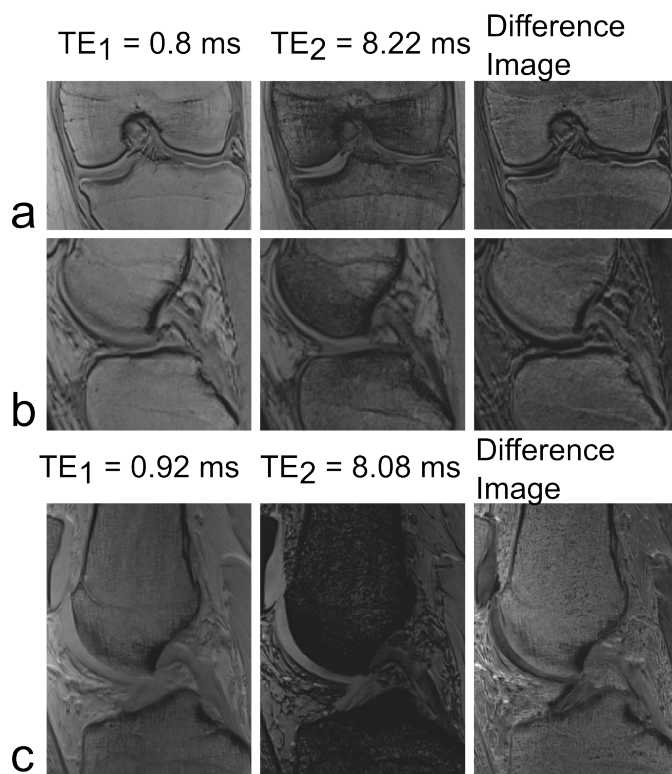


Figure 2.3: Coronal and sagittal sample images of knee joint ligaments. (a, b) Optimized 3D SPGR scan at 3T with in-plane resolution $0.5 \times 0.5 \text{ mm}^2$, slice thickness 2.5 mm, (c) Optimized 3D SPGR scan at 7T with in-plane resolution $0.36 \times 0.36 \text{ mm}^2$, slice thickness 1 mm.

2.3.2 Imaging of the knee joint and the Achilles tendon at 7T

High in-plane resolution images ($0.36 \times 0.36 \text{ mm}^2$) of the knee joint show high contrast between the meniscus and the cartilage for scans with a sub-millisecond echo time of $TE_1 = 0.92 \text{ ms}$ (see Fig. 2.2b). In addition, connective tissues, such as the posterior cruciate ligament, can be very clearly visualized (Fig. 2.3c).

The images of the Achilles tendon indicate that minimizing the echo time to 0.8 ms, with a resolution of 0.52 mm and a slice thickness of 1 mm yields high signal from the tendon (see Fig. 2.4a). In Fig. 2.4a the tendon appears with high signal and with very homogenous signal distribution. However, lowering the demands for the echo time and increasing the resolution to 0.42 mm in-plane (see Fig. 2.4b) enables the observation of structures such as thin bundles of the Achilles tendon.

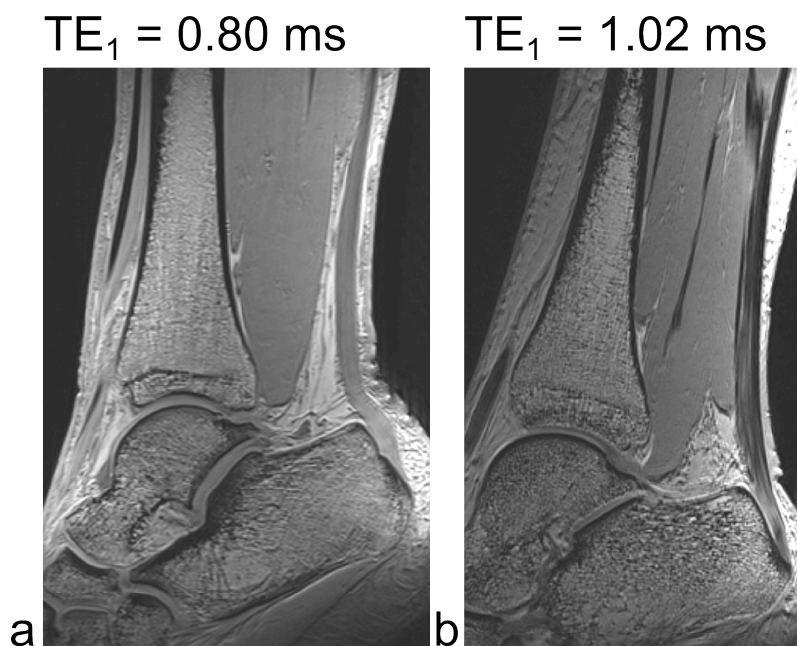


Figure 2.4: Sagittal sample images of the Achilles tendon at 7T. (a) $TE_1 = 0.8$ ms, resolution of $0.52 \times 0.52 \times 1.0$ mm³, 2 averages, (b) Optimized 3D SPGR scan with $TE_1 = 1.02$ ms for a resolution of $0.42 \times 0.42 \times 0.5$ mm³, 1 average.

2.4 Discussion

High-resolution and high contrast-to-noise 3D imaging of short-lived T_2 MSK tissue components was demonstrated to be feasible using an optimized Fourier-encoded SPGR technique. Typically, for the commonly required in-plane resolution of about $0.3 \times 0.3 - 0.5 \times 0.5$ mm² for high-resolution MSK imaging, a minimum TE of about 1.0 - 0.8 ms could be achieved which has shown to be sufficient for imaging the fibrous tissues of interest (i.e., menisci, tendons and ligaments). Imaging of very short-lived T_2 species, such as cortical bone with a $T_2 \ll 1$ ms [23], however, will not be feasible.

Compared with contemporary radial 3D UTE sequences and other non-Cartesian sampling techniques, Fourier-encoded methods benefit from their intrinsic robustness and allow high-resolution imaging within clinically feasible scan times down to about 2 to 3 min. Moreover, scans are not restricted to the isocenter or do not require an isotropic voxel size, and generally allow the use of common acceleration methods such as partial Fourier or parallel imaging techniques without any restriction. As a result, sub-ms SPGR can be easily implemented in protocols for clinical MSK imaging for positive contrast visualization of fibrous tissue components.

Generally, imaging methods able to provide sub-ms TE, such as UTE, have shown great potential for MSK imaging, and have recently become a major research focus in this field not only at 1.5 and 3 T [5, 24, 28] but also at ultra-high field strength [29, 30].

Besides advanced morphological evaluations, biochemical MSK imaging concepts such as sodium imaging or T_2^* imaging, have gained increased interest for ultrastructural and functional assessment of cartilage, tendons and ligaments, especially at 7T [12,13,31–34]. Both sodium and T_2^* imaging, however, would benefit from acquisition strategies providing short TEs. About 60 % of the total sodium in cartilage decays with a short-lived T_2 component of about 1 ms, leading to a significant loss of signal using conventional MR imaging techniques [35]. Contemporary sodium imaging protocols are thus commonly based on non-Cartesian acquisition schemes [6,31,36]. Signal-to-noise, however, is still the major limiting factor requiring long scan times even for low resolution images. As a result, the use of highly efficient 3D sampling schemes, such as Fourier encoding rather than radial sampling, could contribute to a substantial increase in signal-to-noise ratio, if sub-ms TEs can be achieved. Similarly, quantitative T_2^* imaging with a multiecho UTE approach has only recently shown good promise as a marker for Achilles tendinopathy [33]. Quantitative imaging techniques in particular, however, require a highly robust imaging technique for the derivation of reliable results; but UTE and non-Cartesian sampling methods are highly prone to artifacts from their technical challenge, and thus less stable than their Cartesian counterparts. In summary, Fourier-encoded SPGR with sub-ms TE not only is an easy applicable alternative to morphological MSK UTE imaging in the clinical routine but is also of good potential interest for biochemical quantification techniques such as sodium imaging and T_2^* mapping, especially at ultra-high field strengths.

In conclusion, high-resolution positive contrast imaging of fibrous tissue components in the knee and ankle joint was demonstrated to be feasible within clinically adequate scan times using a conventional, but optimized, Cartesian sampling strategy. Sub-ms TEs for common Fourier-encoded SPGR sequences can be optioned on clinical whole body system using vTEs in combination with high asymmetric echo RO and a dedicated algorithm for reconstruction of undersampled data. This results in a highly robust, flexible and efficient method for imaging of short-lived T_2 components in the range of several hundred microseconds from clinical to ultra-high field strength.

References

- [1] P. D. Gatehouse and G. M. Bydder, “Magnetic resonance imaging of short t2 components in tissue,” *Clin Radiology*, vol. 58, pp. 1–19, Jan. 2003. PMID: 12565203.
- [2] P. D. Gatehouse, R. W. Thomas, M. D. Robson, G. Hamilton, A. H. Herlihy, and G. M. Bydder, “Magnetic resonance imaging of the knee with ultrashort TE pulse sequences,” *Magn Reson Imaging*, vol. 22, pp. 1061–1067, Oct. 2004. PMID: 15527992.
- [3] W. C. Bae, J. Du, G. M. Bydder, and C. B. Chung, “Conventional and ultrashort time-to-echo magnetic resonance imaging of articular cartilage, meniscus, and intervertebral disk,” *Top Magn Reson Imaging*, vol. 21, pp. 275–289, Oct. 2010. PMID: 22129641.
- [4] C. J. Bergin, J. M. Pauly, and A. Macovski, “Lung parenchyma: projection reconstruction MR imaging,” *Radiology*, vol. 179, pp. 777–781, June 1991. PMID: 2027991.
- [5] M. D. Robson, P. D. Gatehouse, M. Bydder, and G. M. Bydder, “Magnetic resonance: an introduction to ultrashort TE (UTE) imaging,” *J Comput Assist Tomogr*, vol. 27, pp. 825–846, Dec. 2003. PMID: 14600447.
- [6] S. Nilles-Vallespin, M.-A. Weber, M. Bock, A. Bongers, P. Speier, S. E. Combs, J. Wöhrle, F. Lehmann-Horn, M. Essig, and L. R. Schad, “3D radial projection technique with ultrashort echo times for sodium MRI: clinical applications in human brain and skeletal muscle,” *Magn Reson Med*, vol. 57, pp. 74–81, Jan. 2007. PMID: 17191248.
- [7] E. M. Haacke, R. W. Brown, M. R. Thompson, and R. Venkatesan, *Magnetic Resonance Imaging: Physical Principles and Sequence Design*. 1999. John Wiley & Sons, New York.
- [8] M. A. Bernstein, K. F. King, and X. J. Zhou, *Handbook of MRI Pulse Sequences*. Elsevier, Sept. 2004.
- [9] M. L. Lauzon and B. K. Rutt, “Effects of polar sampling in k-space,” *Magn Reson Med*, vol. 36, no. 6, p. 940–949, 1996.
- [10] I. C. Atkinson, A. Lu, and K. R. Thulborn, “Characterization and correction of system delays and eddy currents for MR imaging with ultrashort echo-time and time-varying gradients,” *Magn Reson Med*, vol. 62, no. 2, p. 532–537, 2009.
- [11] Y. Qian, A. A. Williams, C. R. Chu, and F. E. Boada, “High-resolution ultrashort echo time (UTE) imaging on human knee with AWSOS sequence at 3.0 t,” *J Magn Reson Imaging*, vol. 35, pp. 204–210, Jan. 2012. PMID: 22002811.
- [12] V. Juras, V. Jellus, I. Szomolanyi, I. Frolo, and S. Trattinig, “1H relaxation properties of achilles tendons measured by 3D-UTE at 3T and 7T: a feasibility study,” in *Proceedings 19th Scientific Meeting, International Society for Magnetic Resonance in Medicine*, (Montreal), p. 3212.
- [13] A. Williams, Y. Qian, S. Golla, and C. R. Chu, “UTE-T2* mapping detects sub-clinical meniscus injury after anterior cruciate ligament tear,” *Osteoarthritis and Cartilage*, vol. 20, pp. 486–494, June 2012. PMID: 22306000.
- [14] R. Krug, C. Stehling, D. A. C. Kelley, S. Majumdar, and T. M. Link, “Imaging of the musculoskeletal system in vivo using ultra-high field magnetic resonance at 7 t,” *Investig Radiol*, vol. 44, pp. 613–618, Sept. 2009.

- [15] G. H. Welsch, V. Juras, P. Szomolanyi, T. C. Mamisch, P. Baer, C. Kronnerwetter, M. Blanke, H. Fujita, and S. Trattig, “Magnetic resonance imaging of the knee at 3 and 7 tesla: a comparison using dedicated multi-channel coils and optimised 2D and 3D protocols,” *Eur Radiol*, Apr. 2012. PMID: 22538628.
- [16] P. Schmalbrock, “A method to achieve very short echo times for submillimeter resolution imaging,” in *Proceedings 11th Scientific Meeting, International Society for Magnetic Resonance in Medicine*, (New York, USA), p. 3934, 1992.
- [17] K. Ying, P. Schmalbrock, and B. Clymer, “Echo-time reduction for submillimeter resolution imaging with a 3D phase encode time reduced acquisition method,” *Magn Reson Med*, vol. 33, pp. 82–87, Jan. 1995. PMID: 7891540.
- [18] Kumar, D. Welti, and R. Ernst, “NMR fourier zeugmatography,” *J Magn Reson*, vol. 18, no. 1, pp. 69–83, 1975.
- [19] E.-K. Jeong, D. L. Parker, J. S. Tsuruda, and J.-Y. Won, “Reduction of flow-related signal loss in flow-compensated 3D TOF MR angiography, using variable echo time (3D TOF-VTE),” *Magn Reson Med*, vol. 48, pp. 667–676, Oct. 2002. PMID: 12353284.
- [20] H. K. Song and F. W. Wehrli, “Variable TE gradient and spin echo sequences for in vivo MR microscopy of short t2 species,” *Magn Reson Med*, vol. 39, pp. 251–258, Feb. 1998. PMID: 9469708.
- [21] A. F. Stalder, D. V. Elverfeldt, D. Paul, J. Hennig, and M. Markl, “Variable echo time imaging: signal characteristics of 1-m gadobutrol contrast agent at 1.5 and 3T,” *Magn Reson Med*, vol. 59, pp. 113–123, Jan. 2008. PMID: 18058940.
- [22] J. Magland and F. W. Wehrli, “Imaging of trabecular bone architecture at isotropic resolution by a new variable-echo hybrid radial acquisition technique,” in *Proceedings 13th Scientific Meeting, International Society for Magnetic Resonance in Medicine*, (Miami, Florida, USA), p. 2365, 2005.
- [23] A. Techawiboonwong, H. K. Song, and F. W. Wehrli, “In vivo MRI of submillisecond t(2) species with two-dimensional and three-dimensional radial sequences and applications to the measurement of cortical bone water,” *NMR Biomed*, vol. 21, pp. 59–70, Jan. 2008. PMID: 17506113.
- [24] J. Du, A. M. Takahashi, W. C. Bae, C. B. Chung, and G. M. Bydder, “Dual inversion recovery, ultrashort echo time (DIR UTE) imaging: creating high contrast for short-t(2) species,” *Magn Reson Med*, vol. 63, pp. 447–455, Feb. 2010. PMID: 20099332.
- [25] G. McGibney, M. R. Smith, S. T. Nichols, and A. Crawley, “Quantitative evaluation of several partial fourier reconstruction algorithms used in MRI,” *Magn Reson Med*, vol. 30, pp. 51–59, July 1993. PMID: 8371675.
- [26] F. Santini, S. Patil, and K. Scheffler, “IceLuva: a scripting framework for MR image reconstruction based on free software,” *Concepts Magn Reson B Magn Reson Eng*, vol. 39B, pp. 1–10, Feb. 2011.
- [27] G. J. Stanisz, E. E. Odobina, J. Pun, M. Escaravage, S. J. Graham, M. J. Bronskill, and R. M. Henkelman, “T1, t2 relaxation and magnetization transfer in tissue at 3T,” *Magn Reson Med*, vol. 54, no. 3, p. 507–512, 2005.
- [28] J. Rahmer, P. Börnert, and S. P. M. Dries, “Assessment of anterior cruciate ligament reconstruction using 3D ultrashort echo-time MR imaging,” *J Magn Reson Imaging*, vol. 29, pp. 443–448, Feb. 2009. PMID: 19161200.

- [29] R. R. Regatte and M. E. Schweitzer, "Ultra-high-field MRI of the musculoskeletal system at 7.0T," *J Magn Reson Imaging*, vol. 25, pp. 262–269, Feb. 2007. PMID: 17260399.
- [30] R. Krug, P. E. Z. Larson, C. Wang, A. J. Burghardt, D. A. C. Kelley, T. M. Link, X. Zhang, D. B. Vigneron, and S. Majumdar, "Ultrashort echo time MRI of cortical bone at 7 tesla field strength: A feasibility study," *J Magn Reson Imaging*, vol. 34, pp. 691–695, Sept. 2011. PMID: 21769960.
- [31] S. Trattnig, S. Zbýň, B. Schmitt, K. Friedrich, V. Juras, P. Szomolanyi, and W. Bogner, "Advanced MR methods at ultra-high field (7 tesla) for clinical musculoskeletal applications," *Eur Radiol*, June 2012. PMID: 22688127.
- [32] J. Hennig and O. Speck, eds., *High-Field MR Imaging*. Springer, 2011 ed., Nov. 2011.
- [33] V. Juras, S. Zbyn, C. Pressl, L. Valkovic, P. Szomolanyi, I. Frollo, and S. Trattnig, "Regional variations of t_2^* in healthy and pathologic achilles tendon in vivo at 7 tesla: Preliminary results," *Magn Reson Med*, 2011.
- [34] G. H. Filho, J. Du, B. C. Pak, S. Statum, R. Znamorowski, P. Haghighi, G. Bydder, and C. B. Chung, "Quantitative characterization of the achilles tendon in cadaveric specimens: T1 and t_2^* measurements using ultrashort-TE MRI at 3 t," *AJR Am J Roentgenol*, vol. 192, pp. W117–124, Mar. 2009. PMID: 19234239.
- [35] A. Borthakur, E. Mellon, S. Niyogi, W. Witschey, J. B. Kneeland, and R. Reddy, "Sodium and $t_1\rho$ MRI for molecular and diagnostic imaging of articular cartilage," *NMR Biomed*, vol. 19, no. 7, p. 781–821, 2006.
- [36] L. Wang, Y. Wu, G. Chang, N. Oesingmann, M. E. Schweitzer, A. Jerschow, and R. R. Regatte, "Rapid isotropic 3D-sodium MRI of the knee joint in vivo at 7T," *J Magn Reson Imaging*, vol. 30, pp. 606–614, Sept. 2009. PMID: 19711406.

Chapter 3

Water-selective excitation of short T_2 species with binomial pulses

An adapted version of this chapter is submitted as: X. Deligianni, P. Bär, K. Scheffler, S.Trattnig and O. Bieri, Water-selective excitation of short T_2 species with binomial pulses, as a possible publication to MRM.

3.1 Introduction

Highly ordered musculoskeletal (MSK) structures, such as menisci, tendons, ligaments or bone, exhibit short transverse relaxation (T_2) times (in the range of only few milliseconds and below), typically requiring dedicated imaging sequences for their visualization [1–3]. An important general issue with MSK imaging, however, is the possible interference of fat with the tissue of interest. Several studies have demonstrated that fat suppression, or alternatively, spectrally selective excitation of water, can significantly improve the quality of MSK images to provide diagnostic information equivalent to that acquired with invasive arthroscopy [2,4,5]. In complete analogy, visualization of short-lived T_2 components can be considerably improved by either long T_2 suppression or fat suppression techniques [2,6,7]. Moreover, fat suppression allows for MSK imaging with high signal-to-noise, since there is no need for high receiver bandwidths to account for possible chemical shift artifacts [5,8] and increases the sensitivity to contrast uptake in contrast-enhanced MSK studies.

The most common approach for fat suppression in clinical practice is the use of spectrally selective radiofrequency (RF) and gradient prepulses for fat saturation (usually referred to as FATSAT) [9–11]. A general disadvantage of this approach is not only the additional time required for magnetization preparation, but also its susceptibility to heterogeneities in the main magnetic field (B_0), as well as in the transmit field (B_1) [12]. Moreover, some authors pointed out that fat saturation pulses might reduce the conspicuity of short T_2 structures [2]. In contrast, the use of water-selective excitation with composite pulses is known to offer improved contrast through fat suppression between the cartilage and the synovial fluid without considerably increasing the scan time [4,13,14]. A comparison of the two methods based on spin echo sequences showed that the water excitation performed statistically better than FATSAT for all investigated criteria, including fat suppression homogeneity, presence of artifacts, conspicuousness of lesions, and overall image quality [15]. As a result, water-selective excitation pulses are extensively used for cartilage imaging in the clinical routine [16–19]. Water-selective excitation consists of composite RF pulses whose relative flip angles are most commonly modulated according to the coefficients of a binomial series [13,20,21]. The phase accumulation of the off-resonant spins between the sub-pulses can be used to excite either only water (water excitation) or only fat components (off-resonant excitation). Binomial water excitation has recently attracted considerable interest [22–26] especially phase modulated schemes [25,27–29].

In this chapter, we investigate the possible benefit of short 1-1 binomial schemes for spectrally selective excitation of short-lived T_2 components. Nonselective sub-pulses, rather than spatial-spectral pulses [20], were used to allow sub-millisecond echo times in combination with a recently reported three-dimensional (3D) variable echo time (vTE) spoiled gradient echo (SPGR) sequence [30]. Simulations indicate a maximum signal loss from binomial excitation of about 30% in the limit of very short T_2 (0.1 ms), as compared to nonselective imaging; leveling off faster with increasing field strength to about 19% at 3T and 10% at 7T for a T_2 of 1 ms. In agreement with simulations, phase of about 90° yielded minimum signal loss: for menisci the signal loss was about 5% and 0-1% at 3T and 7T, whereas for the ligaments 9% and 13%. Finally, measurements at 3T revealed considerable lower signal loss at 3T in comparison to FATSAT.

3.2 Methods

Only minimal binomial preparation schemes, i.e., 1-1 excitation, with different fat phase evolution ϕ between the two hard sub-pulses were considered; for simplicity denoted by $1_\phi 1$ (see Fig. 3.1). The spacing of the sub-pulses, i.e. the time τ_ϕ (in ms) required for spectral excitation,

thus becomes a function of the desired fat phase evolution ϕ (in degrees) and the field strength B_0 (in Tesla), according to

$$\tau_\phi = \frac{2\pi \cdot \phi \cdot 10^3}{360 \cdot \sigma \cdot \gamma \cdot B_0} \quad (3.1)$$

where σ is the fat-water chemical shift (in ppm), and γ is the gyromagnetic ratio (in rad / s / T).

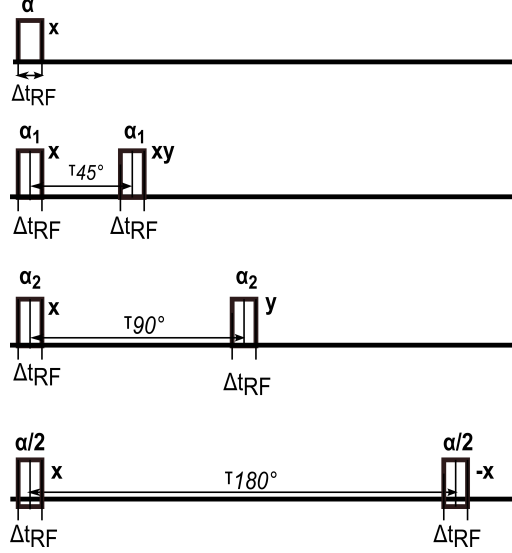


Figure 3.1: Pulse sequence diagram of the different excitation schemes. The sub-pulse flip angles α_1, α_2 for 1_{45° and 1_{90° are higher than $\alpha/2$ so that the equivalent flip angle of the two sub-pulses equals a pulse with flip angle α . The axis of rotation is indicated on the right side of each pulse.

3.2.1 Simulations

All simulations were performed with Matlab 7.0 (The Mathworks, Inc., MA, USA, R2008b). The steady state magnetization was simulated based on the piece-wise constant integrated Bloch equation [31]. As usual, perfect spoiling conditions were assumed, and motion or diffusion effects were neglected. Within the context of short T_2 species excitation, however, finite radio-frequency (RF) pulse effects were accounted for. To this end, excitation pulses were simulated as an equidistant series of 50 pulses of 10 μ s duration, interleaved by longitudinal and transverse relaxation processes. An indicative longitudinal relaxation (T_1) of 500 ms for fibrous tissues, and a repetition time (TR) of 6 ms was assumed. The relative loss of signal from binomial excitation (Δ_s) was estimated over a range of nominal flip angles $\alpha = 0 - 90^\circ$, as a function of the field strength B_0 (3T and 7T), the spacing between the sub-pulses τ_ϕ (for $\phi = 15^\circ - 180^\circ$), as well as $T_2 = 0.1 - 10$ ms, according to

$$\Delta_s(T_2, B_0) = 1 - \frac{\text{argmax}_\alpha \{S_{\phi=15^\circ-180^\circ}(\alpha, T_2, B_0)\}}{\text{argmax}_\alpha \{S_0(\alpha, T_2, B_0)\}} \quad (3.2)$$

where S_ϕ corresponds to the steady state signal acquired immediately after the binomial excitation scheme, S_0 relates to a single nonselective hard pulse excitation (corresponding to the limit of $\tau_\phi \rightarrow 0$), and argmax_α indicates that the flip angle was optimized for each parameter combination.

3.2.2 Imaging experiments

All measurements were performed either at 3T (Magnetom Verio, Siemens Medical Solutions, Erlangen, Germany) or at 7T (Magnetom 7T, Siemens Medical Solutions, Erlangen, Germany). In vivo knee scans of healthy volunteers were acquired with main focus on the menisci and the connective tissues. The experiments were approved by the local ethics committee and informed consent was obtained from all the volunteers prior to scanning. A dedicated 15-channel transmit / receive coil (Quality Electrodynamics (QED), Mayfield Village, OH, United States) was used at 3T and a dedicated 28-channel knee coil (QED) at 7T.

At 3T, in complete analogy to the simulations, nonselective RF pulse excitation (150 μs duration) was compared to water-selective excitation using 1-1 binomial excitation schemes (150 μs sub-pulse duration) with 45°, 90° and 180° phase evolution for the fat component for flip angles ranging between 4° and 8°. The field-of-view (FOV) was 140 mm and a volume of 44 slices with 2.5 mm slice thickness was scanned yielding an in-plane resolution of 0.55 mm for a bandwidth of 528 Hz / pixel. An echo time of 0.8 ms was achieved with 14.8% readout asymmetry (i.e., instead of 100% before the center of k-space) with a repetition time of 6 ms and the total acquisition time was 1.07 min. In order to minimize the signal modulations related to B_0 inhomogeneities, field maps were acquired prior to scanning [32, 33]. Furthermore, the frequency of the scanner was manually adjusted prior to every image acquisition in order to minimize possible frequency drift effects. Finally, the same protocol as for the water excitation scans was applied for a flip angle = 7° with a standard fat saturation prepulse of total preparation time 12.2 ms. In this case the repetition time was 18 ms and the total acquisition time 3.23 min. The protocol setup was as similar as possible to the protocol with the binomial pulses and no parallel imaging techniques were used.

At 7T 3D datasets of 120 slices with 1 mm slice thickness were acquired with and without water excitation and with varying phase advance (i.e., 45°, 90° and 180° phase evolution for the fat component). In this case, high resolution images (i.e., 0.18 mm in-plane for a FOV of 140 mm) were acquired at the optimal flip angle (i.e., 6° for a repetition time of 5.3 ms) according to Ernst Angle (assuming T_1 is equal to 1000 ms). An echo time of 0.83 ms was achieved with 10% readout asymmetry. The excitation pulse was 100 μs and the total acquisition time 3.25 ms.

3.3 Results

Simulation of binomial excitation of short T_2 components

The expected relative signal loss (Δs) from binomial excitation in comparison to a non-spectrally selective excitation is analyzed in Fig. 3.2, as a function of T_2 for a magnetic field of 3T and 7T. It is common to both curves that a maximum loss occurs at the limit of short T_2 (0.1 ms) and decreases for increasing values of T_2 . As might be expected, a reduced signal loss is observed with increasing main magnetic field strength from the reduced interpulse spacing τ_ϕ (cf. Eq. 3.2), and is typically marginal for $T_2 \gg \tau$: at 7T, it is below 5% for all three binomial schemes for T_2 larger than 3 ms, whereas at 3T, only for relaxation times larger than approximately 8 ms a reduction of the signal loss below 5% is observed. For fibrous tissue components with

an expected $T_2 \sim 1$ ms, the predicted signal loss from binomial excitation is about 27% for $1_{45^\circ}1$ and about 19% for $1_{90^\circ}1$ and $1_{180^\circ}1$ at 3T and 16%, 10% and 12% respectively at 7T. For components with an expected $T_2 \sim 5$ ms, the predicted signal loss from binomial excitation is about 9% for $1_{45^\circ}1$ and about 5% and 6% for $1_{90^\circ}1$ and $1_{180^\circ}1$ at 3T, while at 7T it is 4%, 2% and 3% for $1_{45^\circ}1$, $1_{90^\circ}1$ and $1_{180^\circ}1$ respectively. Interestingly, the $1_{45^\circ}1$ binomial scheme performs markedly worse than the $1_{90^\circ}1$ and $1_{180^\circ}1$ preparations, although its interpulse spacing is shortest. This might be attributed to saturation effects, due to the fact that the phase of the second RF pulse for the $1_{45^\circ}1$ is not parallel to the x axis or y axis and needs a higher flip angle for each sub-pulse.

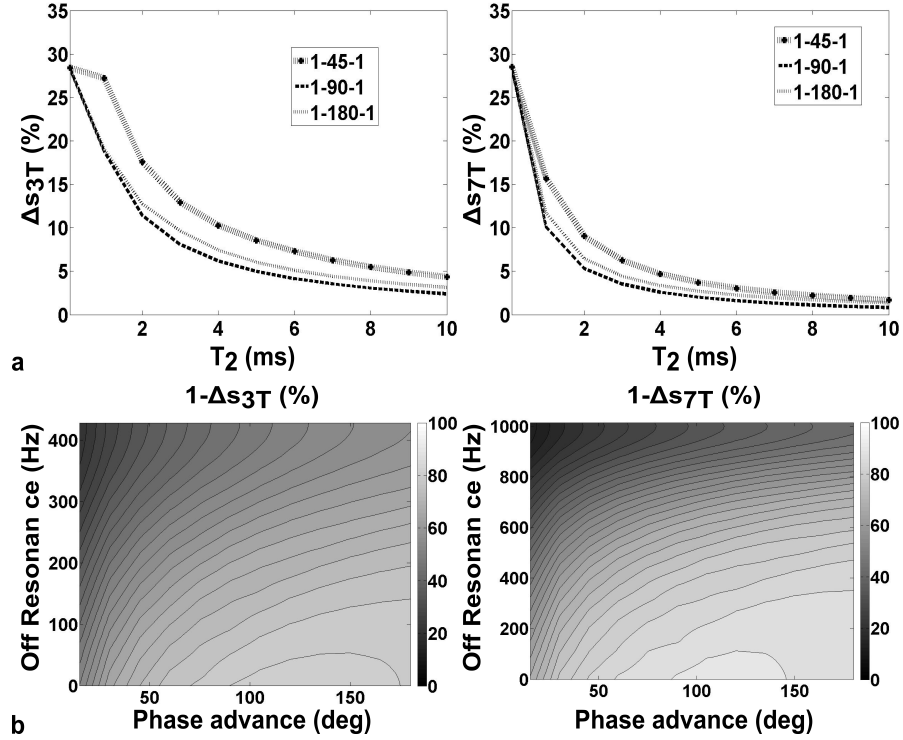


Figure 3.2: a. Graph that shows the signal loss $\Delta s (T_{2=0.1-10\text{ms}}) (\%)$ in comparison to non-spectrally selective excitation calculated according to Eq. 3.2 for field strengths of 3T (left top) and 7T (right top) and binomial schemes $1_{45^\circ}1$, $1_{90^\circ}1$ and $1_{180^\circ}1$, b. Graph that shows the signal loss $1 - \Delta s (T_2 = 1\text{ms}) (\%)$ at 3T and 7T versus different phase advance between the binomial sub-pulses and for different off-resonance. The off-resonance is modified from 0 to the resonance frequency of fat (i.e., from 0 to 428 Hz at 3T and from 0 to 1014 Hz at 7T).

Additionally, the signal loss was depicted versus the phase advance of the off-resonant component between the sub-pulses (see Fig. 3.2b) for different values of the off-resonance (i.e., 0-428 Hz for 3T and 0-1014 Hz for 7T). It is observed that off-resonance effects influence more schemes employing smaller phase advance between the binomial sub-pulses such as 45° . Interestingly, the signal loss reaches a minimum (i.e., highest values of $1 - \Delta s$) around 90° and increases again for increasing phase values towards 180° (see Fig. 3.2b).

In vivo validation at 3T and 7T

For in vivo validation, the signal from highly ordered tissue components, such as the meniscus and the patellar ligament, was analyzed at 3T over the range of practically relevant flip angles for the three binomial excitation schemes with corresponding phase evolution $\phi = 45^\circ, 90^\circ, 180^\circ$. Sample images of sagittal orientation acquired with the optimal flip angle for the meniscus according to the experiments (i.e., a nominal flip angle of 7°) are presented on Fig. 3.3.

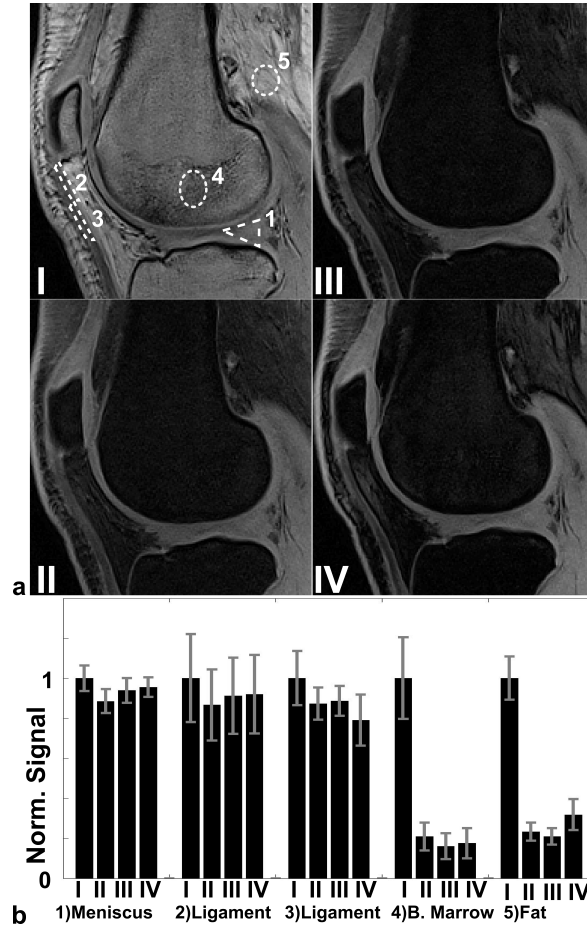


Figure 3.3: a) Sample images of sagittal orientation acquired with a nominal flip angle of 7° are presented for different water excitation schemes: I) conventional, II) $1_{45^\circ}1$, III) $1_{90^\circ}1$ and IV) $1_{180^\circ}1$, b) Average signal with the different excitation schemes, which corresponds to the images on Fig. 3.3a, normalized to the signal of the non-spectrally selective excitation for each ROI for the respective regions shown in Fig. 3.3a.

As can be expected, due to heterogeneities in the main magnetic field, spectral excitation is partly incomplete in the subcutaneous tissue and performs best for the $1_{90^\circ}1$ preparation. Close to the image center, however, where B_0 inhomogeneities are minimal due to better shim, fat suppression is robust for all schemes investigated.

In agreement with the simulations, the meniscus signal loss due to the $1_{90^\circ}1$ and $1_{180^\circ}1$, is

similar and lower than with the $1_{45^\circ}1$ (see Fig. 3.3). The relative signal intensity (S) at the optimal flip angle, which was 7° for the meniscus, according to the experiments is presented in Fig. 3.3b. The experimental results show $\sim 1.5\%$ lower signal loss than expected for the simulations for $1_{180^\circ}1$ and about $\sim 1\%$ and 3% higher than expected for $1_{90^\circ}1$ and $1_{45^\circ}1$ respectively if we assume a $T_2 = 5$ ms for the meniscus. For tissues with lower T_2 on the order of 1 ms, such as the patellar ligament, the maximum signal loss in comparison to a simple nonselective excitation is about 3% higher than for the meniscus (see Fig. 3.3b, ROI₂ for the patellar ligament). The results are comparable to what we would expect from the simulations for T_2 values between 1 and 3.5 ms.

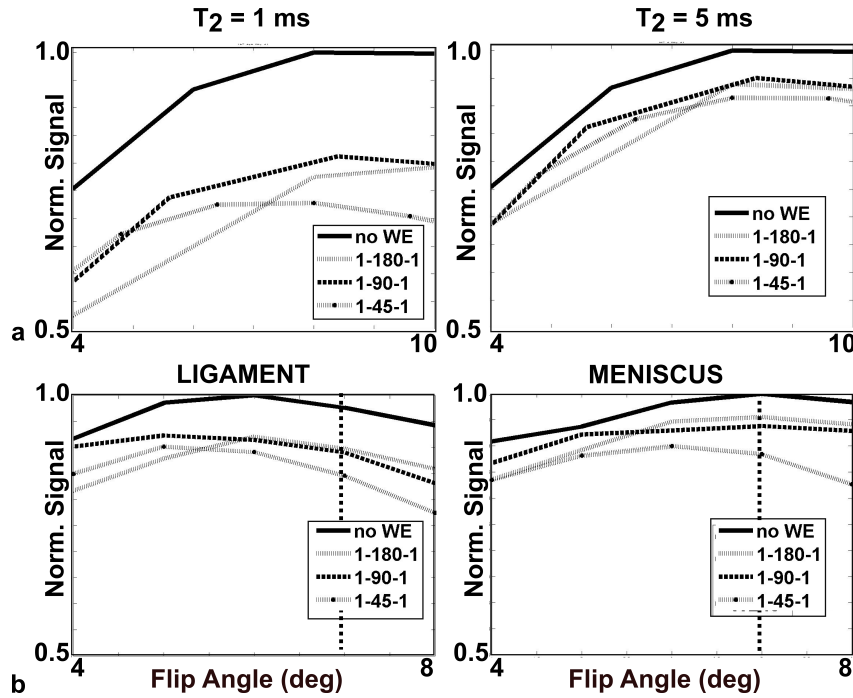


Figure 3.4: a) The simulated steady state signal just after excitation is depicted versus the effective flip angle for different flip angles at $3T$ (i.e., $4-10^\circ$ assuming $TR = 6$ ms) and two different T_2 values (1 ms and 5 ms) for different binomial schemes $1_{45^\circ}1$, $1_{90^\circ}1$ and $1_{180^\circ}1$ and for non-spectrally selective excitation, b) The signal of a ROI (see Fig. 3.3a) of the posterior lateral meniscus (ROI₁) and of a ROI of the patellar ligament (ROI₂) closer to the patella is depicted versus the flip angle from sagittal images acquired with different flip angles at $3T$ and for different excitation schemes (with conventional nonselective excitation and with water excitation preparation $1_{45^\circ}1$, $1_{90^\circ}1$ and $1_{180^\circ}1$).

On Fig. 3.4a the relative signal amplitude (as a result of the simulations) for the different excitation schemes is depicted for $T_2 = 1$ and 5 ms versus the flip angle (i.e., the nominal flip angle for nonselective excitation and the effective flip angle for the binomial schemes). It can be observed that the difference between the various excitation schemes reduces for increasing T_2 values. In agreement with the simulations, the meniscus signal loss (as a result of the experiments) due to the $1_{90^\circ}1$ and $1_{180^\circ}1$ is similar and lower than with the $1_{45^\circ}1$ (see Fig. 3.4b).

$1_{45^\circ}1$ according to the experiments performs worse than expected, which could be attributed to off-resonance effects. Finally, as expected from the simulations the optimal flip angle for the meniscus is higher than for patellar ligament.

In general, in agreement with the simulations, the signal loss due to the $1_{90^\circ}1$ and $1_{180^\circ}1$ is similar and lower than with the $1_{45^\circ}1$ (see Fig. 3.3 and 3.4). However, for the patellar ligament a second ROI (ROI₃, see Fig. 3.3a) was analyzed in a region of the ligament with lower intensity. Here, in contrast to the simulations the $1_{45^\circ}1$ performs better than the $1_{180^\circ}1$ and with $1_{90^\circ}1$ there is the lowest signal loss. For $1_{90^\circ}1$ the absolute values are slightly lower than what we would expect but nevertheless the two curves (i.e., $1_{180^\circ}1$ and $1_{90^\circ}1$) are rather comparable, which can also be seen in the simulation, and this deviation might be attributed to the much lower T_2 of the part of the patellar ligament.

As compared to the standard FATSAT preparation for flip angles of 7° (see Fig. 3.5), the signal from short T_2 tissues, such as the menisci or the patellar ligaments, exhibits a much higher signal with the binomial excitation scheme. More specifically for the ROIs indicated on Fig. 3.5a and b) the signal is much higher on the menisci and the patellar ligament and slightly lower on ROIs containing fat (see Fig. 3.5c). Overall, the quality of fat suppression was comparable on the center of the FOV and more effective with the binomial excitation scheme off-center (see Fig. 3.5c).

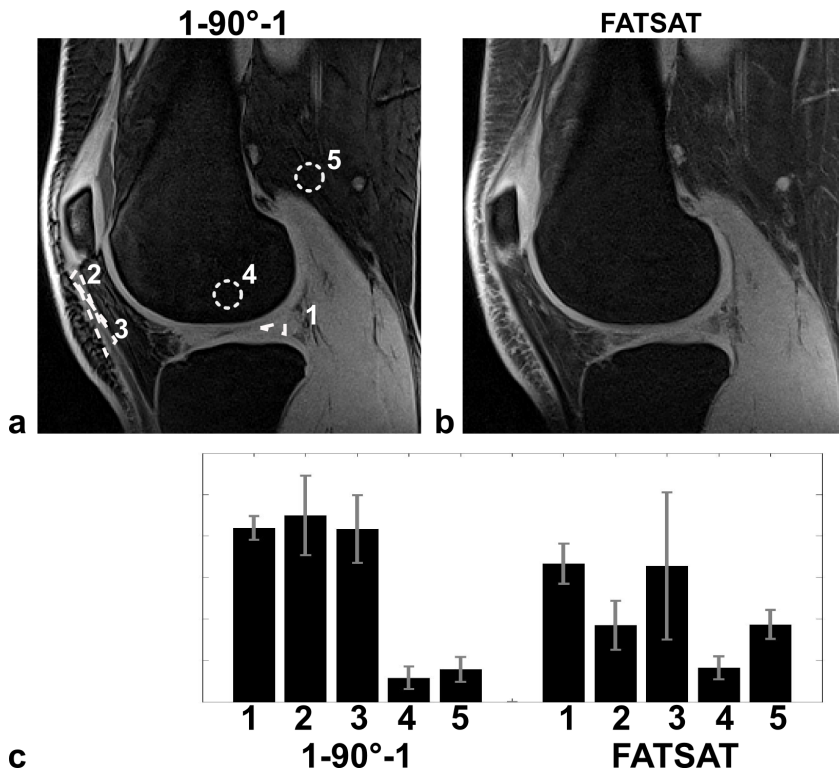


Figure 3.5: Sample sagittal images of the knee joint acquired with a flip angle 7° at 3T with two different fat suppression schemes: a) fast water excitation with 90 degrees phase advance, b) standard fat saturation preparation, c) average signal on selected ROIs (see Fig. 3.5a).

Finally, according to the experiments at 7T (see Fig. 3.6, ROI₁ and Fig. 3.7) the relative signal of the lateral meniscus has a signal loss (see Fig. 3.7) of $\sim 0.4\%$ due to $1_{90^\circ}1$ and $\sim 8.2\%$ due to $1_{45^\circ}1$. There is practically no signal difference between the $1_{180^\circ}1$ and the nonselective excitation. The suppression of the lipid signal from the trabecular bone marrow signal (see Fig. 3.6, ROI₄) is $\sim 62.5\%$, $\sim 65\%$ and $\sim 75.6\%$ with $1_{180^\circ}1$, $1_{90^\circ}1$ and $1_{45^\circ}1$ respectively. The $1_{90^\circ}1$ is the optimal scheme for simultaneous fat suppression and visualization of the meniscus (see Fig. 3.7). For the patellar ligament, however, there is a greater signal loss with the binomial excitation with respect to the nonselective excitation. The signal loss of the patellar ligament (see Fig. 3.6, ROI₂ and Fig. 3.7) with the $1_{180^\circ}1$, $1_{90^\circ}1$ and $1_{45^\circ}1$ was respectively 12%, 13% and 21% for $1_{180^\circ}1$, $1_{90^\circ}1$ and $1_{45^\circ}1$ (see Fig. 3.7). The experimental results are comparable to the expected signal loss from the simulations for a T_2 of 0.9 ms, which is $\sim 12\%$ for $1_{180^\circ}1$ and $1_{90^\circ}1$ and $\sim 18\%$ for $1_{45^\circ}1$. Also in this case a second region of the ligament which is characterized by signal of lower signal-to-noise ratio was analyzed (see Fig. 3.6 ROI₃ and Fig. 3.7) and similarly, as in the experiments at 3T, the $1_{45^\circ}1$ leads to less signal loss than the $1_{180^\circ}1$.

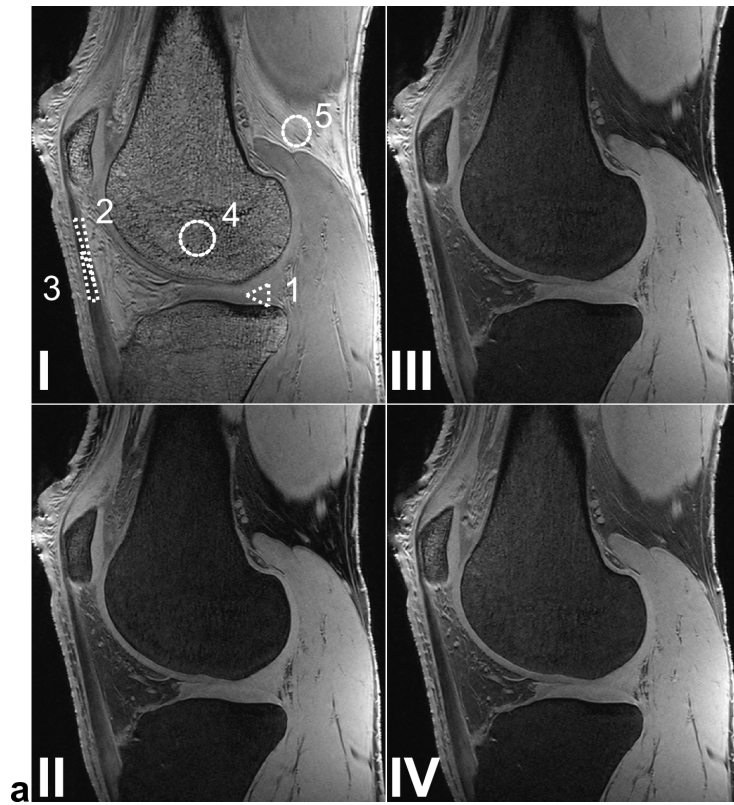


Figure 3.6: Sample images of a healthy volunteer at ultra high field (7T) a conventional short nonselective excitation (I) and with a fast water excitation scheme (II) $1_{45^\circ}1$, (III) $1_{90^\circ}1$ and (IV) $1_{180^\circ}1$.

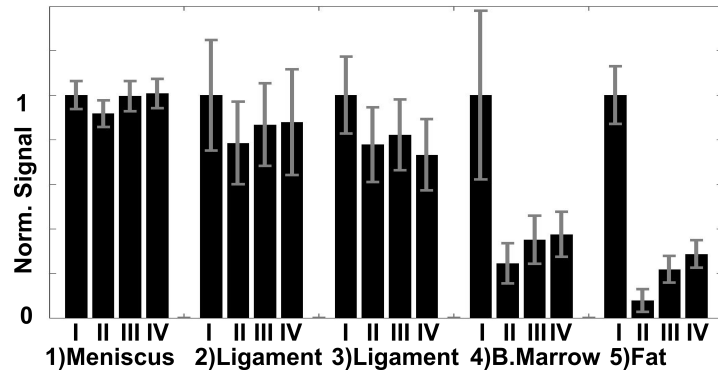


Figure 3.7: Average signal as calculated from the experiments 7T, normalized to the signal of the non-spectrally selective excitation for each ROI (see Fig. 3.6). The signal with $190^\circ 1$ and $1180^\circ 1$ excitation is comparable and lower than with nonselective excitation, while $145^\circ 1$ yields less signal. A relative reduction in the signal of 8.2% and 0.4% is observed for the meniscus (ROI₁) respectively for $145^\circ 1$ and $190^\circ 1$ and no signal loss for $1180^\circ 1$. The signal of the patellar ligament (ROI₂) is reduced 21%, 13% and 12% for $145^\circ 1$, $190^\circ 1$ and $1180^\circ 1$ in respect to a simple nonselective excitation.

3.4 Discussion

The possible benefit of spectrally selective water excitation over conventional FATSAT preparation method for visualization of short T_2 MSK components was analyzed. The T_2 of such highly ordered tissue components typically lies in the several hundreds microseconds for tendons to the millisecond range for menisci and ligaments. Our results indicate that a maximum signal loss from binomial excitation of about 30% in the limit of very short T_2 (0.1 ms), as compared to non-selective imaging; leveling off faster with increasing field strength to about 19% at 3T and 10% at 7T for a T_2 of 1 ms. In agreement with simulations, phase of about 90° yielded minimum signal loss: For menisci the signal loss was about 5% and 0-1% at 3T and 7T, whereas for the ligaments 9% and 13%. Finally, measurements at 3T revealed considerable lower signal loss at 3T in comparison to FATSAT.

In 2007 Hauger et al. [15] presented a comparison of fat saturation and water excitation based on a spin echo sequence. In our comparison using gradient echo sequences, we analyzed a short echo time sequence based on vTE SPGR approach to show that MSK imaging of short-lived T_2 components can benefit from the combination of a technique providing simultaneous fat suppression and short TE. Overall, spectral water excitation based on short binomial excitation showed similar fat suppression quality, but offered improved signal-to-noise: binomial excitation not only provided higher signal levels for short T_2 components than FATSAT methods, but it was evident that the sequence efficiency could be considerably increased, since there is no additional time required for magnetization preparation.

Frequently, a phase evolution of 180° is used in combination with binomial excitation schemes. In practice, however, our results indicate that a phase advance of 90° can offer comparable fat suppression quality and is more advantageous in several cases. From the simulations and experimental results, the $190^\circ 1$ excitation scheme is less sensitive to main magnetic field inhomogeneities as compared to the $1180^\circ 1$, while the quality of fat suppression is comparable in both cases. Also, both the simulations and the experiments underline the fact that although

for long T_2 tissues it is not important, for short T_2 tissues, as well as for lower field strengths, the choice of the water–fat phase evolution for the binomial pulses is important since especially with 45° phase evolution there is a non-negligible signal loss.

In this chapter, binomial excitation was combined with a Cartesian short TE SPGR sequence to validate the theoretical predictions. However the results presented herein can be generalized to any short or ultra-short TE imaging sequence. Overall, binomial excitation schemes for imaging of short-lived T_2 species outperform conventional FATSAT preparation techniques and prove to be especially beneficial at ultra-high field strength, where the signal loss due to reduced interpulse spacing becomes marginal.

In conclusion, the use of binomial excitation in combination with a short echo time sequence as opposed to using FATSAT preparation was demonstrated to be beneficial for imaging of short T_2 MSK tissues. In addition, a 90° phase advance was shown to be comparable and even more advantageous in comparison to the commonly used 180° phase advance when the focus of interest is highly ordered components in MSK.

References

- [1] C. J. Bergin, J. M. Pauly, and A. Macovski, "Lung parenchyma: projection reconstruction MR imaging," *Radiology*, vol. 179, pp. 777–781, June 1991. PMID: 2027991.
- [2] P. D. Gatehouse and G. M. Bydder, "Magnetic resonance imaging of short t2 components in tissue," *Clin Radiology*, vol. 58, pp. 1–19, Jan. 2003. PMID: 12565203.
- [3] M. D. Robson, P. D. Gatehouse, M. Bydder, and G. M. Bydder, "Magnetic resonance: an introduction to ultrashort TE (UTE) imaging," *J Comput Assist Tomogr*, vol. 27, pp. 825–846, Dec. 2003. PMID: 14600447.
- [4] P. A. Hardy, M. P. Recht, and D. W. Piraino, "Fat suppressed MRI of articular cartilage with a spatial-spectral excitation pulse," *J Magn Reson Imaging*, vol. 8, pp. 1279–1287, Dec. 1998. PMID: 9848740.
- [5] J. Hennig and O. Speck, eds., *High-Field MR Imaging*. Springer, 2011 ed., Nov. 2011.
- [6] A. Techawiboonwong, H. K. Song, and F. W. Wehrli, "In vivo MRI of submillisecond t(2) species with two-dimensional and three-dimensional radial sequences and applications to the measurement of cortical bone water," *NMR Biomed*, vol. 21, pp. 59–70, Jan. 2008. PMID: 17506113.
- [7] J. Du, A. M. Takahashi, W. C. Bae, C. B. Chung, and G. M. Bydder, "Dual inversion recovery, ultrashort echo time (DIR UTE) imaging: creating high contrast for short-t(2) species," *Magn Reson Med*, vol. 63, pp. 447–455, Feb. 2010. PMID: 20099332.
- [8] R. R. Regatte and M. E. Schweitzer, "Ultra-high-field MRI of the musculoskeletal system at 7.0T," *J Magn Reson Imaging*, vol. 25, pp. 262–269, Feb. 2007. PMID: 17260399.
- [9] J. Frahm, A. Haase, W. Hänicke, D. Matthaei, H. Bomsdorf, and T. Helzel, "Chemical shift selective MR imaging using a whole-body magnet," *Radiology*, vol. 156, pp. 441–444, Aug. 1985. PMID: 4011907.
- [10] A. Haase, J. Frahm, W. Hänicke, and D. Matthaei, "1H NMR chemical shift selective (CHESS) imaging," *Phys Med Biol*, vol. 30, pp. 341–344, Apr. 1985. PMID: 4001160.
- [11] B. R. Rosen, V. J. Wedeen, and T. J. Brady, "Selective saturation NMR imaging," *J Comput Assist Tomogr*, vol. 8, pp. 813–818, Oct. 1984. PMID: 6470246.
- [12] T. A. Bley, O. Wieben, C. J. François, J. H. Brittain, and S. B. Reeder, "Fat and water magnetic resonance imaging," *J. Magn. Reson. Imaging*, vol. 31, no. 1, p. 4–18, 2010.
- [13] P. Hore, "Solvent suppression in fourier transform nuclear magnetic resonance," *Journal of Magnetic Resonance (1969)*, vol. 55, pp. 283–300, Nov. 1983.
- [14] O. Bieri, T. C. Mamisch, S. Trattnig, O. Kraff, M. E. Ladd, and K. Scheffler, "Optimized spectrally selective steady-state free precession sequences for cartilage imaging at ultra-high fields," *Magn Reson Mater Phy*, vol. 21, pp. 87–94, Mar. 2008. PMID: 18030512.
- [15] O. Hauger, E. Dumont, J.-F. Chateil, M. Moinard, and F. Diard, "Water excitation as an alternative to fat saturation in MR imaging: preliminary results in musculoskeletal imaging," *Radiology*, vol. 224, pp. 657–663, Sept. 2002. PMID: 12202695.
- [16] H. Graichen, V. Springer, T. Flaman, T. Stammberger, C. Glaser, K. H. Englmeier, M. Reiser, and F. Eckstein, "Validation of high-resolution water-excitation magnetic resonance imaging for quantitative assessment of thin cartilage layers," *Osteoarthritis Cartilage*, vol. 8, pp. 106–114, Mar. 2000. PMID: 10772240.

- [17] L. Heudorfer, J. Hohe, S. Faber, K. H. Englmeier, M. Reiser, and F. Eckstein, “[precision MRI-based joint surface and cartilage density analysis of the knee joint using rapid water-excitation sequence and semi-automatic segmentation algorithm],” *Biomedizinische Technik. Biomedical engineering*, vol. 45, pp. 304–310, Nov. 2000. PMID: 11155531.
- [18] C. Glaser, S. Faber, F. Eckstein, H. Fischer, V. Springer, L. Heudorfer, T. Stammberger, K. H. Englmeier, and M. Reiser, “Optimization and validation of a rapid high-resolution t1-w 3D FLASH water excitation MRI sequence for the quantitative assessment of articular cartilage volume and thickness,” *Magn Reson Imaging*, vol. 19, pp. 177–185, Feb. 2001. PMID: 11358655.
- [19] A. Mohr, M. Priebe, B. Taouli, J. Grimm, M. Heller, and J. Brossmann, “Selective water excitation for faster MR imaging of articular cartilage defects: initial clinical results,” *Eur Radiol.*, vol. 13, pp. 686–689, Apr. 2003. PMID: 12664103.
- [20] Y. Zur, “Design of improved spectral-spatial pulses for routine clinical use,” *Magn Reson Med*, vol. 43, pp. 410–420, Mar. 2000. PMID: 10725884.
- [21] M. A. Bernstein, K. F. King, and X. J. Zhou, *Handbook of MRI Pulse Sequences*. Elsevier, Sept. 2004.
- [22] W. E. Kwok, S. M. Totterman, and J. Zhong, “3D interleaved water and fat image acquisition with chemical-shift correction,” *Magn Reson Med*, vol. 44, no. 2, p. 322–330, 2000.
- [23] K. Mori, N. Takahashi, M. Hiratsuka, M. Shiigai, M. Minami, T. Oda, N. Ohkohchi, and Y. Morishita, “Detection of hepatic metastases using ferucarbotran-enhanced MR imaging: Feasibility and diagnostic accuracy of three-dimensional sensitivity-encoding water-excitation multishot echo-planar sequence (3D-SWEEP),” *J. Magn. Reson. Imaging*, vol. 24, no. 5, p. 1110–1116, 2006.
- [24] T. Zhao, H. Zheng, Y. Qian, T. Ibrahim, and F. Boada, “Using the binomial RF pulses for selective excitation of the ultra-short t2 component,” in *Proceedings 20th Scientific Meeting, International Society for Magnetic Resonance in Medicine*, p. 4154, 2012.
- [25] Y. Ye, J. Hu, and E. M. Haacke, “Robust selective signal suppression using binomial off-resonant rectangular (BORR) pulses,” *J. Magn. Reson. Imaging*, 2013.
- [26] F. Springer, G. Steidle, P. Martirosian, U. Grosse, R. Syha, C. Schabel, C. D. Claussen, and F. Schick, “Quick water-selective excitation of fast relaxing tissues with 3D UTE sequences,” *Magn Reson Med*, Feb. 2013. PMID: 23440968.
- [27] D. Thomasson, D. Purdy, and J. P. Finn, “Phase-modulated binomial RF pulses for fast spectrally-selective musculoskeletal imaging,” *Magn Reson Med*, vol. 35, pp. 563–568, Apr. 1996.
- [28] G. R. Morrell, “Rapid fat suppression in MRI of the breast with short binomial pulses,” *J Magn Reson Imaging*, vol. 24, pp. 1172–1176, Nov. 2006. PMID: 17036329.
- [29] H.-Y. Lin, S. V. Raman, Y.-C. Chung, and O. P. Simonetti, “Rapid phase-modulated water excitation steady-state free precession for fat suppressed cine cardiovascular MR,” *J Cardiovasc Magn Reson*, vol. 10, p. 22, 2008. PMID: 18477396.
- [30] X. Deligianni, P. Bär, K. Scheffler, S. Trattinig, and O. Bieri, “High-resolution fourier-encoded sub-millisecond echo time musculoskeletal imaging at 3 tesla and 7 tesla,” *Magn Reson Med.*, vol. doi: 10.1002/mrm.24578, 2012.

- [31] E. T. Jaynes, “Matrix treatment of nuclear induction,” *Physical Review*, vol. 98, pp. 1099–1105, May 1955.
- [32] F. Santini, S. Patil, and K. Scheffler, “IceLuva: a scripting framework for MR image reconstruction based on free software,” *Concepts Magn Reson B Magn Reson Eng*, vol. 39B, pp. 1–10, Feb. 2011.
- [33] C. Lenz, O. Bieri, K. Scheffler, and F. Santini, “Simultaneous b1 and b0 mapping using dual-echo actual flip angle imaging (DE-AFI),” in *Proceedings 19th Scientific Meeting, International Society for Magnetic Resonance in Medicine*, 2011.

Chapter 4

In vivo visualization of cells labeled with superparamagnetic iron oxides by a sub-millisecond gradient echo sequence

An adapted version of this chapter is submitted as: **Deligianni X**, Jiráček D, Scheffler K, Berková Z, Hájek M and Bieri O, In vivo visualization of cells labeled with superparamagnetic iron oxides by a sub-millisecond gradient echo sequence, Magn Reson Mater Phy

4.1 Introduction

Superparamagnetic iron oxide nanoparticles (SPIO) induce strong susceptibility effects that lead to a pronounced shortening of both T_2 and T_2^* relaxation times. Single cells are not visible with MRI, but can be traced upon labeling with SPIO [1–3]. One of the most successful applications of cell imaging is the monitoring of transplanted pancreatic islets (PIs). Transplantation of PIs into the liver represents a promising alternative treatment to the well-established pancreas organ transplantation for restoring normoglycemia in type 1 diabetes mellitus patients [4, 5]. In 2004, Jirak et al. demonstrated that SPIO-labeled pancreatic islets can be detected as hypointense spots on T_2^* images following transplantation into the rat liver [6]. Since then many other studies have been performed to monitor the fate of labeled PIs with MRI on animal models [7–9]. Recently Jiao et al. confirmed that ex vivo cell labeling for islet graft imaging and monitoring with a 3T clinical scanner is feasible and advantageous over 1.5T since the susceptibility effect of iron nanoparticles is amplified [8].

Non-invasive islet graft MR-imaging is successfully applied in human livers up to 6 months after transplantation despite signal loss due to the clearance of the labeling from the islets [7, 10–12]. Although the signal loss is clearly visible and can be monitored, quantitative or serial studies are not easily performed [10, 13, 14]. Typically the iron-labeled islets appear as hypointense spots on MRI, but susceptibility artifacts such as the presence of air, air and tissue interfaces and other effects like calcification and flow-related signal losses also provide negative contrast, and reliable detection of false positives can become an issue. In addition, using the signal void as a means of detection can be hindered by severe partial volume effects [14]. As a result, positive contrast MR techniques [15–18] such as double echo ultra short echo time (UTE) methods were proposed to prevent such false positive results [19]. Recently, the feasibility of quantitative imaging and automatic thresholding of islets labeled with iron oxides with a positive contrast UTE-based MRI method was shown [19–21]. UTE allows successful islet detection in rats, but image acquisition requires respiratory triggering, which in this case was achieved with a specialized respiratory pad system [19]. In humans, however, UTE with respiratory triggering for abdominal imaging has not yet been applied.

In UTE techniques, it is common to use a subtraction image (i.e., subtracting a later echo from the UTE image) in order to yield positive contrast and increase the conspicuity in the detection of labeled islets [14, 21]. This kind of positive contrast serves in reducing false positives, but in principle the two images could also be used for weighted subtraction in order to yield a weighted positive contrast. In 2013 Martirosian et al. proposed a relative subtraction method to enhance the positive contrast in a modified DESS sequence [22].

Contemporary imaging protocols used in standard clinical practice for the follow-up of the islet grafts in patients include balanced steady-state free precession (bSSFP) and spoiled gradient echo (SPGR) sequences [11]. Gradient echo methods provide good anatomic liver images, but usually only a few 2D slices can be acquired in a breath-hold. The goal of this chapter was to develop an MRI technique for 3T scanners that could

monitor the fate of transplanted labeled islets in patients. As a result, we modified a contemporary sequence that was already being used in the clinic for the screening of diabetic patients after transplantation. Instead of the typically implemented 2D protocol, we used a 3D protocol to achieve larger volume coverage with improved signal-to-noise ratio. A Cartesian sub-millisecond echo time SPGR 3D sequence was used and optimized for the in vivo visualization of SPIO-labeled PIs in the liver in order to yield positive contrast images from patient single-breath-hold imaging. Visualization of pancreatic islets was explored with conventional and weighted subtraction images. The variable echo time scheme in combination with a highly asymmetric readout, as demonstrated in a previous study [23], allowed an important reduction of the echo time down to 0.65 ms while simultaneously achieving a sufficiently high resolution (i.e., $1.3 \times 1.3 \text{ mm}^2$ in-plane) for in vivo scanning of humans.

4.2 Methods

Animal experiments

All protocols were approved by the Ethics Committee of the Institute for Clinical and Experimental Medicine and the Committee for Animal Care of the 2nd Faculty of Medicine of Charles University. The experiments were carried out in accordance with the European Communities Council Directive of 24 November 1986 (86/609/EEC).

Islet isolation, labeling and transplantation for animal experiments

Male Lewis rats (Anlab, Czech Republic) were used as islet donors, as well as recipients for in vivo experiments. The pancreases of donor rats were distended by collagenase (1 mg/ml; Sevapharma, Czech Republic) and incubated at 37°C in a water bath for 20 minutes. The islets were separated from exocrine tissue by centrifugation in a discontinuous Ficoll gradient (Sigma, USA). Purified islets were cultivated in CMRL-1066 medium (PANBiotech GmbH, Germany) supplemented with 10% fetal calf serum, 1% penicillin/streptomycin/L-glutamine and 1% HEPES (all reagents from Sigma, USA) in a humidified CO₂ incubator at 37°C and 5% CO₂ atmosphere. For islet labeling, the MR contrast agent ferucarbotran (RESOVIST®; Schering AG, Germany) was used (5 µl/ml) and pancreatic islets were cultured for 24 hours. Before transplantation, labeled islets were washed three times in Hanks Balanced Saline Solution (Sigma, USA). 1500 hand-picked labeled islets were transplanted under general anesthesia into the portal vein of recipients.

Human islet isolation, labeling and transplantation

After purification and washing, the islets were transferred into the culture medium CMRL-1066 (PAN Biotech GmbH, Germany), which was modified and supplemented according to the Miami Center. Before culture MRI contrast agent ferucarbotran 5 µL/mL ferucarbotran (RESOVIST®; Schering AG, Germany) was added. The islets

were in culture for 24 hours and before transplantation, the labeled islets were washed again in the culture medium to remove the free ferucarbotran. Then 320000 islet equivalents were infused in local anesthesia percutaneously under radiologic control into the portal vein within approximately 60 min.

MRI Imaging

Sub-millisecond SPGR sequence

A double contrast selective 3D SPGR sequence with a variable first echo time (TE) in combination with a highly asymmetric readout was used [23]. Here, the TE of the first echo varies dynamically across k-space enabling a minimum effective echo time, while highly asymmetric sampling allows reducing the echo time even further. Both echoes were acquired after each single excitation. This provided sub-millisecond TE for the first echo, as a key for positive contrast imaging and monitoring of islets labeled with SPIO. A 3D sequence enables the acquisition of multiple contiguous slices to facilitate the islet detection. A special projection onto convex sets algorithm [24] provided by the manufacturer was used to compensate for the asymmetric data sampling.

Positive contrast and relative subtraction images

In order to yield positive contrast, a later echo was subtracted from the sub-millisecond first echo and the image difference was reconstructed online [25]. Apart from the subtraction images, weighted subtraction images were also produced in post-processing. As it has been demonstrated by Martirosian et al. [22], by adding a weighting factor the positive contrast can appear significantly higher. Relative subtraction images were reconstructed offline with Matlab 7.0 (The Mathworks, Inc., MA, USA, R2008b) according to the following formula:

$$\frac{S_{TE_1} - S_{TE_2}}{S_{TE_1} + S_{TE_2}} \quad (4.1)$$

where S_{TE_1} is the signal from the first short echo and S_{TE_2} the signal from the later echo.

Contrast analysis

In order to yield a quantitative estimation of the quality of the contrast, relative contrast-to-noise ratios (CNR) were calculated according to the following equation:

$$CNR = \frac{S_{ROI} - S_{BG}}{S_{ROI}} \quad (4.2)$$

where S_{ROI} is the signal intensity at the region-of-interest (ROI) of the labeled islets are detected and S_{BG} is the signal intensity of the ROI in the islets surroundings (i.e., the liver tissue in the animal and human scans).

Phantom imaging

Pancreatic rat and human islets were labeled with Resovist (Schering AG, Germany) for 1 day and were then inserted into a cylindrical gel phantom in order to test the sequence performance with respect to islet separation and detection. Human and rat islets were separated in two different small tubes and then placed in a larger cylindrical phantom filled with gel. Labeled islets were placed in the surrounding gel as well. Phantom scans were performed in a whole body 3T clinical system (Verio, Siemens Erlangen). For protocol details, see Table 4.1.

	Phantom	Rat scan	Patient scan
In-plane resolution (mm)	1.25	0.74	1.33
FOV (mm)	400 x 275	380 x 261	340 x 244
Slices / slice thickness (mm)	10 / 2.5	16 / 1.25	8 / 2.5
Bandwidth (Hz / pixel)	401	515	455
TE₁(ms) / RO asymmetry (%)^a	0.61 / 9	0.8 / 15.6	0.65 / 19.5
TE₂(ms) / RO asymmetry (%)^a	6 / 100	6 / 100	6 / 100
TR (ms) / Flip angle (°)	15 / 8	15 / 8	10 / 8
Acquisition time	23.11 sec	8.28 min	19 sec
Number of signal averages	1	4	2
Slice oversampling	60	50	50

^aRO asymmetry (Readout asymmetry): percentage of readout sampling before the center of k-space

Table 4.1: Protocol parameters used at 3T.

Animal MR imaging

The Lewis rat was scanned in a whole body clinical system (3T Tim Trio Siemens Erlangen) with a dedicated 8-channel transmit / receive animal coil (Rapid Biomedical). For protocol details, see Table 4.1. For reference, high resolution (0.23 mm in-plane) standard SPGR images (TE = 3.7 ms) were acquired using a 4.7T Bruker Biospec Spectrometer equipped with a resonator coil (Bruker, Germany). During the examination, anesthesia was induced and continued by spontaneous breathing of 3 % and 1-2 % isoflurane in the surrounding air, at 3T and 4.7T respectively.

Human MR imaging

The protocol was tested and evaluated on three healthy volunteers and subsequently a patient, who was a member of the cohort of patients studied under ENCITE project [www.encite.org], was scanned six months after transplantation [11] on a 3T whole body clinical scanner (Tim Trio, Siemens Erlangen). The study was approved by the Ethics Committee of the Institute for Clinical and Experimental Medicine. All participants of the project were informed about the nature and potential risks of the study and

signed their informed consent. The subjects were examined in supine position with a 6-channel body phased-array coil placed on the upper abdomen. The scan protocol apart from positive contrast images included conventional MR imaging (i.e., HASTE, balanced SSFP, 2D conventional SPGR) and the whole examination did not exceed one hour. The additional positive contrast scans increased the total scan protocol by three breath-hold scans of 19 s each (i.e., the acquisition was repeated to scan different parts of the liver); a 3D transverse dataset with 50% slice oversampling was acquired in a single breath-hold at end-expiration mode. GRAPPA acceleration of a factor 2 and Partial Fourier 6/8 in slice direction was used to reduce the scan time. The flip angle was adjusted in order to yield optimum signal from the liver so that the long T_2 species suppression would be optimal. For protocol details, see Table 4.1.

4.3 Results

4.3.1 Phantom scan

The sub-millisecond short echo time image (see Fig. 4.1A) exhibited homogenous signal and almost no hypointensities were present. In the second echo (see Fig. 4.1B), islets appeared as dark areas of smaller or bigger extent, as a result of the different amount of the contrast agent. In the image difference (see Fig. 4.1C) and in the relative image difference (see Fig. 4.1D), islets appeared as hyperintense areas which could be easily distinguished from the background.

The contrast of the islets looks similar in the image difference and in the relative image difference. Both images yielded better CNR in comparison to the late echo, while the CNRs with both positive contrast methods are almost identical (see Table 4.2). Only in one of the two ROIs the relative subtraction image performs slightly better (0.87 over 0.85). The smallest visible hyperintensities could be attributed to single islets, which was verified by visual observation.

		TE_1	TE_2	Pos. Contrast	Rel. Subtraction
Phantom	ROI₁	0.01	0.09	0.85	0.87
	ROI₂	0.03	0.08	1.03	1.03
Rat	ROI₁	0.05	0.24	0.18	0.28
	ROI₂	0.02	0.43	0.43	0.53
Patient	ROI₁	0.02	0.15	0.41	0.42
	ROI₂	0.03	0.45	0.64	0.72

Table 4.2: Evaluation of contrast-to-noise ratios for selected regions-of-interest. The ROIs are indicated on the figures of the relevant experiments. Positive contrast images have higher contrast than the second echo images and the relative subtraction images have comparable or higher ratios in comparison to positive contrast images.

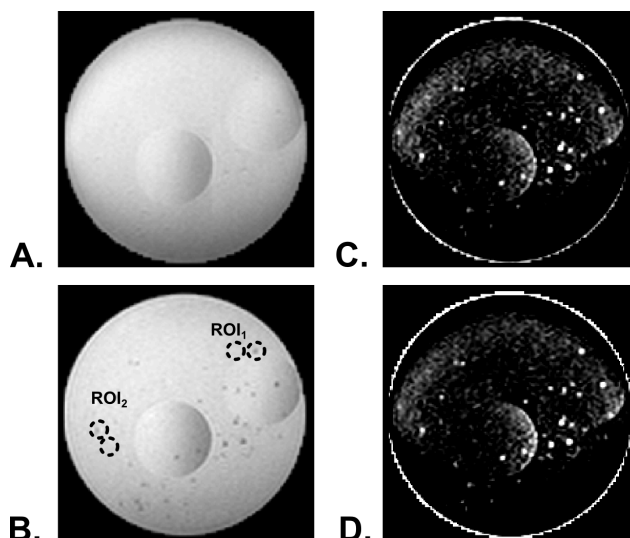


Figure 4.1: Cylindrical gel phantom with rat and human islets. The circular forms visible in the short (A) and long (B) echo image are smaller gel containers to separate the rat from the human islets. The images were acquired at 3T field strength: A) sub-millisecond first echo image acquired at 0.61 ms, B) second echo image acquired at 6 ms, C) positive contrast image (subtraction of the second echo from the first echo), where the islets appear as hyperintensities, D) relative subtraction image. The ROIs for which the CNRs were calculated are indicated on sub-figure (B).

4.3.2 Animal scan

In the animal subject, the liver exhibited completely homogenous signal in the sub-millisecond first echo image acquired with the proposed method (see Fig. 4.2Ai), while the labeled islets appear as dark spots in the second echo (see Fig. 4.2Aii). The CNR was sufficiently high to allow the reconstruction of a positive contrast image (see Fig. 4.2Aiii), on which the islets could be seen as hyperintense spots and were easily identified. On the relative subtraction images (see Fig. 4.2Aiv), equal amount of hyperintense spots are detected, while the contrast-to-noise is improved (see Table 4.2). As it can also be observed in the zoomed images (see Fig. 4.2B) the relative-subtraction images yield better contrast for the islets.

The location and presence of islets was confirmed by comparison to the high-resolution images from the experimental 4.7T scanner. The same position was confirmed by looking at bigger anatomical structures. On Fig. 4.2C a high resolution image from the experimental scanner is presented, which corresponds to the same position as the variable echo time (vTE) SPGR images (see Fig. 4.2A). By comparison of the respective images, it was possible to confirm that the contrast observed on the positive contrast images was indeed due to the presence of labeled islets.

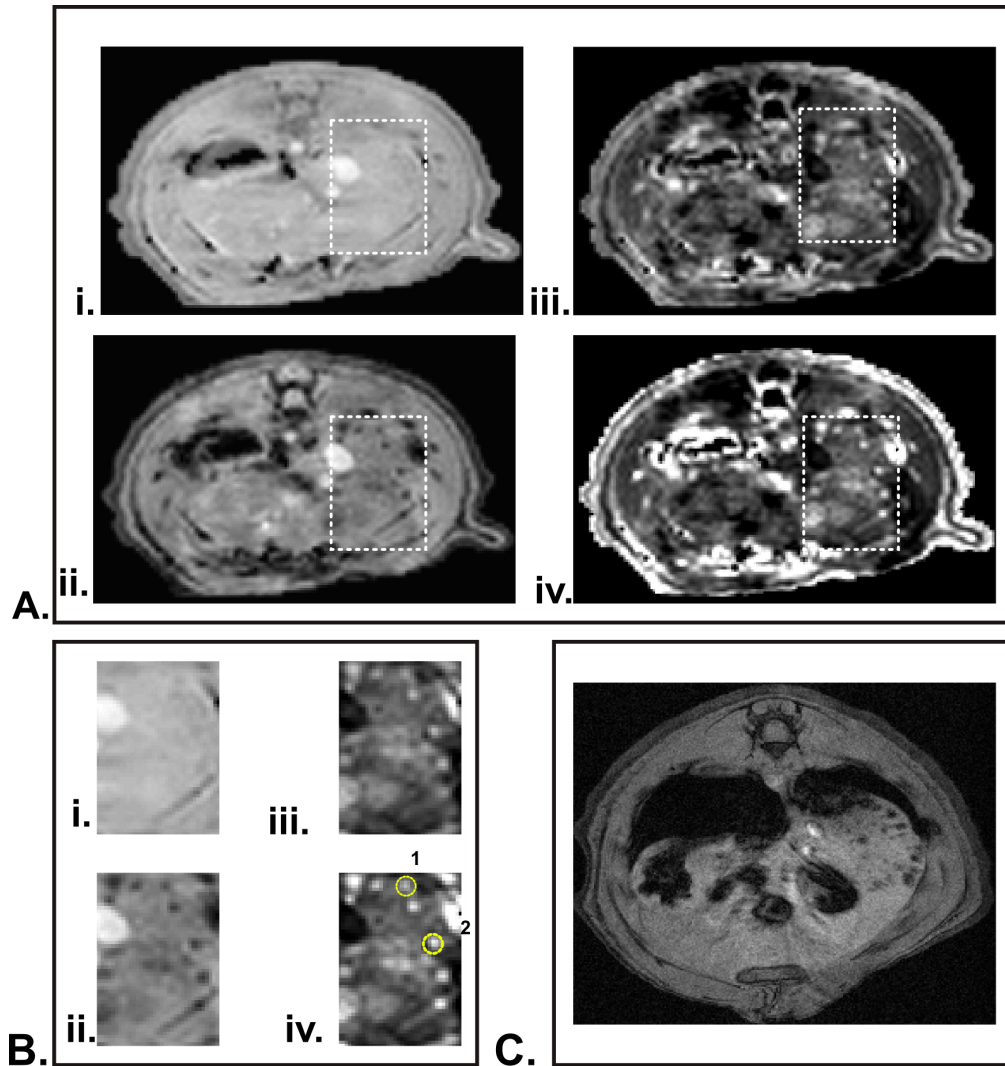


Figure 4.2: MR images from a rat that has undergone transplantation of PIs: A) axial sample images from a 3D variable TE SPGR images from a clinical 3T MR scanner: (i) sub-millisecond first echo image ($TE = 0.8$ ms), (ii) second echo image ($TE = 6.75$ ms), (iii) image difference, (iv) relative subtraction image, B) Details from all four images of subfigure 4.2A, where the labeled islets are more clearly visible (on subfigure 4.2Biv the ROIs that were used for CNR calculations are indicated) C) high resolution (i.e., 0.23 mm) axial SPGR sample image (from a 2D multi-slice dataset) acquired on an experimental 4.7T animal scanner.

4.3.3 Patient scan

Transplanted pancreatic islets could be positively identified on two different slices (see Fig. 4.3 left and right) in patient scans. They could be identified as regions without

any hypointensities present in the sub-millisecond first echo acquired at 0.65 ms (see Fig. 4.3A) and hypointense regions on the second echo (see Fig. 4.3B). On the positive contrast image (i.e., the image difference) distributed hyperintensities (see Fig. 4.3C) were visible in the close vicinity of the islets. On the relative subtraction images islets were also identified in both positions (see Fig. 4.3D). The relative subtraction images offer better background suppression and therefore better contrast-to-noise (see Table 4.2). In one of the slices (see Fig. 4.3C right) an islet was revealed by the positive contrast imaging, which was not visible in the late echo. The fact that islets were identified only in two locations could be attributed to the fact that the patient was scanned six months after transplantation where the majority of the iron was cleared out from islets or islets were already lost [6, 11].

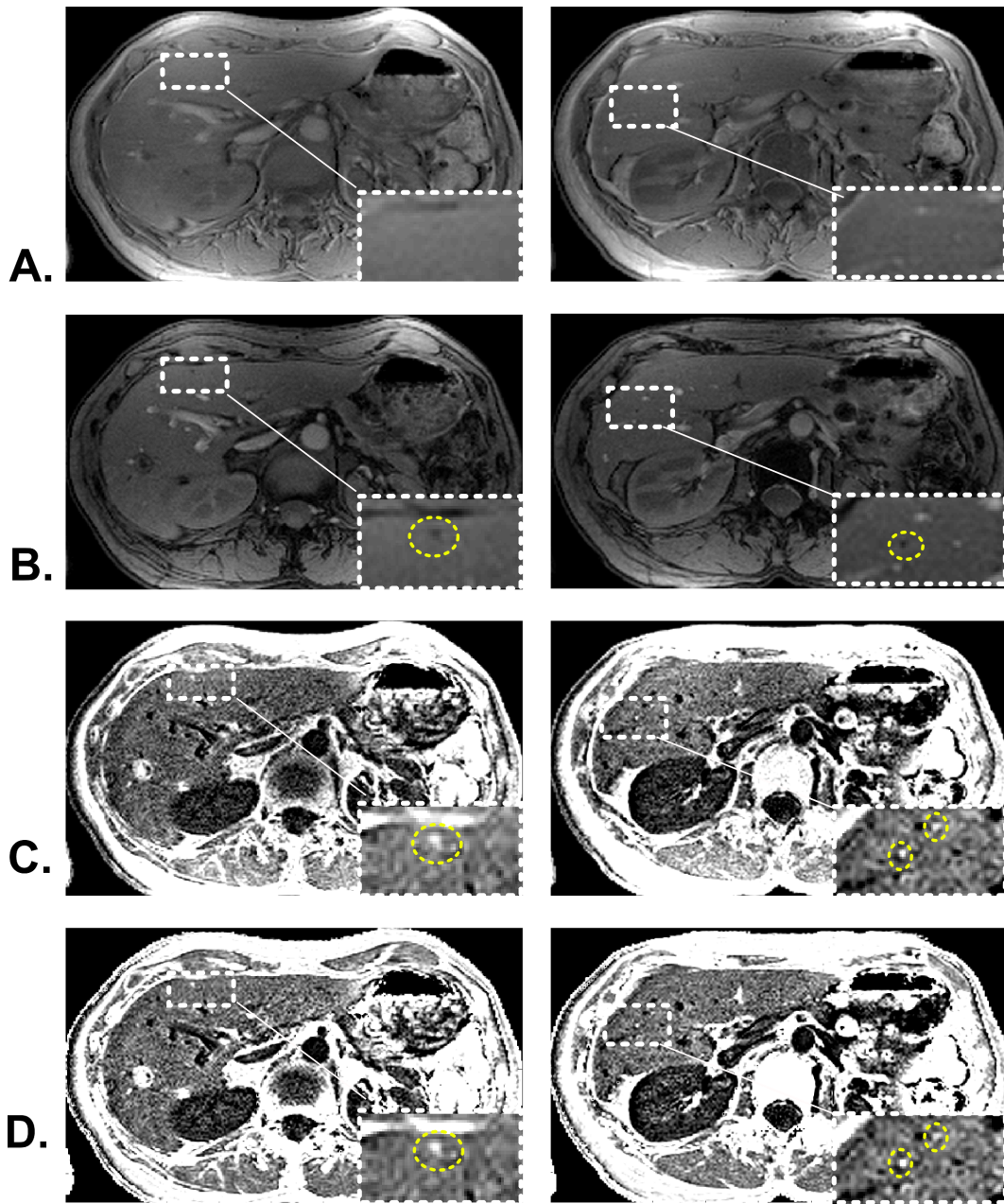


Figure 4.3: MR Images ($1.3 \times 1.3 \times 2.5 \text{ mm}^3$, acquisition time 19 s) acquired at two different slice positions (left & right) 3T with a variable TE 3D SPGR sequence from a patient, who had undergone transplantation of labeled pancreatic islets: A) sub-millisecond first echo acquired at 0.65 ms, B) second echo at 6 ms, C) difference image, D) relative subtraction image. The ROIs of the islets that were used for CNR calculations are indicated on Fig. 4.3B.

4.4 Discussion

In this study, the development of a sequence that provides sub-millisecond echo times similar to UTE techniques allowed positive contrast imaging of species with very short T_2^* . As a basis for the development of the sequence, a 3D SPGR template was used since in addition to high contrast anatomical images it offers larger volume coverage, and is suitable for application in a breath-hold (i.e., we suppose there will be a benefit for patients who have trouble holding their breath, especially in end-expiration mode). The sequence demonstrated high sensitivity as even single islets could be visualized in vitro with positive contrast images. Labeled PIs were also identified positively in the rat, as well as in the patient scans.

In addition, the fact that the sequence is fast and flexible could also offer the possibility of adding special preparation schemes for fat suppression or other utilities. This could be especially useful in the case of obese patients or patients with fibrotic liver.

The technique has shown low sensitivity to shimming issues. During the experiment only the standard product pre-scan 3D shimming procedure was used. As we can see from Fig. 4.1 at the edges of phantom this can be an issue, but nevertheless, we see on Fig. 4.3 that the image quality on the liver does not suffer from any shimming issues

The background level has lower intensity in the positive contrast images, but is more suppressed in the relative subtraction ones. In this case, the patient was scanned 6 months after transplantation and the labeling effect is not so strong any more. As a result, thresholding would be challenging, but in the case of patients scanned in shorter time after the transplantation it would be probably feasible.

Currently, due to a pause in production of Resovist for human use, further research related to SPIO labeled islets on humans must be delayed. There is active research towards new agents that investigate the use of different particles such as magnetoliposomes [26]. Methods using particles with iron concentration comparable to the currently used or more could profit from the proposed method.

The significant finding of this study was also the confirmation of the clearance of the area representing transplanted islets in human liver over time by a different imaging approach. It is another part of mosaic where we try to image transplanted pancreatic islets because it confirms the results obtained from previously used animal models and human studies [11]. In addition, the fact that islets could be detected with a double contrast approach in breath-hold scans even 6 months after transplantation is a promising result for future applications. The two different positive contrast methods exhibited better contrast than the late echo images. The relative subtraction images yielded comparable or in some cases better contrast than the simple subtraction images.

We showed that the use of the proposed 3D vTE SPGR sequence is transferable to the situation in patients with transplanted pancreatic islets and we believe this approach might be extended to any kind of iron labeled cells. Finally, the most important result from the current study is that achieving sub-millisecond echo time with the proposed 3D short echo time sequence, provides during a breath-hold of a patient high CNR, good anatomy information and sensitivity to SPIO labeled cells.

In conclusion, the proposed 3D vTE SPGR sequence is sensitive to iron labeled single islets in vitro and can be used to identify SPIO labeled islets in the liver. The achievement of sub-millisecond echo time while preserving high image contrast allowed successful reconstruction of positive contrast images and relative subtraction images. Islets were identified positively in positive contrast images in an animal in vivo as well as in a patient. To our knowledge these are the first patient results of positive contrast liver MRI for detecting pancreatic islets. So this sequence could improve the segmentation accuracy in unclear cases of islet detection and relative subtraction could offer important information for threshold identification with increased contrast-to-noise.

References

- [1] W. Liu and J. A. Frank, "Detection and quantification of magnetically labeled cells by cellular MRI," *Eur J Radiol*, vol. 70, pp. 258–264, May 2009. PMID: 18995978.
- [2] J. Langley, W. Liu, E. K. Jordan, J. A. Frank, and Q. Zhao, "Quantification of SPIO nanoparticles in vivo using the finite perturber method," *Magn Reson Med*, vol. 65, pp. 1461–1469, May 2011. PMID: 21500271.
- [3] J. W. M. Bulte and D. L. Kraitchman, "Iron oxide MR contrast agents for molecular and cellular imaging," *NMR Biomed*, vol. 17, pp. 484–499, Nov. 2004. PMID: 15526347.
- [4] R. P. Robertson, "Islet transplantation as a treatment for diabetes — a work in progress," *N Engl J Med*, vol. 350, no. 7, pp. 694–705, 2004.
- [5] A. J. Shapiro, J. R. Lakey, E. A. Ryan, G. S. Korbutt, E. Toth, G. L. Warnock, N. M. Kneteman, and R. V. Rajotte, "Islet transplantation in seven patients with type 1 diabetes mellitus using a glucocorticoid-free immunosuppressive regimen," *N Engl J Med*, vol. 343, no. 4, pp. 230–238, 2000.
- [6] D. Jiráček, J. Kríz, V. Herynek, B. Andersson, P. Girman, M. Burian, F. Saudek, and M. Hájek, "MRI of transplanted pancreatic islets," *Magn Reson Med*, vol. 52, pp. 1228–1233, Dec. 2004. PMID: 15562474.
- [7] D. Jirak, J. Kriz, M. Strzelecki, J. Yang, C. Hasilo, D. J. White, and P. J. Foster, "Monitoring the survival of islet transplants by MRI using a novel technique for their automated detection and quantification," *Magn Reson Mater Phy*, vol. 22, pp. 257–265, Aug. 2009. PMID: 19390886.
- [8] Y. Jiao, Z.-H. Peng, T.-H. Xing, J. Qin, and C.-P. Zhong, "Assessment of islet graft survival using a 3.0-tesla magnetic resonance scanner," *Anat Rec (Hoboken)*, vol. 291, pp. 1684–1692, Dec. 2008. PMID: 18951510.
- [9] N. V. Evgenov, Z. Medarova, J. Pratt, P. Pantazopoulos, S. Leyting, S. Bonner-Weir, and A. Moore, "In vivo imaging of immune rejection in transplanted pancreatic islets," *Diabetes*, vol. 55, pp. 2419–2428, Sept. 2006. PMID: 16936189.
- [10] C. Toso, J.-P. Vallee, P. Morel, F. Ris, S. Demuylder-Mischler, M. Lepetit-Coiffe, N. Marangon, F. Saudek, A. M. James Shapiro, D. Bosco, and T. Berney, "Clinical magnetic resonance imaging of pancreatic islet grafts after iron nanoparticle labeling," *Am. J. Transplant.*, vol. 8, pp. 701–706, Mar. 2008. PMID: 18294167.
- [11] F. Saudek, D. Jiráček, P. Girman, V. Herynek, M. Dezortová, J. Kríz, J. Peregrin, Z. Berková, K. Zacharovová, and M. Hájek, "Magnetic resonance imaging of pancreatic islets transplanted into the liver in humans," *Transplantation*, vol. 90, pp. 1602–1606, Dec. 2010. PMID: 21197715.
- [12] K. Zacharovová, Z. Berková, D. Jiráček, V. Herynek, M. Vancová, E. Dovolilová, and F. Saudek, "Processing of superparamagnetic iron contrast agent ferucarbotran in transplanted pancreatic islets," *Contrast Media Mol Imaging*, vol. 7, pp. 485–493, Dec. 2012. PMID: 22991314.
- [13] P. Marzola, B. Longoni, E. Szilagyí, F. Merigo, E. Nicolato, S. Fiorini, G. T. Paoli, D. Benati, F. Mosca, and A. Sbarbati, "In vivo visualization of transplanted pancreatic islets by MRI: comparison between in vivo, histological and electron microscopy findings," *Contrast Media Mol Imaging*, vol. 4, no. 3, p. 135–142, 2009.

- [14] S. Wu, L. Zhang, J. Zhong, and Z. Zhang, "Dual contrast magnetic resonance imaging tracking of iron-labeled cells in vivo," *Cytotherapy*, vol. 12, pp. 859–869, Nov. 2010. PMID: 20184501.
- [15] J.-C. Brisset, M. Sigovan, F. Chauveau, A. Riou, E. Devillard, V. Desestret, M. Touret, S. Nataf, J. Honnorat, E. Canet-Soulas, N. Nighoghossian, Y. Berthezene, and M. Wiart, "Quantification of iron-labeled cells with positive contrast in mouse brains," *Mol Imaging Biol*, vol. 13, pp. 672–678, Aug. 2011. PMID: 20734153.
- [16] C. H. Cunningham, T. Arai, P. C. Yang, M. V. McConnell, J. M. Pauly, and S. M. Conolly, "Positive contrast magnetic resonance imaging of cells labeled with magnetic nanoparticles," *Magn Reson Med*, vol. 53, pp. 999–1005, May 2005. PMID: 15844142.
- [17] F. Eibofner, G. Steidle, R. Kehlbach, R. Bantleon, and F. Schick, "Positive contrast imaging of iron oxide nanoparticles with susceptibility-weighted imaging," *Magn Reson Med*, vol. 64, pp. 1027–1038, Oct. 2010. PMID: 20564596.
- [18] Q. Zhao, J. Langley, S. Lee, and W. Liu, "Positive contrast technique for the detection and quantification of superparamagnetic iron oxide nanoparticles in MRI," *NMR in Biomedicine*, vol. 24, no. 5, p. 464–472, 2011.
- [19] L. A. Crowe, F. Ris, S. Nilles-Vallespin, P. Speier, S. Masson, M. Armanet, P. Morel, C. Toso, D. Bosco, T. Berney, and J.-P. Vallee, "A novel method for quantitative monitoring of transplanted islets of langerhans by positive contrast magnetic resonance imaging," *Am. J. Transplant.*, vol. 11, pp. 1158–1168, June 2011. PMID: 21564535.
- [20] C. J. Bergin, J. M. Pauly, and A. Macovski, "Lung parenchyma: projection reconstruction MR imaging," *Radiology*, vol. 179, pp. 777–781, June 1991. PMID: 2027991.
- [21] M. D. Robson, P. D. Gatehouse, M. Bydder, and G. M. Bydder, "Magnetic resonance: an introduction to ultrashort TE (UTE) imaging," *J Comput Assist Tomogr*, vol. 27, pp. 825–846, Dec. 2003. PMID: 14600447.
- [22] P. Martirosian, C. Schraml, F. Springer, N. F. Schwenzer, C. Würslin, F. Schick, and M. Deimling, "Positive contrast MR imaging of tendons, ligaments, and menisci by subtraction of signals from a double echo steady state sequence (sub-DESS)," *Magn Reson Med*, Feb. 2013. PMID: 23400875.
- [23] X. Deligianni, P. Bär, K. Scheffler, S. Trattng, and O. Bieri, "High-resolution fourier-encoded sub-millisecond echo time musculoskeletal imaging at 3 tesla and 7 tesla," *Magn Reson Med*, Dec. 2012. PMID: 23233430.
- [24] G. McGibney, M. R. Smith, S. T. Nichols, and A. Crawley, "Quantitative evaluation of several partial fourier reconstruction algorithms used in MRI," *Magn Reson Med*, vol. 30, pp. 51–59, July 1993. PMID: 8371675.
- [25] F. Santini, S. Patil, and K. Scheffler, "IceLuva: a scripting framework for MR image reconstruction based on free software," *Concepts Magn Reson B Magn Reson Eng*, vol. 39B, pp. 1–10, Feb. 2011.
- [26] A. L. Ketkar-Atre, T. Yin, T. Struys, W. Malaise, and U. Himmelreich, "Longitudinal follow up of pancreatic islets by MRI using labeling with magnetoliposomes," (Salt Lake City, USA), 2013.

Part II

Fat-Water quantification

Chapter 5

Fast Quantitative Fat-Water Liver Imaging Based on a Multi-Echo Gradient Echo Singular Value Decomposition Matrix Pencil Method

5.1 Introduction

Accurate non-invasive quantification of the liver fat fraction (FF) is important for the diagnosis as well as for the follow-up of patients suffering from various disorders such as non-alcoholic fatty liver disease (NAFLD), alcoholic liver disease or viral hepatitis B and C [1–4]. NAFLD has a high prevalence in the western world and is characterized by excessive triglyceride accumulation in the liver [1]. It ranges from simple steatosis to type-2 diabetes and steatohepatitis and can also lead to end-stage liver disease [1, 5, 6]. The clinical standard for quantification of liver FF is non-targeted biopsy; an invasive procedure that is moreover subjected to sampling variability [7], and is thus not performed unless there is a clear pathological evidence. Alternatively, $^1\text{H-NMR}$ spectroscopy is the current gold standard for non-invasive quantification of the liver FF but requires a complicated setup and does not offer whole organ coverage [8–10]. Consequently, both biopsy and spectroscopy are prone to sampling errors – a drawback that can be overcome by whole organ quantification of the liver FF. As a result, over the years several MRI techniques have been developed for water-fat quantification.

Dixon techniques, originally introduced in 1984 [11], exploit the chemical shift between water and fat to derive the relative amount of water and fat from images where the water and the main peak of fat are either in- or out-of-phase, respectively. Overall, Dixon techniques rely on the restrictions on echo times and the number of sampled echoes, which has led to the development of extended two-point approaches [12–14], allowing more flexible sequence design, or multiple-point techniques [4, 15–21], which account for field inhomogeneities. A different approach that allows more flexible echo times and the acquisition of multiple echo points is the iterative decomposition of water and fat with echo asymmetry and least-squares estimation (IDEAL) based on an iterative least squares method [22, 23], however, it requires a priori knowledge about the fat spectra and it assumes a common T_2^* for the water and fat components [24]. Although the primary objective of all multiple-point water-fat imaging techniques is the quantification of liver fat, the simultaneous correction or quantification of field inhomogeneities and iron induced T_2^* effects were introduced as secondary objectives [16], since it was important to consider the effects from both fat and T_2^* as they may interfere with the estimation of each other [13]. Multi-echo approaches, in particular, have been shown to be more robust to the presence of iron [25]. O’ Regan et al. [26] proposed a multi-echo approach using bi-exponential fitting of the data to calculate both water-fat maps and individual water-fat T_2^* maps (i.e., separate T_2^* for the water and the fat component of the liver) [26]. This approach did not require a priori knowledge, but the echoes were restricted to in- and out-of- phase echo times, the sequence was two-dimensional and iterative curve fitting was used. Both healthy and obese participants were scanned with encouraging results and an extension of this approach to 3D and improved resolution is clinically desirable.

In this chapter, a novel technique for water-fat mapping will be introduced based on a singular value decomposition matrix pencil (SVD-MP) method; a computationally fast algorithm that originates from the spectroscopic analysis presented by Lin et

al. in 1997 [27]. It will be shown that its application in combination with an adapted three-dimensional (3D) multi-echo spoiled gradient echo (SPGR) acquisition using sequentially shifted echo times, accurate liver water-fat fractions can be derived within a single breath hold.

5.2 Methods

All measurements were performed on a 3T clinical whole body MRI system (Verio, Siemens Medical Solutions, Erlangen, Germany) with a 6-channel phased-array body coil.

5.2.1 Singular Value Decomposition Matrix Pencil Method

For the analysis of the signal time course in each voxel, a spectroscopic approach proposed by Lin et al. is used [27]. To this end, it is assumed that the observed signal $s_n = (s_0, s_1, \dots, s_{N-1})$ (sampled at N discrete time points t_n) can be decomposed into a set of M damped exponentials (modulo a global phase drift related to macroscopic field inhomogeneities):

$$s_n = \sum_{j=1}^M |a_j| \exp(i\theta_j) \times \exp[(-\alpha_j + i2\pi f_j) t_n] + w_n =: \sum_{j=1}^M a_j z_j^n + w_n \quad (5.1)$$

where $|a_j|$ and θ_j refers to the amplitude and phase of the individual modes, α_j and f_j reflect the inverse time constants (damping factors) and frequencies of the exponentials and w_n the Gaussian random variables representing the noise components. In Eq. 5.1, $z \equiv \exp(-\alpha_j + i2\pi f_j)$ are the individual signal poles, which are calculated directly by solving the associated Eigenvalue problem with a singular value decomposition after simplifying the data matrix through calculation of the Toeplitz matrix of the free induction decay [27–29]. For simplicity, a single peak analysis of the fat component was adopted (i.e., $M = 2$ in Eq. 5.1), taking into consideration only the main fat resonance peak, which is shifted 3.35 ppm from the water peak (i.e., at -420 Hz at 3T), as commonly applied with Dixon techniques. As a result, Eq. 5.1 reduces to

$$s_n = A_W \times \exp[-t_n/T_{2,w}^*] + A_F \times \exp[-t_n/T_{2,f}^* - i\Delta\omega t_n] \quad (5.2)$$

where t_n is the time after the excitation (i.e., the echo time TE_n), $\Delta\omega$ is the frequency difference between water and fat, $A_W(A_F)$ and $T_{2,w}^*(T_{2,f}^*)$ are the water (fat) signal amplitude and transverse relaxation time respectively.

5.2.2 Sequence Adaptation and Setup

A conventional multi-echo 3D spoiled gradient echo (SPGR) sequence was adapted to allow a signal time course analysis according to the SVD-MP method. To this end,

the echo spacing was shortened using sequentially shifted echo times in an interleaved mode, similar to the approach presented by Liu et al. for optimization of the echo time spacing [30]. Overall, twelve equally spaced echoes were acquired (constant spacing is required from the post-processing SVD-MP algorithm): for every phase encoding step, a first excitation pulse preceded six echoes (i.e., TE_1, TE_3, TE_5-TE_{11}), followed by another excitation and subsequent acquisition of another six echoes (i.e., TE_2, TE_4, TE_6-TE_{12}) but shifted in time (see Fig. 5.1).

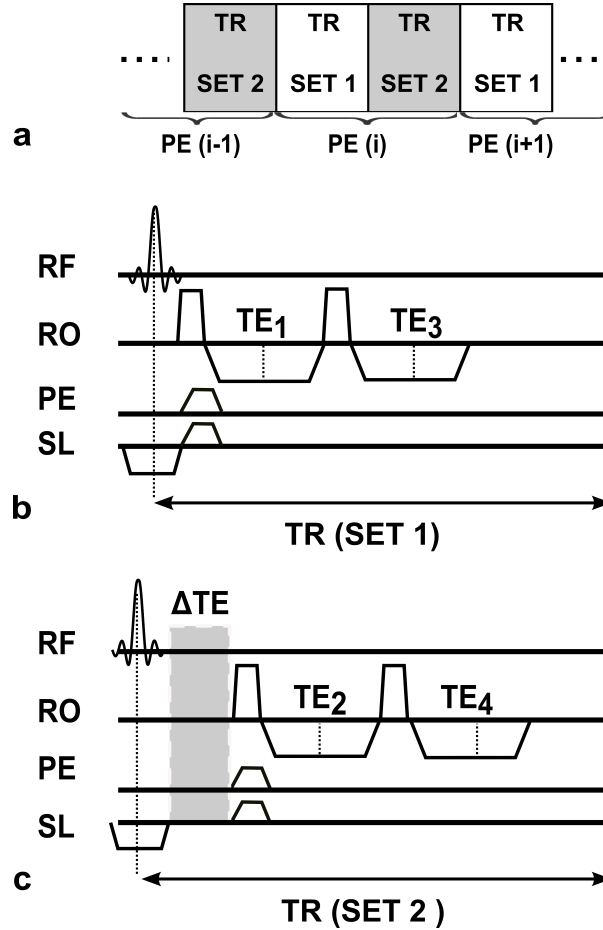


Figure 5.1: Multi-echo SPGR sequence diagram with sequentially shifted echo times. For every phase encoding step, there are two different TR sets (see Fig. 5.1a). The first set of echoes (b) is almost identical to the second set of echoes (c). The difference is that the second set of echoes (c), which follows the second excitation, is shifted in respect to the first one (b) by a delay time equal to the echo spacing (ΔTE).

The SVD-MP adapted multi-echo SPGR sequence was first tested on dairy cream phantoms with a nominal fat percentage of 25 % and 35 %, respectively. The dairy creams were heated as described by Fieremans et al [31], cooled down overnight, and

scanned the next day. Subsequently, four healthy volunteers (mean age 28.5 ± 1 years) were examined and informed written consent was obtained from all the volunteers prior to scanning. All images were acquired in a single breath-hold in end-expiration mode.

Multi-echo SPGR scans were performed in 3D (FOV = 380×285 mm, in-plane resolution = 2.4 mm, 16 slices, slice thickness = 4.4 mm, BW = 1360 Hz / pixel, flip angle = 6°) with a TR of 16 ms, a TE₁ of 1.12 ms, and ΔTE of 0.92 ms. The same protocol was used for both, phantom and in vivo, scans. The total acquisition time was reduced to 22 sec using parallel imaging: GRAPPA of a factor 2, elliptical scanning and partial Fourier acquisition in slice (6/8) and phase (5/8) orientation. Slice oversampling (50 %) was used to compensate for the slab profile and a standard Sinc pulse with duration 0.24 ms and time-bandwidth product 7.8 was employed for selective volume excitation. Advanced shimming was used and the shimming volume was restricted to the liver area for the in vivo scans.

For comparison, standard 3D two-point Dixon (2P-Dixon) scans were performed, with parameters matched as close as possible to the multi-echo SPGR acquisition. (FOV = 380×285 mm, in-plane resolution = 2.4 mm, 16 slices, slice thickness = 4 mm, BW = 470 Hz / pixel, flip angle = 15°) with a TR of 20 ms, a TE₁ of 2.45 ms, and TE₂ of 3.68 ms. The total acquisition time was reduced to 23 sec using parallel imaging as described above for the multi-echo acquisition.

5.2.3 Data Analysis

For the online reconstruction of water and fat maps in the scanner only magnitude data were used [27, 32], but both magnitude and phase data were elaborated with Matlab 7.0 (The Mathworks, Inc., MA, USA, R2008b), based on the initial Matlab script as provided by Lin et al [27]. The phase data served to correct for the erroneous mapping of the subcutaneous fat. The input magnitude images in both cases were filtered with a Gaussian 3x3 kernel. Additionally, the FF maps in Matlab were filtered with a median filter. The signal decomposition was performed pixelwise and subsequently segmented manually for the in vivo liver data along all 16 slices to avoid any visible vasculature and the edges of the liver. The normalized fat fraction (FF) was calculated for each slice and given in percent units according to:

$$FF(\%) = 100 \cdot \frac{A_F}{A_F + A_W} \quad (5.3)$$

An analogous procedure was adopted for the 2P-Dixon method: water and fat images were reconstructed online and the FF was calculated offline based on Eq. 5.3. The regions-of-interest (ROI) were selected as similar as possible to the ones identified for the SVD-MP method and the average fat content for every phantom and volunteer was calculated in the same way (i.e., initially the mean of a ROI on the liver was calculated for every slice and then the mean value of all 16 slices).

5.3 Results

All echoes required to have equal spacing for signal analysis with the MP method. In addition, the first echo was chosen as short as possible while using only symmetric echoes and monopolar gradients, because this setup resulted in lower FFs. Trying to set the echoes as close as possible to in- and out-of-phase echo times did not yield lower fat fractions.

5.3.1 Liver Fat Quantification in Dairy Cream Phantoms

Exemplary water-fat imaging in cream phantoms with the SVD-MP method is demonstrated in Fig. 5.2. A sample signal curve from the middle slice of the volume (i.e., 8th slice see Fig. 5.2a) was analyzed. The phantom with the highest fat percentage (i.e. 35 %) exhibited bigger oscillations (see Fig. 5.2b). At the middle slice of the volume the fat percentage calculated with the SVD-MP method was 25.1 ± 1.0 % and 33.1 ± 1.2 % (see Fig. 5.2c, d) for the two phantoms with a nominal fat percentage of 25 % and 35 %, respectively. Overall, the fat and water maps were smooth and with a small standard deviation (i.e., the mean standard deviation for all slices was approximately 1.7 % for both phantoms). The average fat percentage observed the SVD-MP method was 25.1 % and 33.0 % across all slices (see Table 5.1), while the 2P-Dixon method yielded 39.5 % and 46.3 %, respectively.

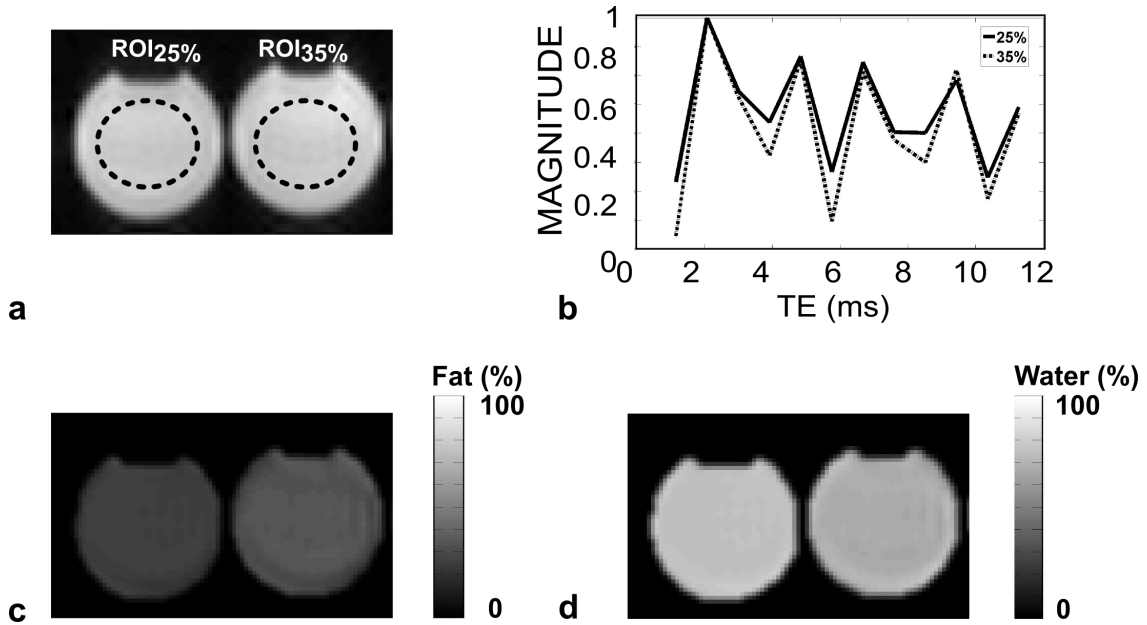


Figure 5.2: Sample phantom images: (a) reference echo image (at 2.08 ms), on which the ROIs for the analysis are indicated, (b) exemplary magnitude signal decay versus time, (c) fat and (d) water fraction maps from two dairy phantoms with nominal milk fat percentage 25 % and 35 % from the middle slice of the scanned volume.

5.3.2 Liver Fat Quantification In Vivo

For the online water and fat image reconstruction on the scanner, only magnitude images were used. As a result, subcutaneous fat was wrongly assigned to water, however, no water-fat shifts were observed inside the liver volume. For the offline reconstruction, both magnitude and phase image data were used, resulting in a correct assignment over the whole image. Quantification was done on the magnitude images only, but identification was done based on the complex data. Empirically, it was found that in liver tissue water components were characterized by f_i values (see Eq. 5.1) less than 0.2 Hz as calculated with the complex fitting. This threshold was used to correct the erroneous mapping of the subcutaneous fat region mentioned above.

The mean liver FF values calculated with the proposed method averaged over all 16 slices are presented on Table 5.1. The maximum liver FF for the four subjects (see Table 5.1) as calculated with the SVD-MP method was 2.9 % and did not exceed 5 - 6 % among all subjects tested, as theoretically expected from healthy volunteers [33]. The mean liver FF ranged from 1.6 % - 2.9 %, which is in agreement with the results presented by O' Regan et al. [26] where for healthy volunteers the multi-echo method yielded 1.3 % - 4.8 % and the spectroscopy 1.1 % - 3.7 %.

	Fat fraction(%)	
	SVD-MP	2P-Dixon
Phantom 1	25.1 ± 1.6	39.5 ± 1.9
Phantom 2	33.0 ± 1.8	46.3 ± 1.9
Subject 1	1.6 ± 1.1	4.2 ± 1.7
Subject 2	1.9 ± 1.1	4.8 ± 1.4
Subject 3	2.6 ± 1.4	4.9 ± 1.5
Subject 4	2.9 ± 1.7	8.0 ± 2.4

Table 5.1: Mean fat fractions over all 16 measured slices for the dairy cream phantoms and liver fat fractions for the four healthy volunteers.

As an example, calculated fat maps along all 16 slices are presented in Fig. 5.3 for subject 4 and the mean liver fat percentage along all measured slices and for all volunteers is presented in Fig. 5.4. Overall, the liver FF appeared homogeneous in the liver area (see Fig. 5.3) and relatively constant across slices (see Fig. 5.4).

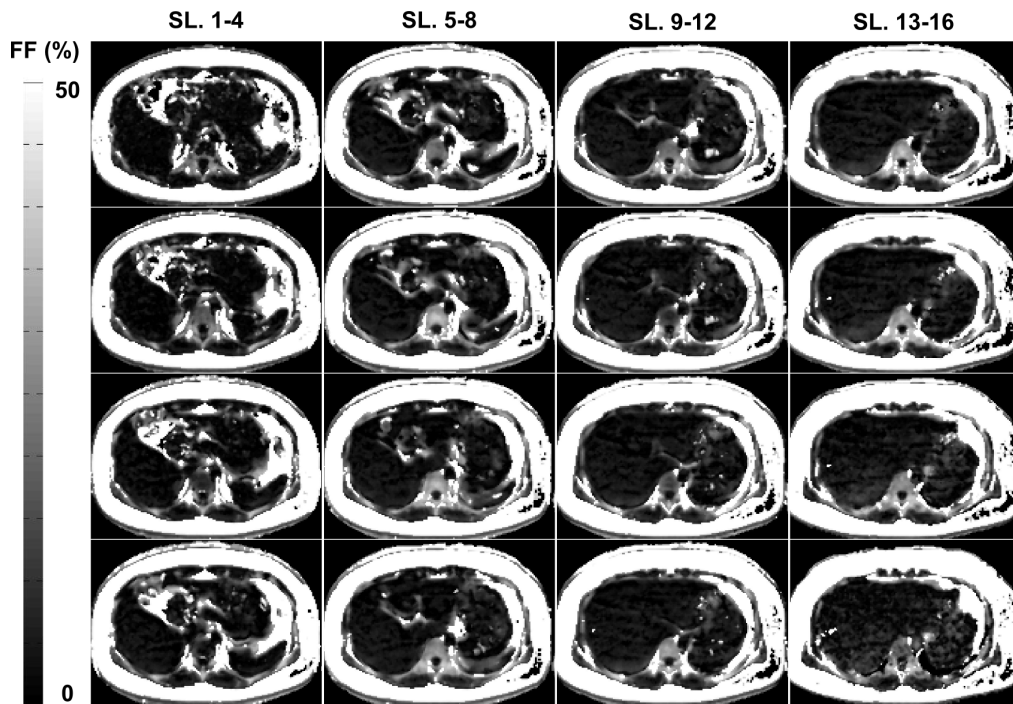


Figure 5.3: Exemplary Liver FF maps from subject 4 measured along all 16 slices.

In the middle slice (i.e., the 8th slice) of the volume the standard deviation of the liver FF across the liver region was 1.1 %, 0.7 %, 1.3 %, 1.9 % for subjects 1 - 4 respectively and the average variation over all slices for all subjects ranged from 1.1% to 1.7%. The liver FF appeared to be slightly lower than the average in the upper slices towards the direction of the head and higher than the average in the lower ones.

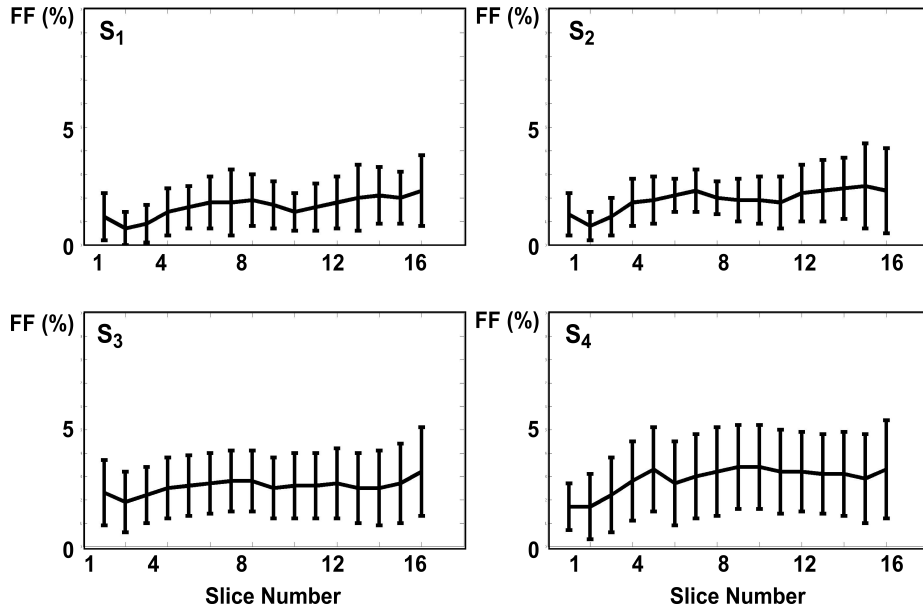


Figure 5.4: Mean liver FFs from all subjects for each measured slice. The average standard deviation of the mean liver FF across all the slices was 1.1 %, 1.1 %, 1.4 % and 1.7 % for subject 1, 2, 3 and 4 respectively.

The liver FFs from the 2P-Dixon method were on average increased by 3.2 % (see Table 5.1) as compared to the fat percentage observed with the SVD-MP. The mean liver FF with the 2P-Dixon method was 5.5 %, which was a bit higher than the 4.5 - 5 % reported as threshold in literature [34–36]. As an example, a comparison between the liver FF maps from SVD-MP and 2P-Dixon are presented in Fig. 5.5 for the subjects with the lowest and highest fat percentage (i.e., subject 1 and 4), respectively.

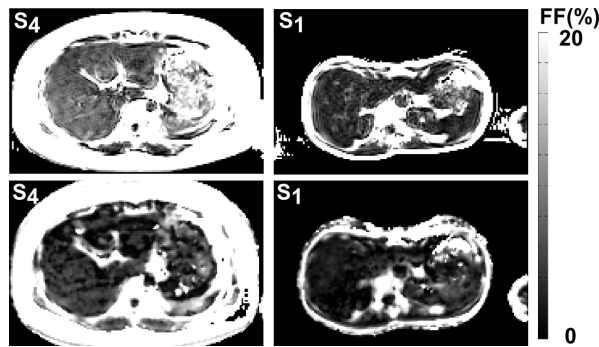


Figure 5.5: Liver FF maps (top: 2P-Dixon, bottom: SVD-MP) of the middle slice are presented for the subjects with the highest (subject 4, left) and the lowest (subject 1, right) fat percentage, respectively.

5.4 Discussion

Fat quantification was shown to be accurate within 2 % of the theoretically expected fat percentage in dairy cream phantoms. Fat quantification at 3T with the SVD-MP method on healthy volunteers was demonstrated to be within the limits of fat fractions expected from the results presented by O' Regan et al [26] and below 5 % as we would expect from $^1\text{H-NMR}$ spectroscopy [8, 37, 38]. Overall, the fat content of normally appearing liver tissue observed by the SVD-MP method was about 3 % lower than the one derived with the 2P-Dixon method (see Fig. 5.5, Table 5.1). It has been reported that liver FF appears higher than normal, since due to its longer T_1 , water gets partially suppressed [39]. In the SVD-MP, to exclude a possible T_1 related bias in the fat estimation with fast SPGR-based imaging, fat scans were repeated with different flip angles (ranging from 6° up to 10°), but no dependence on the flip angle was observed for the mean FF.

In contrast to common Dixon methods that typically suffer from water-fat swap [17, 26, 40, 41], the SVD-MP method does not rely on phase unwrapping algorithms. Subcutaneous fatty tissue, however, was wrongly attributed as water, since data analysis was based on magnitude data. Generally, it is a common occurrence that areas with very high fat content are wrongly attributed as belonging to water, and these areas can be identified within the SVD-MP method by using complex rather than magnitude data.

Complex data, however, were used only for recognition of these specific regions but not for calculation of water and fat fractions, since the algorithm turned out to be more robust when using the magnitude data as input.

Since twelve echoes could be acquired within a single breath hold, various approaches to resolve the iron content can in principle be used, such as information theory [42], but in this work, our main interest was focused on the detection of fat content only. In addition, the signal from the twelve echoes could be used for multi-spectral fat analysis, which has been shown to be beneficial for dealing with inaccuracies (i.e. incorrect fat fraction or T_2^* estimation) occurring due to the assumption that fat has a single resonance frequency [10, 18]. The inclusion in the post-processing of more than one peak for the fat component could also allow individual estimation of T_2^* for fat and water [18].

In conclusion, the SVD-MP analysis method in combination with the adapted multi-echo SPGR acquisition provides an efficient new method to accurately assess whole liver water-fat fractions at 3T. In combination with the SVD-MP method, sequential shifting of echo times offers optimal echo spacing and allows for the acquisition of twelve echoes and 16 slices of 4.4 mm slice thickness of the liver in a single breath-hold.

References

- [1] M. Krawczyk, L. Bonfrate, and P. Portincasa, “Nonalcoholic fatty liver disease,” *Best Practice & Research Clinical Gastroenterology*, vol. 24, pp. 695–708, Oct. 2010.
- [2] R. S. O’Shea, S. Dasarathy, A. J. McCullough, P. G. C. o. t. A. A. f. t. S. o. L. Diseases, and t. P. P. C. o. t. A. C. o. Gastroenterology, “Alcoholic liver disease,” *Hepatology*, vol. 51, no. 1, p. 307–328, 2010.
- [3] D. Peng, Y. Han, H. Ding, and L. Wei, “Hepatic steatosis in chronic hepatitis b patients is associated with metabolic factors more than viral factors,” *Journal of Gastroenterology and Hepatology*, vol. 23, no. 7pt1, p. 1082–1088, 2008.
- [4] C.-H. Guo, P.-C. Chen, and W.-S. Ko, “Status of essential trace minerals and oxidative stress in viral hepatitis c patients with nonalcoholic fatty liver disease,” *Int J Med Sci*, vol. 10, pp. 730–737, Apr. 2013. PMID: 23630437 PMCID: PMC3638296.
- [5] J. D. Browning, L. S. Szczepaniak, R. Dobbins, P. Nuremberg, J. D. Horton, J. C. Cohen, S. M. Grundy, and H. H. Hobbs, “Prevalence of hepatic steatosis in an urban population in the united states: impact of ethnicity,” *Hepatology*, vol. 40, pp. 1387–1395, Dec. 2004. PMID: 15565570.
- [6] J. Ludwig, T. R. Viggiano, D. B. McGill, and B. J. Oh, “Nonalcoholic steatohepatitis: Mayo clinic experiences with a hitherto unnamed disease,” *Mayo Clin Proc*, vol. 55, pp. 434–438, July 1980. PMID: 7382552.
- [7] V. Ratziu, F. Charlotte, A. Heurtier, S. Gombert, P. Giral, E. Bruckert, A. Grimaldi, F. Capron, and T. Poynard, “Sampling variability of liver biopsy in nonalcoholic fatty liver disease,” *Gastroenterology*, vol. 128, pp. 1898–1906, June 2005. PMID: 15940625.
- [8] S. McPherson, J. R. Jonsson, G. J. Cowin, P. O’Rourke, A. D. Clouston, A. Volp, L. Horsfall, D. Jothimani, J. Fawcett, G. J. Galloway, M. Benson, and E. E. Powell, “Magnetic resonance imaging and spectroscopy accurately estimate the severity of steatosis provided the stage of fibrosis is considered,” *Journal of Hepatology*, vol. 51, pp. 389–397, Aug. 2009.
- [9] N. Pineda, P. Sharma, Q. Xu, X. Hu, M. Vos, and D. R. Martin, “Measurement of hepatic lipid: high-speed t2-corrected multiecho acquisition at 1H MR spectroscopy—a rapid and accurate technique,” *Radiology*, vol. 252, pp. 568–576, Aug. 2009. PMID: 19546430.
- [10] G. Hamilton, T. Yokoo, M. Bydder, I. Cruite, M. E. Schroeder, C. B. Sirlin, and M. S. Middleton, “In vivo characterization of the liver fat ¹H MR spectrum,” *NMR Biomed*, vol. 24, pp. 784–790, Aug. 2011. PMID: 21834002.
- [11] W. T. Dixon, “Simple proton spectroscopic imaging,” *Radiology*, vol. 153, pp. 189–194, Oct. 1984.
- [12] T. E. Skinner and G. H. Glover, “An extended two-point dixon algorithm for calculating separate water, fat, and b0 images,” *Magn Reson Med*, vol. 37, pp. 628–630, Apr. 1997. PMID: 9094088.
- [13] H. Eggers, B. Brendel, A. Duijndam, and G. Herigault, “Dual-echo dixon imaging with flexible choice of echo times,” *Magn Reson Med*, vol. 65, pp. 96–107, Jan. 2011. PMID: 20860006.
- [14] Q.-S. Xiang, “Two-point water-fat imaging with partially-opposed-phase (POP) acquisition: an asymmetric dixon method,” *Magn Reson Med*, vol. 56, pp. 572–584, Sept. 2006. PMID: 16894578.

- [15] G. H. Glover and E. Schneider, “Three-point dixon technique for true water/fat decomposition with b_0 inhomogeneity correction,” *Magn Reson Med*, vol. 18, pp. 371–383, Apr. 1991. PMID: 2046518.
- [16] H. Yu, C. A. McKenzie, A. Shimakawa, A. T. Vu, A. C. S. Brau, P. J. Beatty, A. R. Pineda, J. H. Brittain, and S. B. Reeder, “Multiecho reconstruction for simultaneous water-fat decomposition and t_2^* estimation,” *J Magn Reson Imaging*, vol. 26, pp. 1153–1161, Oct. 2007. PMID: 17896369.
- [17] J. Ma, “Dixon techniques for water and fat imaging,” *J Magn Reson Imaging*, vol. 28, pp. 543–558, Sept. 2008. PMID: 18777528.
- [18] H. Yu, A. Shimakawa, C. A. McKenzie, E. Brodsky, J. H. Brittain, and S. B. Reeder, “Multiecho water-fat separation and simultaneous r_2^* estimation with multifrequency fat spectrum modeling,” *Magn Reson Med*, vol. 60, pp. 1122–1134, Nov. 2008. PMID: 18956464.
- [19] Q.-S. Xiang, “Water-fat and t_2^* mapping with 3-point acquisitions,” in *Proceedings 16th Scientific Meeting, International Society for Magnetic Resonance in Medicine*, (Toronto), p. 1383, 2008.
- [20] B. Guiu, R. Loffroy, J.-M. Petit, S. Aho, D. Ben Salem, D. Masson, P. Hillon, J.-P. Cercueil, and D. Krause, “Mapping of liver fat with triple-echo gradient echo imaging: validation against 3.0-t proton MR spectroscopy,” *Eur Radiol*, vol. 19, pp. 1786–1793, July 2009. PMID: 19247667.
- [21] B. Guiu, J.-M. Petit, R. Loffroy, S. Aho, D. Ben Salem, D. Masson, I. Robin, B. Vergès, P. Hillon, J.-P. Cercueil, and D. Krause, “Liver methylene fraction by dual- and triple-echo gradient-echo imaging at 3.0T: correlation with proton MR spectroscopy and estimation of robustness after SPIO administration,” *J Magn Reson Imaging*, vol. 33, pp. 119–127, Jan. 2011. PMID: 21182129.
- [22] S. B. Reeder, A. R. Pineda, Z. Wen, A. Shimakawa, H. Yu, J. H. Brittain, G. E. Gold, C. H. Beaulieu, and N. J. Pelc, “Iterative decomposition of water and fat with echo asymmetry and least-squares estimation (IDEAL): application with fast spin-echo imaging,” *Magn Reson Med*, vol. 54, pp. 636–644, Sept. 2005. PMID: 16092103.
- [23] S. B. Reeder, C. A. McKenzie, A. R. Pineda, H. Yu, A. Shimakawa, A. C. Brau, B. A. Hargreaves, G. E. Gold, and J. H. Brittain, “Water-fat separation with IDEAL gradient-echo imaging,” *J. Magn. Reson. Imaging*, vol. 25, no. 3, p. 644–652, 2007.
- [24] H. H. Hu, H.-W. Kim, K. S. Nayak, and M. I. Goran, “Comparison of fat-water MRI and single-voxel MRS in the assessment of hepatic and pancreatic fat fractions in humans,” *Obesity (Silver Spring, Md.)*, vol. 18, pp. 841–847, Apr. 2010. PMID: 19834463.
- [25] A. C. A. Westphalen, A. Qayyum, B. M. Yeh, R. B. Merriman, J. A. Lee, A. Lamba, Y. Lu, and F. V. Coakley, “Liver fat: effect of hepatic iron deposition on evaluation with opposed-phase MR imaging,” *Radiology*, vol. 242, pp. 450–455, Feb. 2007. PMID: 17255416.
- [26] D. P. O’Regan, M. F. Callaghan, M. Wylezinska-Arridge, J. Fitzpatrick, R. P. Naoumova, J. V. Hajnal, and S. A. Schmitz, “Liver fat content and t_2^* : simultaneous measurement by using breath-hold multiecho MR imaging at 3.0 t—feasibility,” *Radiology*, vol. 247, pp. 550–557, May 2008. PMID: 18349314.
- [27] Y.-Y. Lin, P. Hodgkinson, M. Ernst, and A. Pines, “A novel Detection–Estimation scheme for noisy NMR signals: Applications to delayed acquisition data,” *J Magn Reson*, vol. 128, pp. 30–41, Sept. 1997.

- [28] Y. Hua and Y. Zhang, "On SVD for estimating generalized eigenvalues of singular matrix pencil in noise," *IEEE Transactions on Signal Processing*, vol. 39, pp. 892–900, Apr.
- [29] R. Roy, A. Paulraj, and T. Kailath, "ESPRIT—A subspace rotation approach to estimation of parameters of cisoids in noise," *IEEE Transactions on Acoustics, Speech and Signal Processing*, vol. 34, pp. 1340–1342, Oct.
- [30] W. Liu, H. Dahnke, J. Rahmer, E. K. Jordan, and J. A. Frank, "Ultrashort t_2^* relaxometry for quantitation of highly concentrated superparamagnetic iron oxide (SPIO) nanoparticle labeled cells," *Magn Reson Med*, vol. 61, pp. 761–766, Apr. 2009. PMID: 19191285 PMID: PMC3384488.
- [31] E. Fieremans, A. Pires, and J. H. Jensen, "A simple isotropic phantom for diffusional kurtosis imaging," *Magn Reson Med*, vol. 68, pp. 537–542, Aug. 2012. PMID: 22161496.
- [32] F. Santini, S. Patil, and K. Scheffler, "IceLuva: a scripting framework for MR image reconstruction based on free software," *Concepts Magn Reson B Magn Reson Eng*, vol. 39B, no. 1, p. 1–10, 2011.
- [33] L. S. Szczepaniak, P. Nurenberg, D. Leonard, J. D. Browning, J. S. Reingold, S. Grundy, H. H. Hobbs, and R. L. Dobbins, "Magnetic resonance spectroscopy to measure hepatic triglyceride content: prevalence of hepatic steatosis in the general population," *Am. J. Physiol. Endocrinol. Metab.*, vol. 288, pp. E462–E468, Feb. 2005.
- [34] M. A. Fischer, D. Nanz, C. S. Reiner, M. Montani, S. Breitenstein, S. Leschka, H. Alkadhi, P. Stolzmann, B. Marincek, and H. Scheffel, "Diagnostic performance and accuracy of 3-d spoiled gradient-dual-echo MRI with water- and fat-signal separation in liver-fat quantification: comparison to liver biopsy," *Invest Radiol*, vol. 45, pp. 465–470, Aug. 2010. PMID: 20479652.
- [35] N. Mennesson, J. Dumortier, V. Hervieu, L. Milot, O. Guillaud, J.-Y. Scoazec, and F. Pilleul, "Liver steatosis quantification using magnetic resonance imaging: a prospective comparative study with liver biopsy," *J Comput Assist Tomogr*, vol. 33, pp. 672–677, Oct. 2009. PMID: 19820490.
- [36] R. J. H. Borra, S. Salo, K. Dean, R. Lautamäki, P. Nuutila, M. Komu, and R. Parkkola, "Nonalcoholic fatty liver disease: Rapid evaluation of liver fat content with in-phase and out-of-phase MR imaging1," *Radiology*, vol. 250, pp. 130–136, Jan. 2009. PMID: 19017926.
- [37] M. Hajek, M. Dezortova, D. Wagnerova, A. Skoch, L. Voska, I. Hejlova, and P. Trunecka, "MR spectroscopy as a tool for in vivo determination of steatosis in liver transplant recipients," *Magn Reson Mater Phy*, vol. 24, pp. 297–304, Oct. 2011. PMID: 21744232.
- [38] C. Thomsen, U. Becker, K. Winkler, P. Christoffersen, M. Jensen, and O. Henriksen, "Quantification of liver fat using magnetic resonance spectroscopy," *Magn Reson Imaging*, vol. 12, no. 3, pp. 487–495, 1994.
- [39] M. Bydder, T. Yokoo, G. Hamilton, M. S. Middleton, A. D. Chavez, J. B. Schwimmer, J. E. Lavine, and C. B. Sirlin, "Relaxation effects in the quantification of fat using gradient echo imaging," *Magn Reson Imaging*, vol. 26, pp. 347–359, Apr. 2008. PMID: 18093781.
- [40] H. K. Hussain, T. L. Chenevert, F. J. Londy, V. Gulani, S. D. Swanson, B. J. McKenna, H. D. Appelman, S. Adusumilli, J. K. Greenson, and H. S. Conjeevaram, "Hepatic fat fraction: MR imaging for quantitative measurement and display—early experience," *Radiology*, vol. 237, pp. 1048–1055, Dec. 2005. PMID: 16237138.

- [41] S. H. Kim, J. M. Lee, J. K. Han, J. Y. Lee, K. H. Lee, C. J. Han, J. Y. Jo, N.-J. Yi, K.-S. Suh, K.-S. Shin, S. Y. Jo, and B. I. Choi, "Hepatic macrosteatosis: predicting appropriateness of liver donation by using MR imaging—correlation with histopathologic findings," *Radiology*, vol. 240, pp. 116–129, July 2006. PMID: 16684918.
- [42] Y.-Y. Lin, P. Hodgkinson, M. Ernst, and A. Pines, "A novel Detection–Estimation scheme for noisy NMR signals: Applications to delayed acquisition data," *Journal of Magnetic Resonance*, vol. 128, pp. 30–41, Sept. 1997.

Part III
Conclusion

Chapter 6

Summary and conclusion

The main goal of this thesis was to develop a method of capturing fast decaying signals that has potentials for clinical use and secondly to use the signal decay for quantifying tissue properties. Therefore, this thesis was developed in two different directions. Both methods were developed out of modified spoiled gradient echo sequences.

The first goal was to develop a fast and robust short echo time sequence for visualization of short T_2 components. The initial focus of the sequence was musculoskeletal imaging. For this reason its application on high and ultra-high field was investigated, as well as its application in combination with fat suppression methods.

The second part of the thesis was focused on the analysis of the signal decay, as measured with a multi-echo sequence, in order to produce an accurate method for quantifying liver fat. The goal was to develop a fast method that produces accurate results, well related to spectroscopy methods and offers improved acquisition parameters in comparison to existing methods.

6.1 Variable Echo Time Imaging

UTE sequences and high to ultra-high field are beneficial for scanning short T_2 species due to their very short relaxation times [1,2]. However, the translation of UTE sequences to the clinics remains challenging. Variable echo time sequences can benefit from the robustness of Cartesian sampling, while offering the possibility to reduce sufficiently the echo time for acquisition of short T_2 signal.

A novel implementation of a variable echo time sequence was presented in chapter 2. vTE sequences can provide sub-millisecond echo times, which are sufficient for the visualization of fibrous MSK tissues since they are characterized by short but not ultrashort T_2 relaxation times. In this chapter, the feasibility of imaging musculoskeletal fibrous tissue components, such as menisci, ligaments, and tendons, with a conventional spoiled gradient echo technique was explored in vivo at 3 Tesla and 7 Tesla. It was demonstrated that after optimization, the presented Fourier-encoded spoiled gradient echo sequence provides a highly robust and flexible imaging technique for high-resolution positive contrast imaging of fibrous tissue that can readily be used in the clinical routine.

For imaging of fibrous musculoskeletal components, short or ultra-short echo time methods are often combined with a conventional presaturation of the fat signal using dedicated magnetization preparation schemes (FATSAT pulses). Alternatively, due to the increased chemical shift, spectral excitation of water might become especially favorable at ultra-high fields. Thus, in chapter 3 different short binomial excitation schemes for spectrally selective imaging of fibrous tissue components with short transverse relaxation time (T_2) were analyzed. Water selective 1-1 binomial excitation was compared to common FATSAT and nonselective imaging using a sub-millisecond spoiled gradient echo technique for in vivo imaging of fibrous tissue at 3 Tesla and 7 Tesla. It was demonstrated that for imaging of short-lived T_2 components, short 1-1 binomial excitation schemes proved to perform favorably over conventional FATSAT techniques, offering marginal signal loss especially at ultra-high fields with overall improved scanning efficiency.

Short T_2 relaxation times can be an inherent tissue characteristic such as in the case of tendons or an induced one such as in the case of labeled cells. In chapter 4 the vTE method was adapted for in vivo imaging of iron-labeled islets. The vTE scheme was used to develop and evaluate a double contrast method for the detection of pancreatic islets labeled with superparamagnetic iron oxide (SPIO) nanoparticles. A three-dimensional (3D) spoiled gradient echo sequence was adapted to yield a sub-millisecond first echo time using variable echo times and highly asymmetric Cartesian readout. The presented method allows 3D data acquisition within a single breath-hold and provides positive contrast of transplanted SPIO labeled pancreatic islets enhanced relative to standard negative contrast and thus improved identification.

6.2 Water-Fat Imaging

The increased research interest to identify and quantify water and fat signals was motivated by the raising prevalence of obesity and diabetes in the western world [3]. Increased presence of fat can indicate various pathologies. In this thesis I focused on measuring fat in the liver. Detection of increased presence of fat in the liver is more commonly detected in the last 20 years and is of increased importance since it usually appears in asymptomatic patients [4]. Fat in the liver is an important marker for various disorders, such as non-alcoholic and alcoholic fatty liver diseases, or viral hepatitis. The gold standard for follow-up of fat diseases is biopsy, which is an invasive procedure. In contrast to biopsy, MR spectroscopy-based fat quantification is non-invasive but can be flawed by spatial heterogeneities. Imaging offers a more global image but it can also be affected by T_2^* and other effects. Therefore there is a need for optimization and standardization of fat measurement with MRI.

In chapter 5, a novel three-dimensional (3D) multi-echo approach was introduced for liver water-fat imaging. A conventional spoiled gradient echo (SPGR) sequence was modified to provide twelve multi-echo images for water-fat analysis based on a singular value decomposition matrix pencil (SVD-MP) method; a powerful algorithm to analyze the signal from multiple damped exponentials. Water-fat measurements were performed in phantoms and in vivo in the liver in a single breath hold and compared to common two-point Dixon imaging. The results were very accurate on phantoms and on the expected range in volunteers. The proposed SVD-MP analysis in combination with the adapted SPGR acquisition provides an efficient new method to accurately assess liver water-fat fractions within a single breath hold.

6.3 Outlook

Future work will be focused both on translating the results to a clinical level, as well as on further methodological developments.

Regarding the vTE method, further developments at ultra-high field will be focused on sodium imaging for MSK applications at ultra-high field. Initial work [5,6] has shown

that sodium imaging with the vTE method is feasible and promising, but the method can still be further optimized.

Regarding the second part of the thesis and the water-fat quantification future work will be performed on the translation of the method to a clinical level. Many promising water-fat quantification techniques have been developed, but one of the most important challenges is to move these methods to a clinical level and establish diagnostic standards. Therefore, the next important step is to establish a relation with the gold standard, that is spectroscopy, in order to make it possible to use the sequence for diagnostic purposes. This step is already planned in collaboration with our colleagues in the Institute of Experimental Medicine in Prague.

From a development point of view, the method will be developed further in order to include a multi-peak spectrum. Another possible direction for development would be T_2^* quantification, since the method in principle can provide also dual T_2^* estimation (i.e., independent T_2^* estimation for the water and fat components). However, an accurate estimation of water and fat relaxation values would require an assumption of a multi-peak fat spectrum for the fat, or at least a second fat peak [7].

In conclusion, this thesis aimed to offer a set of new tools to be applied to MSK and liver imaging, with the potential to be directly useful both in clinics and in basic research. My hope is that my work will in the future be able to exploit the characteristics of the gradient echo-based MR acquisitions in order to expand the knowledge and the possibility for MSK imaging from one hand and increase the diagnostic value of MRI for diagnosis of fatty liver on the other.

References

- [1] P. D. Gatehouse and G. M. Bydder, “Magnetic resonance imaging of short t2 components in tissue,” *Clin Radiology*, vol. 58, pp. 1–19, Jan. 2003. PMID: 12565203.
- [2] M. D. Robson, P. D. Gatehouse, M. Bydder, and G. M. Bydder, “Magnetic resonance: an introduction to ultrashort TE (UTE) imaging,” *Journal of Computer Assisted Tomography*, vol. 27, pp. 825–846, Dec. 2003. PMID: 14600447.
- [3] H. H. Hu, P. Bornert, D. Hernando, P. Kellman, J. Ma, S. Reeder, and C. Sirlin, “ISMRM workshop on fat-water separation: Insights, applications and progress in MRI,” *Magn Reson Med*, vol. 68, pp. 378–388, Aug. 2012. PMID: 22693111 PMCID: PMC3575097.
- [4] R. J. H. Borra, S. Salo, K. Dean, R. Lautamäki, P. Nuutila, M. Komu, and R. Parkkola, “Nonalcoholic fatty liver disease: Rapid evaluation of liver fat content with in-phase and out-of-phase MR imaging1,” *Radiology*, vol. 250, pp. 130–136, Jan. 2009. PMID: 19017926.
- [5] S. Zbyn, V. Juras, H. Michaely, X. Deligianni, O. Bieri, S. Schoenberg, S. Trattnig, and S. Haneder, “In vivo functional sodium MR imaging of the human kidneys at 7 tesla,” in *Proceedings 21th Scientific Meeting, International Society for Magnetic Resonance in Medicine*, (SLC, USA), p. 4140, 2013.
- [6] S. Zbyn, S. Apprich, V. Juras, P. Szomolanyi, S. Walzer, X. Deligianni, H. Traxler, O. Bieri, and S. Trattnig, “Ex vivo mapping of sodium t1 and t2* relaxation times in human lumbar intervertebral discs at 7 tesla,” in *Proceedings 21th Scientific Meeting, International Society for Magnetic Resonance in Medicine*, (SLC, USA), p. 2473, 2013.
- [7] H. Yu, A. Shimakawa, C. A. McKenzie, E. Brodsky, J. H. Brittain, and S. B. Reeder, “Multiecho water-fat separation and simultaneous r2* estimation with multifrequency fat spectrum modeling,” *Magn Reson Med*, vol. 60, pp. 1122–1134, Nov. 2008. PMID: 18956464.

Acknowledgment

I would like to acknowledge and deeply thank all the people, that helped me conclude these four years successfully.

I would like to thank my advisor Prof. Klaus Scheffler for offering me the opportunity to perform this thesis and supporting me through it.

My supervisor Prof. Oliver Bieri for his guidance, advice and help and for offering me the opportunity to get in contact with other scientific groups.

My co-examiner Prof. Sebastian Kozerke for participating in my thesis examination.

The present and former colleagues from radiological physics group of Basel especially Claudia and Jinxia for going through these years together.

My collaborators in IKEM, Prague and Excellence Center, Vienna for allowing me to see the actual use and application of the projects, for giving value to our work and for working with me. Especially Daniel Jirak for his help and enthusiasm.

I would like to acknowledge my colleagues and friends in Utrecht and Bordeaux University for guiding me in my first steps in MRI and making me to endorse this research domain.

And I would like to thank all the people behind the scenes my friends local, international and my old friends in Greece, and above all my family for its never-ending support that made it possible to come here.

Last but definitely not least, I would like to thank Francesco for his guidance in my first steps in sequence programming, his help and motivation, as well as his family for their support. But mostly for being always there not only as a colleague, but as a friend, companion, buddy and as my new family in the course of these four years.

Xeni Deligianni

Curriculum Vitae

Personal Data

Name: Xeni Deligianni

Date of birth: 24 Oct. 1983

Place of birth: Thessaloniki, Greece

Citizenship: Greek

Education

Oct. 2009 - Oct. 2013: PhD in BioPhysics

University of Basel, Switzerland

Supervisor: Prof. Dr. Klaus Scheffler

Sept. 2007 - Sept. 2009: MSc in Biomedical Image Sciences

Utrecht University, The Netherlands

Oct. 2008 - June 2009: Master Thesis

University Bordeaux 2, CNRS, Bordeaux, France

Sept. 2001 - July 2007: Diploma in Electrical Engineer and Computers Engineering

Aristotle University of Thessaloniki, Thessaloniki, Greece